

The Behaviour of Water Drops on Insulating Surfaces Stressed by Electric Field

Vom Fachbereich 18
Elektrotechnik und Informationstechnik
der Technischen Universität Darmstadt

zur Erlangung
der Würde eines Doktor-Ingenieurs (Dr.-Ing.)
genehmigte

DISSERTATION

von
Dipl.-Ing. Simona Feier-lova, geb. Iova
geb. in Salonta, Rumänien

Referent: Prof. Dr.-Ing. V. Hinrichsen
Korreferent: Prof. Dr.-Ing. M. Kurrat

Tag der Einreichung: 09.09.2009
Tag der mündlichen Prüfung: 23.11.2009

D17
Darmstadt, 2009

Acknowledgement

This dissertation is an outcome of the work done as a scientific assistant at the High Voltage Laboratories of the Technische Universität Darmstadt which I have joined in the end of 2004. A thesis is seldom the work of a single person rather than the result of a research activity involving a bunch of people. I am pleased now to acknowledge those who have, in various ways, contributed to this work. I owe a great debt of gratitude to all of them.

First and foremost I express my sincere thanks to Prof. Dr.-Ing. Volker Hinrichsen, for giving me the opportunity to work in his group and also for his kind and constructive guidance during the entire period of my PhD, but above of all for his constant confidence.

I am also grateful to Prof. Dr.-Ing. Michael Kurrat from Technische Universität Braunschweig for kindly accepting to be my co-referee and for the co-operation during the dissertation time.

Without financial support, research becomes difficult. Accordingly, thanks to the German Research Foundation (DFG) for supporting in parts this work. Special thanks goes to Mr. Dr. rer. nat. Erion Gjonaj from Computational Electromagnetics Institute for his valuable input to the simulation part of this work. Thanks to Mr. Dr. Hans-Jörg from Wacker Chemie AG, Burghausen for supplying us silicone rubber material for the specimens.

I would like to express my gratitude to the workshop of our Institute for helping me with their technical support in the laboratory. All students who contributed with their work to obtain the results used in this thesis a warm thank you. My thanks should go also to all the colleagues at the High voltage Laboratories, their friendship and professional collaboration meant a great deal to me. In particular, I would like to thank my office mate Alexander Rocks for his friendly support and for helping me to solve many administrative tasks along the five years spent in the same office. Many thanks to Masoumeh Koochack Zadeh, Michael Tenzer, Patrick Halbach and Sébastien Blatt for their help especially in the end phase of this thesis and for the interesting discussions during the coffee breaks.

Many thanks also to Mr. Günther Kloss for his help during the experimental measurements and time spent in the electromagnetic shielded hall.

I feel myself blessed to have a family who were there always with their love and affection. I would like to thank my parents Maria and Moise Iova for their support of all my life choices and their love. Many special thanks go to my lovely husband Dr. Ovidiu Feier-Iova for being the person he is and being a constant source of strength for everything I do.

Contents

Acknowledgement	i
List of symbols.....	vi
List of figures	x
List of tables	xi
Abstract	xiii
Kurzfassung	xvi
1 Introduction	1
2 Wetting Properties of Polymeric Surfaces.....	4
2.1 Wetting Theory.....	4
2.1.1 Static and Dynamic Contact Angle	5
2.2 Hydrophobicity on an Insulating Surface	6
2.2.1 Hydrophobicity Theory	6
2.2.2 Quantification of Hydrophobicity	8
2.2.3 Loss and Recovery of Hydrophobicity on Polymeric Surfaces	10
3 Electrical Ageing Processes on Polymeric Material	13
3.1 Early Ageing Processes on Polymeric Surfaces	13
3.2 Late Ageing Processes on Polymeric Surfaces.....	14
4 Partial Discharges	17
4.1 Definition of Terms.....	17
4.2 External Partial Discharges	18
4.3 Measurement Method of Partial Discharges	19
5 Water Drops under Electric Field Stress.....	22
5.1 Behaviour of Water Drops under Electric Field Stress	22
5.2 Discharge Mechanism at the Water Drops	25
5.2.1 Ionization Coefficient.....	26
5.2.2 Attachment Coefficient	28
5.2.3 Second Emmision Coeficient	28
5.2.4 Streamer mechanism	30
5.3 Determination of the Ionization Coefficient.....	33
5.4 Inception Voltage Influencing Parameters	37
5.4.1 Ambient Conditions	37
5.4.2 Atmospheric Negative Ion Density	39
5.5 Goals of this work	45

6	Experimental Techniques	47
6.1	Test Setup	47
6.1.1	Model Insulator	47
6.1.2	Optical Mirror System and High Speed Camera	50
6.1.3	Calculation of the Applied Electric Field	54
6.1.4	Water Drops	62
6.2	High Voltage Equipment and PD Measurement System	63
6.3	Photomultiplier System	64
6.4	Climate Chamber	67
6.5	UV Camera	67
7	Results.....	69
7.1	Observations on Water Drops.....	69
7.1.1	Water Drop Deformation under Alternating Electric Field Stress	69
7.1.2	Water Drop Deformation under Direct Electric Field Stress.....	72
7.2	Partial Discharge Activity at Water Drops	75
7.2.1	Comparison between PD System and PMT System Recordings	75
7.2.2	Localization of the PD under Alternating and Direct Field Stress	77
7.2.3	Inception Voltage at Different Volumes of the Water Drop	79
7.2.4	Inception Voltage at Different Ambient Humidities.....	80
7.2.5	Inception Voltage at Different Ambient Temperatures	86
8	Modelling and Simulation of the Water Drops on a Insulating Surface Stressed by Electric Field.....	87
8.1	Modelling	87
8.1.1	Modelling of a typical 40 μ l Water Drop	89
8.1.2	Modelling of a typical 60 μ l Water Drop	90
8.1.3	Modelling of a typical 80 μ l water drop.....	90
8.2	Simulations.....	91
8.2.1	Simulation Considerations.....	91
8.2.2	Global Validation Criterion of the Simulation.....	95
8.2.3	Local Validation Criterion of the Simulation	99
8.2.4	Electric Field Enhancement at Undeformed Water Drops	101
8.2.5	Electric Field Enhancement at Modelled Water Drops.....	103
8.2.6	Comparison between the Different Water Drops	110
9	Discussion, Conclusions and Outlook.....	115
9.1	Water Drops under the Electric Field Stress.....	115
9.2	Ageing Model Update.....	117
9.3	Conclusions.....	119

9.4 Outlook.....	123
Standards.....	124
Literature.....	125
Curriculum Vitae.....	133
Publications.....	134

List of symbols

α	-	Ionization coefficient
α_e	-	Effective ionization coefficient
α_1, α_2	°	Angle
δ	-	Relative density correction factor
δ	C/m ³	Charge density
ε	F/m	Permittivity of the material
ε_r	-	Relative permittivity
ε_0	F/m	Permittivity of vacuum
γ	N/m	Surface tension
γ_{SL}	N/m	Interfacial tension of fluid-solid interface
γ_L	N/m	Surface tension of the fluid surface
γ_s	N/m	Surface tension of the solid surface
γ_s	m ³ /s	Secondary emission coefficient
η_{10}	m ³ /s	Combination coefficient (n_+, N_0)
η_{12}	m ³ /s	Combination coefficient (n_-, N_+)
η_{20}	m ³ /s	Combination coefficient (n_-, N_0)
η_{21}	m ³ /s	Combination coefficient (n_+, N_-)
φ	%	Relative humidity
κ	S/m	Electric conductivity
μ_0	H/m	Permeability of vacuum
θ	°	Contact angle
θ_a	°	Advancing contact angle
θ_r	°	Receding contact angle
θ_s	°	Static contact angle
ρ	g/m ³	Density
σ	N/m ²	Tensile stress
Δf	Hz	Band frequency
ΔW	eV	Kinetic energy
Γ	-	Gamma function
Σ	-	Combination coefficient (n_-, n_+)
Y	-	Combination coefficient (N_-, N_+)
A	m ²	Area
a	m	Distance
A, A_1, B	m/N	Constants used for ionization coefficient calculation
\vec{B}	T	Magnetic flux density
C, C_1	N/(m · V)	Constant used for ionization coefficient calculation
C_1	F	Capacitance of the gap
C_3	F	Capacitance of the electrode configuration
C_a	F	Specimen capacitance
C_i	-	Topological matrix
C_k	F	Coupling capacitance
\vec{D}	C/m ²	Electric flux density

E	V/m	Electric field
e	C	Elementary charge
E_0	V/m	Applied electric field
\bar{E}	V/m	Electric field strength
f	Hz	Frequency
F	-	Sphere gap
$F(f)$	-	Spectral amplitude density
G	-	Grid
$\{G, \tilde{G}\}$	-	Staggered grid system
\bar{H}	A/m	Magnetic field strength
H	g/m^3	Water content
H	g/m^3	Absolute humidity
H_0	g/m^3	Standard absolute humidity
I	-	Unity matrix
i	A	Current
i_{em}	A	Electron emission current
k	-	Streamer constant
k	$\text{W} \cdot \text{s/K}$	Boltzmann constant
M	A/m	Magnetization
M	-	Material matrix
n	m^{-3}	Number of ions
n	m^{-3}	Number of small ions
N	m^{-3}	Number of large ions
n_0	m^{-3}	Number of neutral molecules
N_0	m^{-3}	Number of neutral particles
N_{cr}	-	Critical number of electrons
p	Pa	Pressure
P	C/m^2	Polarization density
P	m	Distance
P	-	Partial differential operator
P_a	Pa	External pressure
p_i	Pa	Internal pressure
p_k	Pa	Differential pressure
q	C	Charge
Q	C	Charge
q'	m^3/s	Rate of small ions creation
R	Ω	Resistance
r_1, r_2	m	Radii of curvature
R_2	Ω	Charge carriers resistance
R_{da}	$\text{J}/(\text{g} \cdot \text{K})$	Dry air constant
RH	%	Relative humidity
R_v	$\text{J}/(\text{g} \cdot \text{K})$	Water vapour constant
S	N/m	Spreading coefficient
s	m	Avalanche crossing space

List of symbols

s	m	Distance
t	s	Time
T	K	Temperature
t	-	Singularity exponent
U	V	Voltage
U_0	V	rms normalized voltage at standard atmospheric conditions
u_z	V	Breakdown voltage
V	m^3	Volume
W_{AD}	N/m	Work of adhesion
W_C	N/m	Work of cohesion
W_i	eV	Ionization energy
x	m	Distance
Z_m	Ω	Measuring impedance
η	-	Attachment coefficient of the electrons
λ	m	Mean free path

List of indexes

-	Negative
~	Dual
+	Positive
a	Air
abs	Absolute
d	Breakdown
ha	humid air
i	Inception
i, j, k	Parameters corresponding to each axis
ion	Ionization
m,e	mean electron
m,i	mean ion
max	Maximum
n	Normal
s	Saturation
tan	Tangential
u, v, w	grid coordinates
v	Real
w	Water

List of abbreviations

AC	Alternating current
CCD	Charge coupled device
CMOS	Complementary Metal Oxide Semiconductor
CP	Converge point
DC	Direct current
exp	Exponential
FIFO	First in, first out
FIT	Finite integration technique
FRP	Fibreglass
HC	Hydrophobicity class
HTV	High temperature vulcanized
HV	High voltage
IEC	International Elelctrotechnical Commission
IEEE	Institute of Electrical and Electronics Engineers
IRO	Intensified relay optic
LMW	Low molecular weight
PD	Partial discharge
PMT	Photomultiplier tube
PRPD	Conventional partial discharge system
RTV	Room temperature vulcanized
SIR	Silicone rubber
Sync	Synchronization
TP	Triple point
TTL	Through the lens
UV	Ultra violet
WC	Wettability class

List of chemical abbreviations

O_2^-	Oxygen ion
$C_{14}H_{18}ClN_3S$	Methylene blue
CH_2	Methylen
CH_3	Methyl
CH_n	Alkyl rest where $n=1, 2, 3$
EPDM	Ethylene propylene diene monomer
H_2O	Water
HNO_3	Nitric acid
N_2	Nitrogen
NaOH	Sodium hydroxide
NO_x	Nitrogen oxides, $x=1, 2$
O_2	Oxygen
PDMS	Polydimethylsiloxane

List of figures

Figure 1.1: Types of composite insulators [Lapp2009].....	2
Figure 1.2: Scientific approach.....	3
Figure 2.1: Fluid drop on a solid surface.....	4
Figure 2.2: Dynamic contact angles [IEC/TS 62073]	6
Figure 2.3: Typical examples of surfaces with wettability class (WC) from 1 to 6 [IEC/TS 62073].....	11
Figure 3.1 : Ageing model of polymeric surfaces under electrical and environmental stress.....	15
Figure 4.1: Partial discharge categories [Kön1993]	17
Figure 4.2: External partial discharge equivalent circuit [Kön1993]	18
Figure 4.3: Classification of PD meters for measurement of apparent charge q [Kön1993]	20
Figure 4.4: Basic PD test circuit.....	21
Figure 5.1: The equilibrium requirements of a point on the deformed drop surface.....	23
Figure 5.2: Electric field distortion due to the space charge of an electron avalanche [Küc2005]	30
Figure 5.3: Development of a ionization channel (Streamer mechanism).....	31
Figure 5.4: Avalanche in inhomogeneous field with a negative tip [Küc2005]	32
Figure 5.5: Polarity effect in strong inhomogeneous field with positive and negative tip [Küc2005]	33
Figure 5.6: Ionization coefficient in air according to different authors	37
Figure 6.2: Model insulator used for experiment (a) and electric field lines distribution in air (b).....	48
Figure 6.3: Mould cast of the model insulator	49
Figure 6.5: Model insulator; front, top and side view.....	51
Figure 6.6: Optical system used with the high speed camera.....	52
Figure 6.7: Three views of the water drop in the coordinate system.....	53
Figure 6.9: Schematical diagram of the charge reflection method	56
Figure 6.10: Reflexion law at the boundary of two dielectrics	57
Figure 6.11: Tangential component of the electric field on the insulating surface.....	57
Figure 6.12: Normal component of the electric field on the insulating surface.....	58
Figure 6.13: Absolute values of the electric field on the insulating surface.....	58
Figure 6.14: Discretization units	59
Figure 6.15: Comparison of the calculated and simulated tangential component of the electric field in air.....	59
Figure 6.16: Comparison of the calculated and simulated absolute component of the electric field in air.....	60
Figure 6.17: Electric field distribution in region between the electrodes	61
Figure 6.20: High-voltage circuit.....	63
Figure 6.21: Photomultiplier module.....	65
Figure 6.23: PMT measurement system	66
Figure 6.24: Hermetically closed boxes used for PMT the module	66
Figure 7.2: Partial discharge measurement using PRPD and PMT systems	76
Figure 7.3: Water drop inception field strength as a function of water drop volume and comparison with the literature.....	80
Figure 7.6: Inception electric field strength as a function of absolute humidity	83
Figure 7.8: Inception electric field strength as a function of ambient temperature	86
Figure 8.1: Water drop model using contour curves	88
Figure 8.3: Camera recording and models of three critical deformations for a 60 μ l water drop.....	90
Figure 8.4: Camera recording and models of three common deformations for a 80 μ l water drop.....	91
Figure 8.5: Tetrahedral surface mesh settings for the complete sample	92

Figure 8.6: Tetrahedral surface mesh settings at the water drop.....	93
Figure 8.8: Electric field distribution in the vicinity of the water drop at $U = 1$ kV.....	93
Figure 8.9: Position of the paths for the electric field strength analysis	94
Figure 8.10: Distribution of the tangential electric field strength along the twelve curves in the xz plane	94
Figure 8.12: Singularity exponent as a function of contact angle.....	97
Figure 8.13: Difference of the electric field distribution with drop and without drop, with the area identification	97
Figure 8.14: Comparison between simulated and calculated field enhancement at the water drop	99
Figure 8.15: Electric field enhancement along the given path for a water drop with contact angle of 120° , using three different relative mesh steps.....	100
Figure 8.16: Electric field enhancement for undeformed water drop, zoom of the marked area in Figure 8.15	101
Figure 8.18: Maximum tangential electric field intensification at CP for 40 μ l drop model	104
Figure 8.20: Maximum tangential electric field intensification at CP for 60 μ l drop model	107
Figure 8.21: Maximum absolute electric field intensification at CP for 60 μ l drop model	107
Figure 8.23: Maximum absolute electric field intensification at CP for 80 μ l drop model	110
Figure 8.24: Maximum tangential electric field intensification at different water drop models.....	111
Figure 8.25: Maximum absolute electric field intensification at different water drop models.....	111
Figure 8.26: The absolute local electric field intensifications at different water drop models.....	112
Figure 8.27: Maximum electric field intensification at different water drops.....	113

List of tables

Table 2.1: Processes affecting surface hydrophobicity of a polymeric material.....	7
Table 2.2: Criteria for the determination of wettability class (WC) [IEC/TS 62073].....	9
Table 3.1: Material deterioration as a PD intensity and duration dependence.....	16
Table 5.1: Constant c of equation (5.7) by different authors	25
Table 5.2: Ionization coefficient expressions according to different authors.....	35
Table 5.3: Values of combination coefficients [All1987].....	42
Table 5.4: Neutral particle density N_0 [All1987].....	43
Table 6.1: Properties of material (Wacker Powersil 600) used for the model insulator	49
Table 7.1: The varied parameters during recordings	69
Table 7.4: Water drop movement under direct electric field stress Parameters: $V=80$ μ l; $\gamma=55$ μ S; direct voltage.....	73
Table 7.7: UV-camera recordings for a 40 μ l water drop under direct field stress	78
Table 7.8: Correlation factors between the calculated and measured values of the electric field strength	84
Table 8.1: Three dimensional view of the deformed water drop (80.c).....	88
Table 8.2: 40 μ l water drop models.....	104
Table 8.3: 60 μ l water drop models.....	106
Table 8.4: 80 μ l water drop models.....	109

Abstract

The insulating materials of high voltage equipment are stressed in service over years by several environmental factors. One ageing factor is the humidity, which in combination with the electrical stress causes changes of the conditions on the insulating surface. Polymeric insulators are widely used because of their high contamination resistance and high tensile strength-to-weight ratio, while constituting an unattractive target for vandals. Especially with silicone rubber housings, polymeric insulators exhibit a high surface hydrophobicity. Water drops will be formed on the polymer surface when the insulator is exposed to rain and moisture, and hence the conductive contamination dissolved with water is discontinuous. Hydrophobicity is transferred to pollution layers and after loss of hydrophobicity under severe environmental stress, such as extreme continuous exposure to moisture, it will be recovered in a relatively short time. The aim of this work is to analyze the early ageing conditions of an electrically stressed silicone rubber surface. The influence of water drops under electric field stress on the partial discharge inception phenomena shall provide the focal point of the investigation.

Around the water drops the electric field is intensified. The water drop will be deformed and elongated along the direction of the electric field lines. The deformations will cause local electric field intensifications; the critical point will be the triple point between the water drop, air and the insulating material. This will be a starting point for partial discharges, finally leading to material deterioration.

The water drop movement on the insulating surface is observed and recorded using a high speed camera and a mirror system. The mirror system simultaneously records three different plane views of the water drop. In this way, a three dimensional recording is possible, while providing three dimensional information about the water drop movement. The recordings revealed that the water drops forms sharp edges at the triple point and elongate in the direction of the electric field lines.

The partial discharge activity is analyzed using a standard partial discharge measurement system. As the discharges taking place at one water drop are marginal, the partial discharge system is not sensitive enough to detect the ignition of the discharge. Therefore, a photomultiplier module was used to detect the inception of the discharge activity on the surface. The first light emission of the partial discharges is amplified and converted into an electrical signal. It was revealed that the photomulti-

plier module detects the first partial discharge at a voltage value which is up to 13 % smaller than the value measured using the standard partial discharge system.

Using a UV camera it was observed that discharges take place on the surface starting from the TP of the drop towards electrodes, exactly where the sharp edges are present.

During experiments the following parameters varied: water drop volume, water drop conductivity and ambient conditions. The effects of different parameters on the partial discharge inception conditions are analyzed. The inception electric field strength decreases by increasing the water drop volume. Small water drops exhibit a higher contact angle than larger water drops. The contact angle increase by decreasing the water drop volume.

The ambient conditions also play an important role in determining the inception electric field strength at water drops and it is a parameter which changes very often in normal duty, especially for outdoor insulation. At high humidity and in the presence of the electric field, the oxygen molecules hydrate with the water molecules from moist air, forming large negative ions. As the production of large ions increases exponentially by increasing the humidity, the probability of an avalanche starting is higher at higher humidity than at lower ambient humidity. Hence, the inception electric field strength decreases by increasing the absolute humidity. Two different decay rates were measured. The humidity correction factors presented in this work can be used to predict exactly the inception electric field at the water drops on an insulating surface at a certain absolute humidity value. The practical importance is that the ambient conditions, i.e. absolute humidity, influence PD activities reversely compared with the general breakdown electric field strength. The ambient conditions should always be measured when PD measurements are carried out. Long-term observations and measurements on PD activity will only be of any relevance if the results are obtained under the same humidity conditions or if they are corrected with respect to the humidity level.

The water drop deformations recorded with the high speed camera were modelled using a drawing tool, where the shape and volume of the drop are reproduced very accurately. The electrostatic simulations are carried out using the models and the inception voltage values from the experiments. The simulation results show electric field intensification in the region of the TP. In order to verify the simulation results, an analytical calculation was carried out for an undeformed water drop having a contact angle of 120° . For the deformed water drop the theoretical calculation of the electric

field distribution at the water drop is no longer possible. Therefore, the theoretical consideration revealed that criteria to verify the simulation results must be found. Two criteria are developed, one global and one local. If the simulation results fulfil both criteria, the values can be considered to evaluate the electric field intensifications in the region of water drop. The first criterion, named “integral criterion” is a global validation criterion, e.g. is valid for the whole path along the sample. The interesting point is near the water drop, where the electric field is intensified using a local validation criterion. As the TP is a singularity point, e.g. values of the electric field strength tend towards infinity, the values in the TP cannot be considered in the evaluation of the electric field intensification. The analysis of the electric field curves along the surface at different mesh settings revealed that up to a distance of 0,1 mm from the TP, the curves corresponding to the fine meshes converge and this point is named convergence point (CP). The CP is the point where the electric field intensifications are considered. The electric field intensifications analyzed at the CP show high electric field intensification in the presence of the water drop on the surface.

The variation of the electric field strength with the contact angle and with the contour of the drop is shown by measurements and demonstrated by simulations. For deformed drops, the electric field intensifications are higher and can reach values eight times higher than the applied electric field. The tangential component of the electric field is the affected component by the local field intensifications. Taking into account the magnitude of the local electric field intensification, the deformation of the water drops on the insulating surface must be considered by electrical resistance of the polymeric insulating surfaces.

The absolute value of the electric field is to be considered in order to compare the experimental measurements with the simulation results. For the deformed water drops the absolute values of the electric field are comparable with the inception electric field strength in air.

The ageing model of a polymeric material was upgraded in the region of the early ageing phase. The water drop deformations, their implication on the local electric field intensification and the influence of the ambient conditions on the inception electric field are included in the ageing model for polymeric materials.

Kurzfassung

Isolierstoffe der Hochspannungstechnik unterliegen im Dauerbetrieb einer Vielzahl von Beanspruchungen, die zu ihrer Alterung beitragen. Luftfeuchte bei gleichzeitiger elektrischer Belastung können in einem veränderten Hydrophobieverhalten der Isolierstoffoberfläche resultieren. Polymerisolatoren werden heutzutage wegen ihres positiven Fremdschichtverhaltens und ihrer hohen mechanischen Festigkeit in nahezu allen Spannungsebenen und unter allen Umgebungseinflüssen eingesetzt. Besonders mit Silikongehäuse besitzen die Isolatoren ein hervorragendes Hydrophobieverhalten, was bei Tropfenbildung auf der Isolatoroberfläche durch Regen oder erhöhte Luftfeuchtigkeit verhindert, dass sich Kriechstromwege bilden, die zu Fremdschichtüberschlägen führen können. Selbst bei kurzzeitiger Verschlechterung der Hydrophobie durch extreme äußere Einflüsse sind Polymere in der Lage, sich innerhalb kurzer Zeit selbst zu erholen. Ziel dieser Arbeit ist die Analyse des Alterungsverhaltens im Frühstadium, wenn Silikonoberflächen im elektrischen Feld belastet werden, wobei besonders Teilentladungsphänomene, hervorgerufen durch Tropfenbildung im elektrischen Feld, im Mittelpunkt der Untersuchung stehen.

In Folge der auftretenden Kräfte im elektrischen Feld werden die Tropfen deformiert und in Richtung der Feldlinien gestreckt. Aus den Verformungen resultieren weitere, noch größere Feldstärkeerhöhungen, wobei der kritischste Punkt der sog. Tripelpunkt (TP) ist, an dem Wassertropfen, Luft und Isolierstoffoberfläche aufeinander treffen. Genau an dieser Stelle beginnen die Teilentladungen, die zu verstärkter Materialalterung führen können.

Die Verformung der Wassertropfen auf der Polymeroberfläche im elektrischen Feld wird durch eine Hochgeschwindigkeitskamera in Verbindung mit einem Winkelspiegelsystem visualisiert, so dass gleichzeitig aus drei unterschiedlichen Blickwinkeln die verschiedenen Tropfenoberflächen beobachtet werden können. So wird durch eine dreidimensionale Aufzeichnung auch eine dreidimensionale Auswertung der Tropfenverformung ermöglicht. Bei nahezu allen deformierten Tropfen wurden scharfe Kanten am Tripelpunkt beobachtet.

Die Teilentladungen werden durch ein herkömmliches Aufzeichnungs- und Auswertesystem erfasst. Allerdings sind die Entladungen an den Tropfen zum Teil so gering, dass ihr Einsatz nicht durch das Auswertesystem erfasst wird. Zu diesem Zweck wird ein Photovervielfacher eingesetzt, der die erste Lichtemission einer Teilentladung verstärkt und in ein elektrisches Signal umwandelt. Ein Vergleich der

Messmethoden mit dem Standardmesssystem und dem Photovervielfacher hat gezeigt, dass mit Hilfe des Photovervielfachers ein TE-Einsatz bei 13 % geringerer Spannung als mit dem Standardmesssystem detektiert wird.

Durch den Einsatz einer UV-Kamera konnte gezeigt werden, dass die Teilentladungen unmittelbar vom TP an den Kanten des Tropfens ausgehen.

Für die hier durchgeführten Untersuchungen wurden die Parameter Tropfenvolumen, Leitfähigkeit des Wassers sowie die Umgebungsbedingungen wie Temperatur und Luftfeuchtigkeit variiert.

Gerade die Änderung der Umgebungsbedingungen bei Freiluftisolation ist ein wichtiger Parameter in Bezug auf das Einsetzen von Teilentladungen. Bei hoher Luftfeuchtigkeit im elektrischen Feld werden die vorhandenen Wassermoleküle ionisiert, und es bilden sich u. a. große negative geladene Sauerstoffionen. Die Anzahl der vorhandenen Ionen steigt exponentiell mit der Luftfeuchte, was die verstärkte Entladungstätigkeit bei erhöhter Luftfeuchtigkeit erklärt. Mit anderen Worten sinkt die TE-Einsatzspannung bei steigender Luftfeuchtigkeit, wobei zwei unterschiedliche Abhängigkeiten festgestellt wurden. Die in dieser Arbeit vorgestellten Luftfeuchtekorrekturfaktoren erlauben eine exakte Bestimmung der TE-Einsatzspannung am Wassertropfen auf der Isolierstoffoberfläche abhängig von der vorhandenen Luftfeuchtigkeit. Von besonderer praktischer Bedeutung ist die Feststellung, dass die Änderung der Umgebungsbedingungen den Einsatz von Teilentladungen und die Durchschlagfestigkeit von Luft genau entgegengesetzt beeinflusst – während die Durchschlagfestigkeit von Luft mit höherer absoluter Luftfeuchte steigt, sinkt die TE-Einsatzspannung. Daher müssen die unterschiedlichen Umgebungsbedingungen unbedingt bei der Betrachtung von TE mit berücksichtigt werden. Langzeituntersuchungen und Messungen der TE-Aktivität sind somit nur sinnvoll auswertbar, wenn die Ergebnisse entsprechend den Umgebungsbedingungen korrigiert worden sind.

Die Modellierung der mit der Hochgeschwindigkeitskamera aufgezeichneten Wassertropfenverformung erfolgte mit Hilfe eines Zeichenprogramms, welches Tropfenform und -volumen sehr genau berücksichtigt. Die elektrostatischen Simulationen wurden auf Basis der Ergebnisse der experimentell ermittelten TE-Einsatzspannungen durchgeführt, wobei in den Simulationen ebenfalls stark erhöhte Feldstärken im Bereich des TPs festgestellt werden konnten. Zur weiteren Verifikation der experimentellen und simulatorischen Ergebnisse wurden auf Grundlage eines unverformten Tropfens bei einem Kontaktwinkel von 120° analytische Berechnungen

durchgeführt. Wegen des nicht mehr zu bewältigenden Rechenaufwandes wird auf eine analytische Betrachtung der Verhältnisse an einem verformten Tropfen verzichtet. Somit müssen Kriterien gefunden werden, um die Qualität der Simulationsergebnisse zu bewerten. Zu diesem Zweck werden zwei Kriterien entwickelt, wobei die Simulationsergebnisse beide erfüllen müssen, um zur Bewertung der Feldstärkeerhöhungen im Randbereich der Tropfen herangezogen werden zu können. Das erste Kriterium, ein globales Kriterium, wird "Integralkriterium" genannt und beinhaltet eine Bewertung des gesamten Integrationsweges auf der Isolierstoffoberfläche im Bereich des aufliegenden Tropfens. Allerdings liegen die wirklich interessierenden Punkte unmittelbar in der Nähe des Tropfens auf der Isolierstoffoberfläche, wo die erhöhte elektrische Feldstärke durch ein „lokales Kriterium“ bewertet wird. Aufgrund der Singularität im TP gehen die elektrischen Feldstärken dort gegen unendlich und können daher nicht für die Bewertung der Feldstärkeerhöhungen herangezogen werden. Die Betrachtung des elektrischen Feldes entlang der Oberfläche bei unterschiedlich gewählten Diskretisierungsraten hat ergeben, dass bis zu einem Abstand von 0,1 mm vom TP die elektrischen Feldwerte konvergieren; daher wird bis hierhin ein sehr präzises Ergebnis der Simulation unterstellt, und dieser Punkt wird Konvergenzpunkt (englisch convergence point (CP)) genannt. Die Auswertung der elektrischen Feldstärken im CP zeigt Feldstärkeerhöhungen bei vorhandenen Wassertropfen (wie bereits bei den Messungen und analytischen Betrachtungen festgestellt).

Die Abhängigkeit der elektrischen Feldstärke vom Kontaktwinkel und von der Tropfenform wird anhand von Messungen und Simulationen gezeigt. Für verformte Tropfen können die Feldstärken den achtfachen Wert der angelegten Grundfeldstärke erreichen, wobei überwiegend die Tangentialkomponente beeinflusst wird. Bei Betrachtung der Amplitude der lokalen Feldstärkeerhöhung muss die elektrische Leitfähigkeit der Polymeroberfläche an der entsprechenden Stelle berücksichtigt werden.

Zum Vergleich von Messung und Simulation sind nur die Absolutwerte der elektrischen Feldstärke von Bedeutung. Für die verformten Tropfen stimmen die Absolutwerte sehr gut mit der TE-Einsetzfeldstärke in Luft überein.

Das Alterungsmodell von Polymeren wurde auf die Region der Frühalterungsphase ausgedehnt. Darüber hinaus werden bei der Erweiterung des Alterungsmodells noch die Tropfenverformung, die Beeinflussung der lokalen Feldstärkeerhöhung und der Einfluss der Umgebungsbedingungen auf die Einsetzspannung berücksichtigt.

1 Introduction

The main goal of an electric power system is to generate and to transport the energy safely and efficiently. The insulation between the equipment components under high voltage and surrounding medium is one of the main tasks for high voltage technology. If the surrounding medium is air, the influence of condensation or atmospheric precipitations must be considered. These parameters influence the insulation properties of the insulating parts.

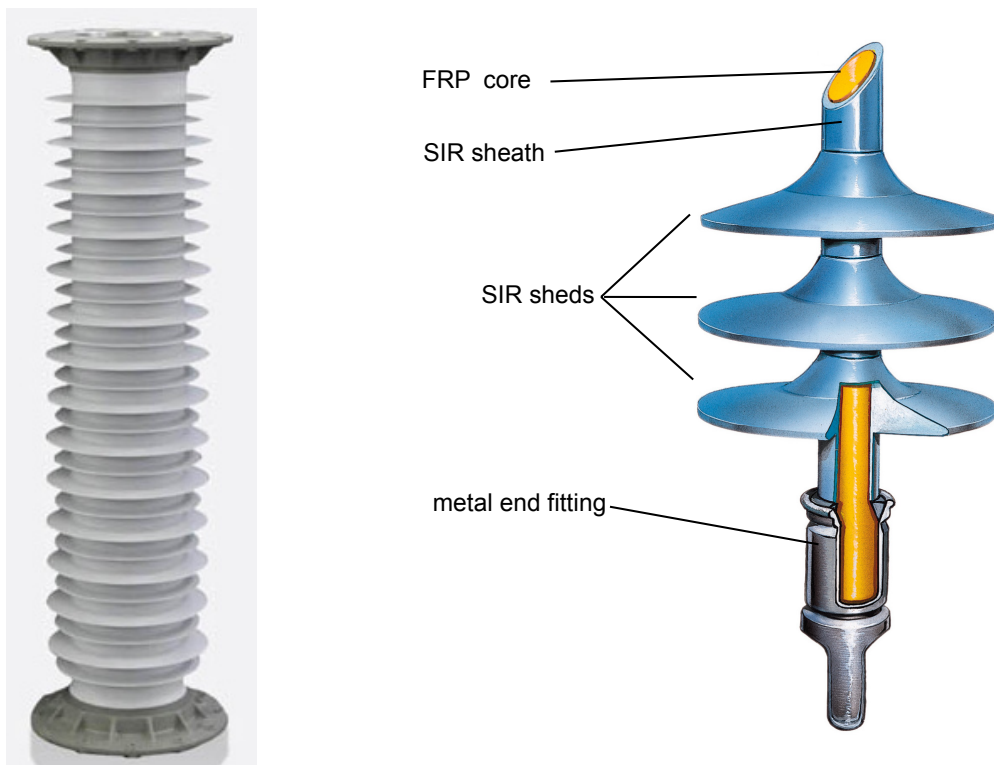
Consideration of the properties of the insulating materials to be used is an important part of the outdoor but as well for indoor insulator design process. Not only does the material have to be a very good dielectric capable of sustaining high electric stress over a long time but it must also withstand the, often severe, environmental effects imposed. It also must possess sufficient tensile, compressive and cantilever strength to support the loads applied and maintain its mechanical integrity over the life of the insulation [Vos2004].

Following the first porcelain insulators in the middle of the 19th century, porcelain remains the most widely used material for outdoor insulation today. Electrical porcelain is an inert and inorganic material and is therefore immune to degradation by environmental factors. Due to the glazure, the insulators surface is smooth and in this way inhibits the adherence of contaminants and facilitates natural washing by rain. Porcelain insulators are resistant to damage by electric surface discharges and leakage current activity. But, due to its brittle nature, porcelain is vulnerable to breakage, chipping and cracking. Another limitation are the low tensile and cantilever strength-to-weight ratios and the possibility of cracking and failure by thermal effects of power arcs. For certain insulator types, due to the intermittent puncture channel, the detection of electrical puncture is very difficult. Therefore, also toughened glass insulators are used. Here the resistance to puncture is higher and identification of faulty units is easy due to the tendency of shatter. On the other hand, the tendency to shatter makes it an ideal target for vandals. The mechanical characteristics of the glass insulators limit their use to certain applications. Later in the 1960s when aromatic resins with silanised silica flour fillers were introduced, epoxy resins were limited to indoor use. The chemical structures of the aromatic and cycloaliphatic epoxy resin are different. While the aromatic resin has the epoxid group linked to a carbon hydrate rest, the epoxide groups of cycloaliphatic resins are linked directly to the matrix. The last

one has improved resistance to UV radiation and therefore can be used also for outdoor insulation, in lightly polluted areas. The required metal fittings can be also embedded during the moulding process. Epoxy resin is an organic material and can suffer from degradation owing to electrical surface discharge activity. Disadvantages of epoxy resin insulators are the possibility of severe leakage current erosion, and usually they are limited to medium voltage and mainly indoor applications.

At the beginning of the 1970s the first composite insulators were developed. A composite insulator consists of a fiberglass (FRP) core which provides the mechanical strength, covered by a housing to protect the core from the environment and to yield the required electrical characteristics.

Two housing materials are mainly used: ethylene propylene diene monomer (EPDM) based and silicone rubber (SIR) based. Silicone rubbers have the unique property of



Directly moulded hollow core insulator

Modular design of line insulator with push over shed

Figure 1.1: Types of composite insulators [Lapp2009]

maintaining a water repellent surface even when severely contaminated. In **Figure 1.1** two typical designs of composite insulators are presented, where the housing material is silicone rubber.

Polymeric insulators are widely used because of their many advantageous properties: high contamination resistance, high tensile strength-to-weight ratio, an unattractive target for vandals and especially with silicone rubber housings, a high surface hydrophobicity. Water drops will be formed on the polymer surface when the insulator is exposed to rain and moisture, and hence the conductive contamination dissolved with water is discontinuous [Phi1999]. Hydrophobicity is transferred to pollution layers and after loss of hydrophobicity under severe environmental stress, like extreme continuous exposure to moisture; it will be recovered in a relatively short time.

However, around the water drops, the electric field is intensified. The water drop will be deformed and elongated along the direction of the electric field lines. The deformations will cause local electric field intensifications, the critical point will be the triple point between water drop, air and insulating material. This will be a starting point for partial discharges, finally leading to deterioration [Kei2003]. For outdoor as well as for indoor insulation materials, the electrical discharges between drops and surface are an important source of ageing.

2 Wetting Properties of Polymeric Surfaces

2.1 Wetting Theory

When a fluid comes in contact with a solid surface, a solid-fluid interface is formed between the phases, which mean that the fluid wets the solid surface. The wetting appearance of the solid surface is dependent on the degree of wettability of the fluid. A basic parameter to characterize the degree of wettability for a given fluid is the contact angle, which is the angle between the tangent to the drop contour in the triple point¹ and the solid surface (**Figure 2.1**).

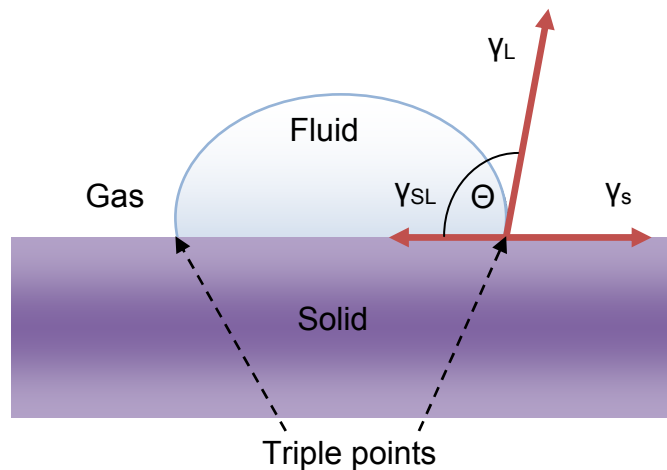


Figure 2.1: Fluid drop on a solid surface

Using the Young equation [Sch1996], the equilibrium relation of a liquid drop on a solid surface as function of four parameters is written:

$$\gamma_S - \gamma_{SL} = \gamma_L \cdot \cos \theta \quad (2.1)$$

where

γ_S – surface tension of the solid surface

γ_{SL} – interfacial tension of the fluid / solid surface

γ_L – surface tension of the fluid surface

θ – contact angle

The Young equation is valid only when the followings conditions are fulfilled:

¹ At the interface there is actually a triple line but in two dimensional representation there is a triple point. Therefore from now on triple point term will be used.

- the solid surface will not be deformed by the fluid drop
- the gravitational force is neglected [Sch1996]
- the solid surface is ideal, without any roughness or inhomogeneities.

The contact angle characterises two regions. One speaks about “wetting” if $\theta < 90^\circ$ and about “no wetting” if $\theta \geq 90^\circ$. The maximum possible value of θ is 180° , but in reality the contact angle will be always below the maximum value. The reason for that are the adhesion forces between the fluid volume and the solid body. Work of adhesion is defined as:

$$W_{AD} = \gamma_S + \gamma_L - \gamma_{SL} \quad (2.2)$$

whereas the work of cohesion is defined as:

$$W_C = 2 \cdot \gamma_L \quad (2.3)$$

When a fluid comes in contact with a solid surface, the surface tensions compete against the interfacial tensions. Both tensions aim to reach a minimum. The form of the fluid drop depends on the magnitude of parameters from the Young equation. The spreading coefficient, S , is defined as:

$$S = \gamma_S - (\gamma_{SL} + \gamma_L) \quad (2.4)$$

A positive S value means that the fluid will spread while a negative S value means the fluid drop will contact. Spreading will take place if wetting tension is greater than the surface tension of the fluid or if the adhesion between the fluid and the solid surface is bigger than the fluid’s cohesion:

$$S = W_{AD} - W_C > 0 \quad (2.5)$$

Complete wetting means that the fluid is spread and a closed fluid film is formed on the surface, while for incomplete wetting drops with a defined contact angle are formed.

2.1.1 Static and Dynamic Contact Angle

Two different types of contact angles are defined. The contact angle of a still fluid drop on a horizontal surface is the static contact angle. Usually, when no other information is given, the static contact angle is meant.

By contrast the dynamic contact angles θ_a (advancing angle) and θ_r (receding angle) can be defined at a drop rolling down on an inclined surface (**Figure 2.2 a**). It is also

possible to measure the dynamic contact angles on horizontal surfaces by increasing or decreasing the drop volume, respectively, as presented in **Figure 2.2 b**.

The static contact angle values are between the receding contact angle and the advancing angle, the relation is given in equation (2.6) as

$$\theta_r \leq \theta_s \leq \theta_a \tag{2.6}$$

The dynamic contact angles, especially the receding contact angle, correlate better with the electrical properties of the surface e.g. leakage current than the static contact angles [Lam2001]. Therefore the dynamic contact angle is used to evaluate the degree of hydrophobicity.

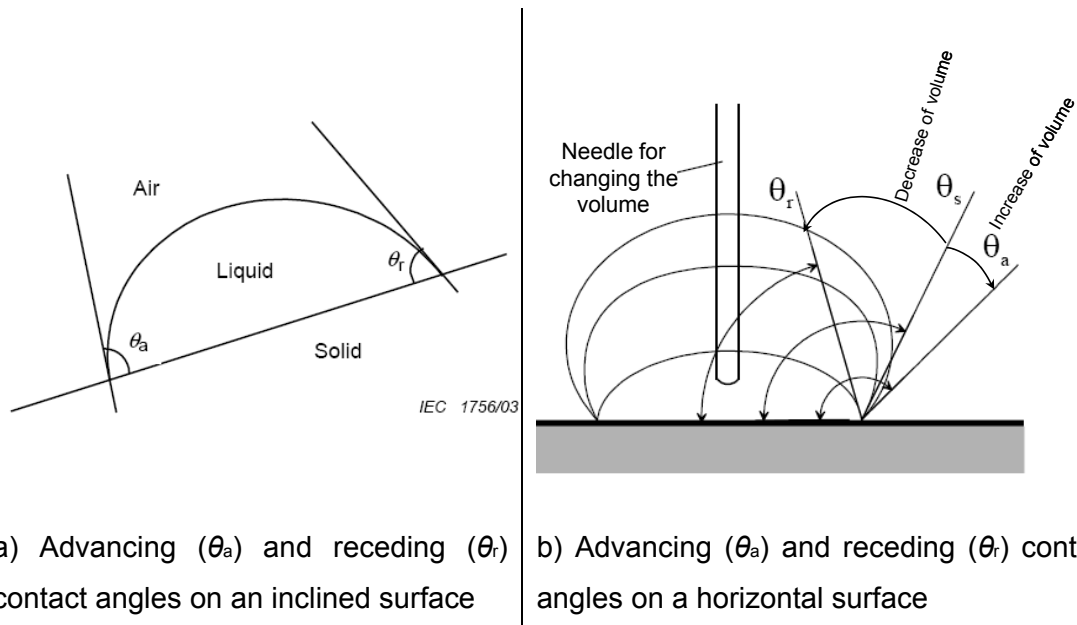


Figure 2.2: Dynamic contact angles [IEC/TS 62073]

2.2 Hydrophobicity on an Insulating Surface

2.2.1 Hydrophobicity Theory

The hydrophobic property of an insulating material is very important when speaking about the operating performance of the electrical equipment. On a hydrophobic surface no water film will be formed which will result in low leakage current between the high voltage and ground electrode. Therefore, hydrophobic polymeric surfaces contribute to the longevity of the insulating materials.

Table 2.1: Processes affecting surface hydrophobicity of a polymeric material

Mechanism	Causes	Effects/ Processes
Reversible changing of the chemical structure of the surface	Mobility of the molecular connections of organic chains Repellent forces between the polar water molecules and covalent groups [Kim1992], [Zis1964]	Temporary orientation of the hydrophobic group from the surface direction to the inside
Irreversible changing of the chemical structure of the surface	UV radiation Chemical and thermal effects due to partial discharges when water is present on the surface [Vla1991], [Kim1990], [Kin1989], [Sig1991], [Owe1986]	Depolymerisation, hydrolysis, wetting, oxygen bridging, oxidation and formation of polar radicals; hydrophobic groups splitting
Physical changing of the surface	UV radiation Erosive processes [Cha1994], [Hil2001], [Jah2003], [led1986],	Increase of surface roughness Local conglomeration of filler material
Pollution layer	Attachment of foreign particles on the surface Adhesion property of foreign particles No self-cleaning effect of the material Biological layer [Sch1992], [Kär1988], [Mal2005], [Win2006], [Wor2004]	Change of surface chemical structure, which is important for the hydrophobicity Increase of surface roughness Dissociation processes if water is present

The critical surface tension of a polymeric material with a chemical surface structure is $(6 - 35) \cdot 10^{-3}$ N/m. This value is smaller than the water surface tension ($72,8 \cdot 10^{-3}$ N/m), indicating that the polymeric material has a hydrophobic surface. The smaller the critical surface tension, the higher is the repel effect.

The critical surface tension is due to the organic group chains present at the surface of a polymeric material. The typical organic groups are carbon hydrate, CH_2 , CH_3 , ..., CH_n . The hydrophobicity of the polymeric material is higher when the hydrogen part in the organic groups is high and the number of groups with higher hydrogen contents is greater than the groups with lower hydrogen content.

The content of polar groups is also a relevant parameter, i.e. hydroxyl, at the polymeric surface. Due to the polar interaction with the water dipole, the adhesion forces will increase and so the hydrophobicity decreases. The hydroxyl groups are necessary for the polymerisation process and also result from ageing processes at the surface [Bit1986].

The dependence of the contact angle on chemical and physical reactions shows that the hydrophobicity is an instantaneous value and is not constant in time. During service the insulating surface is stressed by climatic and electrical factors and the surface condition changes, which usually will negatively affect the hydrophobicity. In **Table 2.1** some surface processes affecting hydrophobicity are presented. These are reversible and irreversible processes that can be caused by different factors.

The consolidated findings regarding the hydrophobicity property of the polymeric material presented in **Table 2.1** are the results of detailed investigations over the last years. The irreversible chemical and physical changes of surface structure of the insulating material can be concluded in one word: "ageing" [DIN 50035-1]. In **Chapter 3** the ageing processes taking place at the polymeric surface will be described.

2.2.2 Quantification of Hydrophobicity

Following a proposal of the STRI [STRI1992] hydrophobicity (or wettability) is categorized into six classes, named HC1 to HC 6. This classification was then introduced to [IEC 62073], here named wettability classes WC1 to WC 7. Each class is characterized by parameters given in **Table 2.2** and a photograph of the appearance in **Figure 2.3**. The evaluation of the insulating material surface condition is performed on the surface without electric field stress.

For wettability measurement three methods exist, differing in accuracy, simplicity, size of measured surface area and applicability and are as follows:

- the contact angle method;
- the surface tension method;

Table 2.2: Criteria for the determination of wettability class (WC) [IEC/TS 62073]

WC	Description
1	Only discrete droplets are formed. Their shape when viewed perpendicular to the surface is practically circular. This corresponds to $\theta_r = 80^\circ$ or larger for the droplets.
2	Only discrete droplets are formed. The major part of the surface is covered by droplets with a shape, as seen perpendicular to the surface, still regular but deviates from circular form. This corresponds to $50^\circ < \theta_r < 80^\circ$ for the majority of droplets.
3	Only discrete droplets are formed. The major part of the surface is covered by droplets with an irregular shape. This corresponds to $20^\circ < \theta_r < 50^\circ$ for the majority of droplets.
4	Both discrete droplets and wetted traces from the water runnels or water film are observed (i.e. $\theta_r = 0^\circ$ for some of the droplets). Less than 10 % of the observed area is covered by water runnels or film.
5	Both discrete droplets and wetted traces from the water runnels or water film are observed (i.e. $\theta_r = 0^\circ$ for some of the droplets). More than 10 % but less than 90 % of the observed area is covered by water runnels or film.
6	More than 90 % but less than 100 % of the observed area is covered by water runnels or film (i.e. small non-wetted areas/spots/traces are still observed).
7	Continuous water film is formed over the whole-observed area.

- the spray method.

Considering **Chapter 2.1**, there are only two situations, wetting and no wetting. Thus, when the contact angle $\theta < 90^\circ$, the surface is hydrophilic and when $\theta \geq 90^\circ$ the surface is hydrophobic. But this classification is too rough for technical applications, where the aim is low wettability. Therefore, in [IEC/TS 62073] three situations and exact borders are given:

a) Hydrophobic surface (not wettable)

- high value of receding contact angle ($> 80^\circ$)

- low value of surface tension (< 30 mN/m)

- low WC value (WC = 1 or WC = 2)

b) Intermediate surface (semi-wettable)

- intermediate value of receding contact angle (10° to 80°),

- intermediate value of surface tension (30 mN/m to 60 mN/m),
- intermediate WC value (WC= 3 to WC = 5).

c) Hydrophilic surface (wetable)

- low value of receding contact angle ($< 10^\circ$),
- high value of surface tension (> 60 mN/m),
- high WC value (WC = 6 or WC = 7).

The hydrophobicity is influenced by several factors which were not considered in the Young equation as roughness of the surface, gravity force, chemical inhomogenities, humidity penetration and others.

During service the polymeric surface tends to deteriorate, negatively affecting the hydrophobicity of the material. The hydrophobicity loss will influence the electrical properties of the wetted surface, so the breakdown voltage, PD inception voltage will be lower and PD charges and leakage currents higher [Qui1993]. But the polymeric surfaces have a self recovery property, which is presented in the following section.

2.2.3 Loss and Recovery of Hydrophobicity on Polymeric Surfaces

Polymeric materials have an intrinsic hydrophobicity on their clean surface. Under operating conditions it can be lost directly (changing the hydrophobic surface) or indirectly (covering the hydrophobic surface). After a healing phase polymeric material is able to recover it and is named recovery process.

After indirect loss of hydrophobicity silicone rubber can show the so-called hydrophobicity transfer: the pollution layer becomes hydrophobic. The speed of the transfer depends on the type of polymeric material as well as on the thickness and the kind of the pollution layer [Kin1989]. If the roughness of the pollution layer is higher than that of the polymeric material, a higher grade of hydrophobicity is possible [Bus1984]. This is due to the inverse capillary effect. Some rare kinds of pollution layers cannot be made hydrophobic; e.g. pure salt.

Hydrophobicity transfer happens due to the diffusion of low molecular weight (LMW components) out of the silicone rubber into and onto the pollution. The LMW components consist of polydimethylsiloxane (PDMS) of different chain lengths and structures [Gou1998]. LMW components content and distribution of the chain lengths

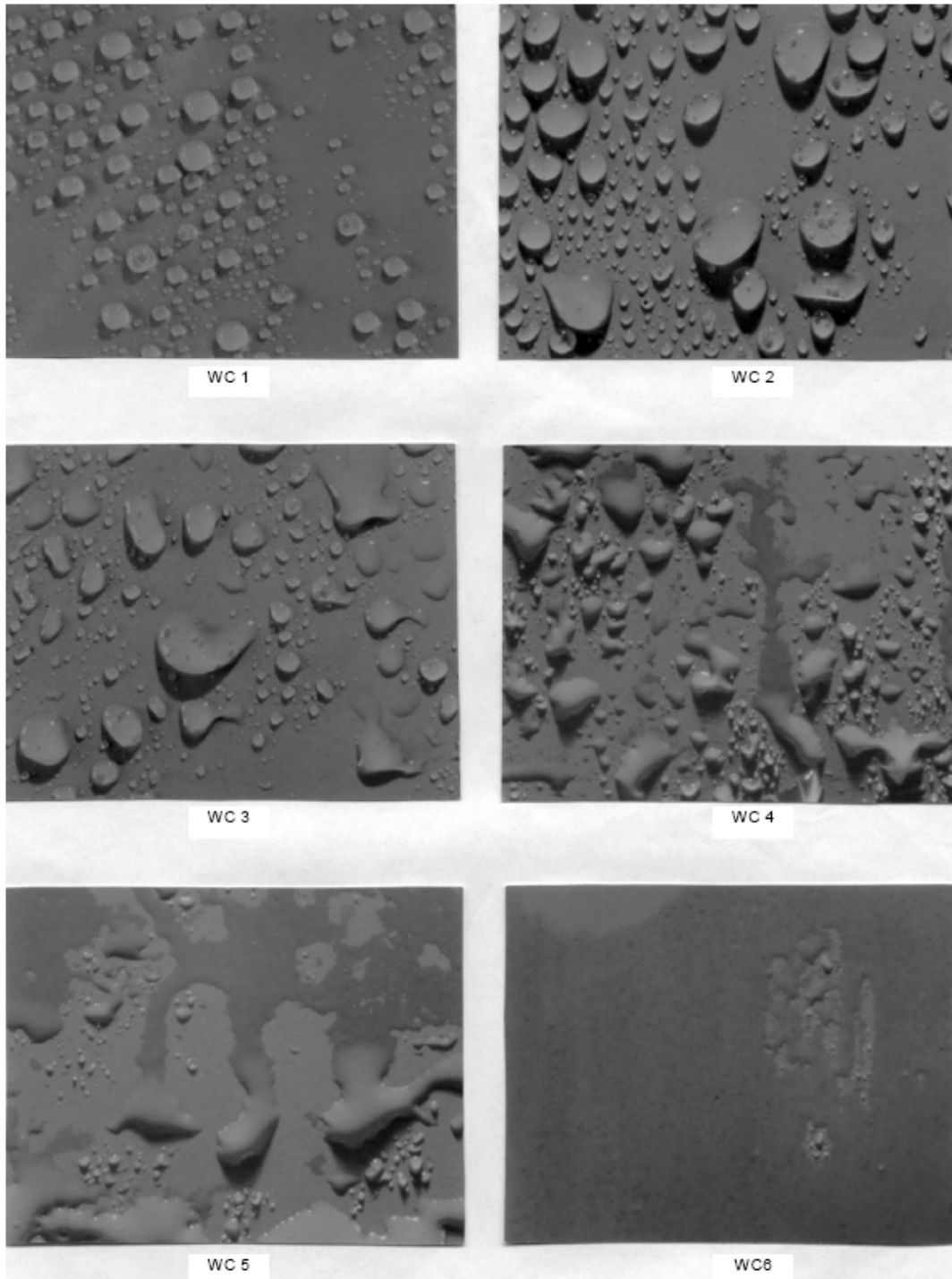


Figure 2.3: Typical examples of surfaces with wettability class (WC) from 1 to 7 [IEC/TS 62073] depend on the type of silicone rubber. From a typically 2-compound room temperature vulcanized (RTV) silicone rubber, approximately 5% LMW components can be extracted. The high temperature vulcanized (HTV) rubber with a 3 times higher filler grade contains 2,5% less LMW components. It has been observed that most 20 year old insulators still have the ability to transfer hydrophobicity as fast as new ones. The silicone rubber still contains the basic LMW components [Kin1989].

Natural UV radiation does not destroy the Si-O backbone because the silicon-oxygen bond has high bond energy. Only energy-intensive radiation with a wavelength of 900 nm and below can attack it. The Si-C bond between the siloxane backbone and methyl groups may be attacked, but obviously it has no influence on the hydrophobicity.

Based on the transfer of the hydrophobicity different possibilities for improving the surface behaviour of epoxy resins are researched. The utilization of a surface treatment is leading to an improvement in the hydrophobicity of epoxy resin cast without any negative influence on the mechanical behaviour of the material. Another method enables an intrinsic hydrophobicity including recovery and transfer of hydrophobicity [Kal2005].

3 Electrical Ageing Processes on Polymeric Material

Ageing is defined as slow and irreversible alteration of a material's chemical or physical structure. This alteration has normally a detrimental effect on the material properties. It leads to gradual loss of the design function and ultimate failure or unacceptable loss of efficiency. For polymeric materials, the combination of electrical with climatic stress, especially pollution layer and moisture, will cause ageing of the surface. The climatic stress is different for indoor and outdoor insulation. For indoor insulation the following are considered as climatic parameters: temperature, humidity, condensation, ozone, acids and industrial pollution. Therefore dimensioning of the electrical equipment is made considering 0,5 kV/cm as the mean value of electric field stress. For outdoor insulation, besides the climatic parameters described above, fog, rain, dew, snow and ice must be considered, in addition. In this case the maximum permitted electrical stress is 0,36 kV/cm [Bär1993]. The two insulation types presented can be differentiated by intensity, development and effects of the influence of climatic factors. From the time development point of view, the ageing processes can be divided into three periods: early ageing, late ageing and tracking time [Kal1998].

In order to describe the ageing processes different models were developed. In [Mül1985], the ageing processes on insulating materials, from physical and chemical point of view are described. Moreover the behaviour and the influence of the pollution layer are considered. Based on [Mül1985], in **Figure 3.1** the ageing model of polymeric surfaces under electrical and environmental stress is presented.

3.1 Early Ageing Processes on Polymeric Surfaces

When water drops are present on polymeric surfaces stressed by an electric field, the water drops are moving in the direction of the electric field. The deformation of the drop will induce the contact angle decreasing at the triple points of the drop. In these regions the electric field is intensified locally up to the partial discharge (PD) inception electric field strength. The ageing process starts with the ignition of the PD. The discharges will dissociate the air into ozone and nitrogen oxides which will form acids in the presence of water. These ageing processes are known as “electrolytic PD erosion” and include the chemical degradation of the surface as well as the formation of soluble nitrates as “self pollution layer”.

Due to light moisture on the polymeric surface, the electrical strength of the surrounding air is only locally exceeded, but this can initiate low intensity discharges due to avalanche formation. These local surface discharges will influence significantly the global appearance of the surface ageing. Discharges are also triggered by electro-hydro-dynamic processes, as splitting of one water drop in two smaller drops or water drop flow, which are taking place on the surface. In particular, by water drop flow the discharge level and intensity is higher [Ock1986], whereas by intensive moisture on the surface, the flowing processes are also intensified and local ageing appearances will be visible on the surface.

Due to evaporation the water drops become smaller with time. The change of the drop volume will also change the contact angle of the drop and the PD inception conditions, respectively.

A typical ageing process in this phase is the loss of material due to erosion on the surface which results in an increase of surface roughness and loss of hydrophobicity. The conductivity of the pollution layer will increase and the early ageing processes will develop towards late ageing processes. A detailed description of the early and late aging processes at the insulating surfaces, from electrical and chemical point of view is given in [Kal2005].

PD activity at the surface of polymeric material is not the only source of gas dissociation. Discharges in material voids, at sharp conductive edges or sliding discharges not taking place on the surface, due to the gas diffusion, contribute to the increasing in interface conductivity.

3.2 Late Ageing Processes on Polymeric Surfaces

As soon as thermal effects of the leakage current appear, late ageing processes on the polymeric surface will start. The PD activity is intensified and the leakage current values are higher. At a leakage current of several milliamperes the water drops are evaporated and the dry zones are formed. The dry zones will sustain constant discharges on the surface which are characterized by mobility, due to the discharge propagation and formation of new dry zones. The stabilization of the discharges will lead to thermal surface deterioration. The appearance of late ageing on the surface is characterized by deep erosion lines and tracking. Tracking paths are electrically conductive and may lead to flashover. Ageing tests have shown that local thermal stress by impulse discharges is sufficient to cause thermal depolymerisation – this is

considered the main degradation method for testing of insulator materials [Gus2002], [Gub2005].

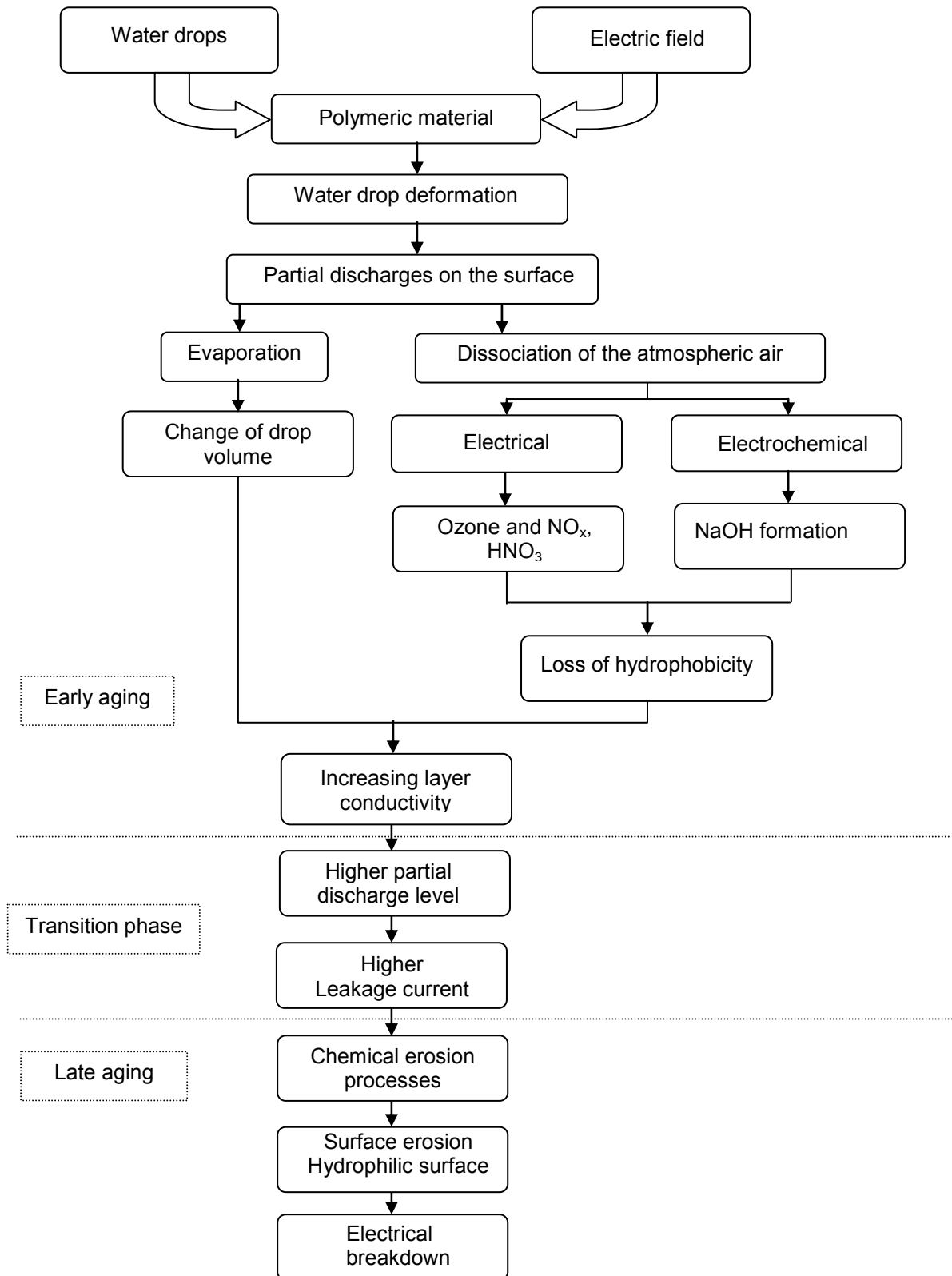


Figure 3.1 : Ageing model of polymeric surfaces under electrical and environmental stress

However, increase of the pollution layer or higher tracking stress will not obligatorily degrade the surface more intensively. For the degradation process, the duration of stress in the same place on the insulating material is more important, even more than the leakage current value [Sei2006].

Strong discharges on a polymeric surface in the presence of moisture are mobile, therefore it will not last long enough to cause ageing. In **Table 3.1** the material deterioration as a function of PD intensity and duration is presented.

Table 3.1: Material deterioration as a PD intensity and duration dependence

PD intensity	Duration of stress	Material deterioration
Light	Short \Rightarrow mobile	slight
Heavy	Long \Rightarrow stable	intensive

The effect of small discharges, which appear on a polymeric surface in the presence of water drops over a longer time is worse than of strong mobile discharges and therefore it is important to avoid small discharges.

4 Partial Discharges

4.1 Definition of Terms

In high voltage terminology, the items a “complete” and an “incomplete” breakdown of the insulation stressed by electric field are used for two different phenomena. While during the “complete” breakdown the insulation fails almost completely, bridging the electrodes by a low ohmic resistance, during an “incomplete” breakdown only part of the insulation fails, resulting in a “partial breakdown” The still intact part of the insulation can withstand the electric field stress. The occurrence of such a breakdown is named “partial discharge” [Kön1993].

The reasons for the appearance of partial discharges are local enhancements of the electric field (for example by conductive tips, electric field displacement) or locally decreasing electrical strength (gas bubbles in insulation material). The behaviour of the discharges is different for alternating voltage stress, direct voltage stress and impulse stress. Partial discharges occurring in gases around electrodes of small radii of their curvature and those on the surface of a solid insulating material are named external partial discharges.

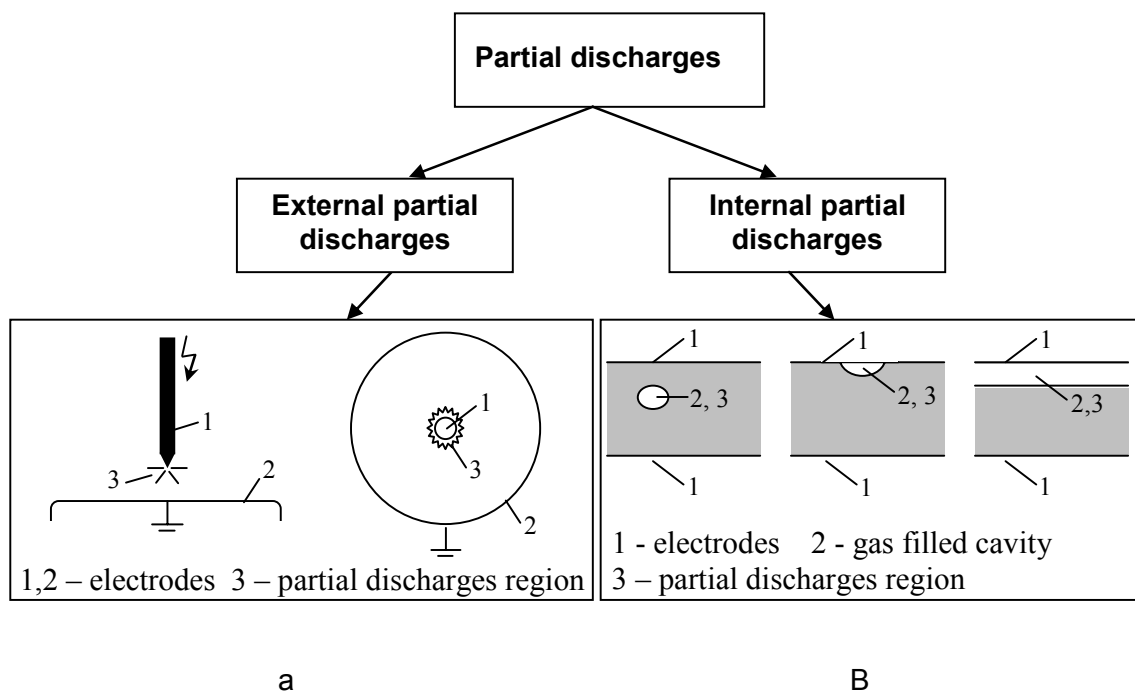


Figure 4.1: Partial discharge categories [Kön1993]

If the partial breakdowns arise in solid or liquid insulating material they are named internal partial discharges, see **Figure 4.1**. Due to the fact that at water drops on the insulating surface only external PD can occur, in this work only external partial discharges are considered.

During a partial discharge measurement, beside the measured signals, background noise, a form of noise pollution also appears. In order to minimize it, the partial discharge measurements are usually made in an electromagnetically shielded chamber [Küc2005].

In the following section the equivalent circuit and parameters of external partial discharges will be presented in detail.

4.2 External Partial Discharges

External partial discharges occur at sharp edges of an electrode where the electric field is strongly inhomogeneous. The rod-plane configuration is the typical electrode arrangement used to describe the external partial discharge mechanism. If many parallel discharge sites are considered, then a coaxial gap system (corona cage) is used, as in **Figure 4.1.a**. In the equivalent circuit, **Figure 4.2.a**, a rod-plane arrangement is considered. C_1 represents the capacitance attributed to the gas gap which discharges completely each time the voltage reaches u_z , the breakdown voltage of the gap F.

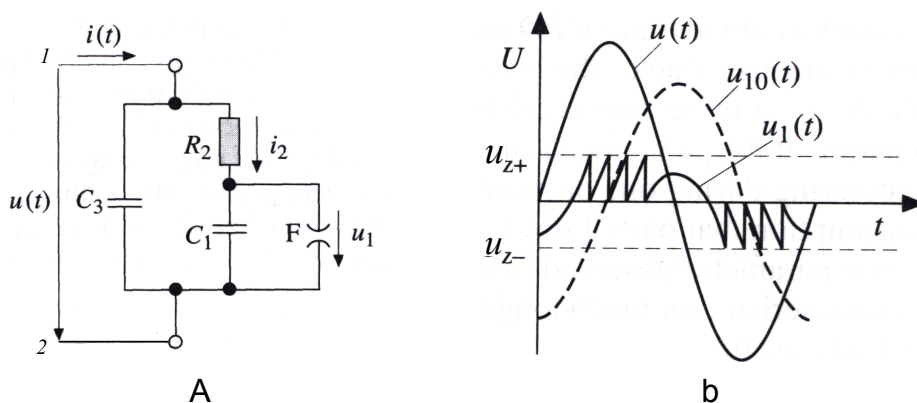


Figure 4.2: External partial discharge equivalent circuit [Kön1993]

a – capacitive equivalent circuit

b – voltage waveform in the equivalent circuit for pulse-like external partial discharges

Due to the presence of the electric field the charge carries formed at the tip of the discharge are travelling, having a certain conductivity which is represented by R_2 in the equivalent circuit. C_3 is the capacitance of the electrode configuration.

The external partial discharge depends on the instantaneous value of the applied voltage, as shown in **Figure 4.2.b**. Due to the polarity effect, considering a tip, the partial discharge will start in the first negative half wave and the breakdown in the positive half wave.

4.3 Measurement Method of Partial Discharges

In general PD inside an operating resource cannot directly be measured at the place of their appearance. There are different methods of measurement of PD-activities. Depending on the measurement method, they can be divided into:

- acoustic PD-measurement
- optical PD-measurement
- chemical analyses (e.g. gas-in-oil-analysis)
- electrical PD-measurement

The first three methods are very simple and effective. But they are not appropriate to a quantitative measurement. Therefore partial discharges are determined with electrical measuring devices. The various types of electrical PD measuring equipment are classified in **Figure 4.3**. Depending on the application and measuring conditions, which for instance are given by the external interference level, one type of equipment is suitable. If the PD spectrum is spread, e.g. up to 100 kHz, the indication of a PD meter based on the selective wideband principle with an upper cutoff frequency of 400 KHz is no longer proportional to the charge. If the spectral amplitude density $F(f)$ of the PD pulse occurring on the specimen's terminals decreases rapidly within the bandwidth of a narrow band or selective wide band instrument, then the accuracy of apparent charge values can be affected.

The high frequency PD pulses are superposed on the test voltage and must be appropriately decoupled out from the test circuit. Therefore according to [IEC 60270] three basic circuits are given for PD tests. The most common circuit is presented in **Figure 4.4**. in which the specimen is represented as capacitor C_a .

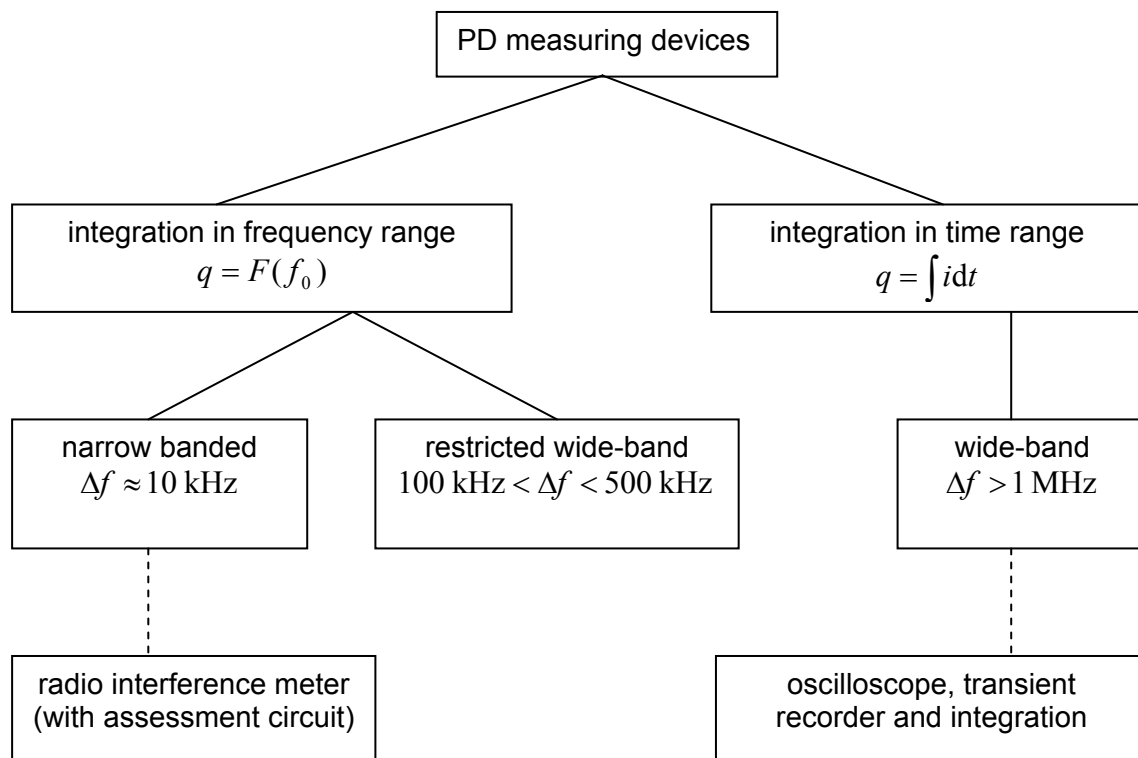


Figure 4.3: Classification of PD meters for measurement of apparent charge q [Kön1993]

The PD pulses appear on the measuring impedance Z_m via the coupling capacitor C_k . The measuring impedance (quadrupole) consists of a resistance R of the order 100Ω connected in parallel with an overvoltage arrester for protection of PD meter and an inductance which leaks-off the low frequency alternating current. Since during measurements of short duration PD pulse effects on the travel time and reflection should be considered, the value of the resistance R should be matched with the surge impedance of the cable connected to the measuring instrument. The quadrupole serves to separate the high frequency current of the partial discharge signals from the power frequency current of the capacitor.

The coupling capacitor is an important element of the test circuit, the return path for the PD pulses is made through it. It must be designed to withstand the full test voltage, PD free and have low inductance. Its capacitance shall be as high as possible in comparison with stray capacitance of the test circuit and the specimen capacitance in order to achieve a high measuring sensitivity.

The PD pulses are coupled to the measuring unit which is computer controlled. The PD pulses are converted in charge and the displayed PD values are usually in pC.

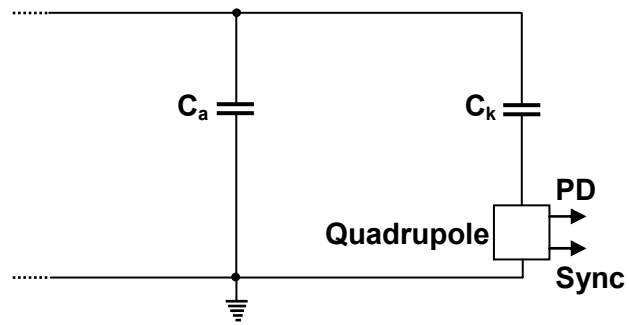


Figure 4.4: Basic PD test circuit

Partial discharge measurements are relative measurements and therefore require a calibration. Also the entire signal path from the test specimen to the instrument and some instrument properties as filters introduce an overall attenuation which is not exactly known. To calibrate the PD measurement system, a pulse source, injecting a given amount of charge, is connected to the test object. When the displayed charge value and the calibration pulse charge are equal, the measurement system has a calibrated sensitivity.

5 Water Drops under Electric Field Stress

5.1 Behaviour of Water Drops under Electric Field Stress

The behaviour of water drops under electric field stress is a classical problem. The first research work in this field was started at the beginning of the last century as investigations on phenomena occurring during a thunderstorm. In 1931 Macky described the appearance of water drop deformations and discharges [Mac1931].

The considered water drops are uncharged drops; no electric field stress is present. The surface curvature of a water drop surface leads to a net component of surface tension forces acting normal to the centre of the water drop [Ber1990]. In order to compensate the surface tension forces with the pressure force, the surface must be curved. When all forces are balanced, the resulting equation is known as Young-Laplace equation. The differential pressure p_k can be expressed as a function of radii of curvature r_1 , r_2 , and the surface tension γ . The expression is valid when a curved surface is considered.

$$p_k = \gamma \cdot \left(\frac{1}{r_1} + \frac{1}{r_2} \right) \quad (5.1)$$

As long as the surface tension is lower than the cohesive forces, the fluid volume will have a sphere form, the radii are $r_1 = r_2 = r$, and p_k becomes

$$p_k = \frac{2 \cdot \gamma}{r} \quad (5.2)$$

The differential pressure p_k of a drop surrounded by a gas atmosphere will contribute to the increase of the drop's internal pressure:

$$p_i = p_a + p_k \quad (5.3)$$

where

p_i - internal pressure; p_a - external pressure

If electric field stress is present, due to the big difference between the relative permittivity of the involved materials ($\epsilon_{r, \text{water}} : \epsilon_{r, \text{air}} \approx 81:1$) an electrostatic force will act on the water drop surface. In the general case of an interface between two dielectrics the tensile stress in the material of smaller permittivity can be expressed as [Küp1990]:

$$\sigma = \frac{1}{2} \cdot (\epsilon_2 - \epsilon_1) \cdot \left(E_{\text{tan}1}^2 + \frac{\epsilon_1}{\epsilon_2} \cdot E_{\text{n}1}^2 \right) \quad (5.4)$$

where

σ - tensile stress

ϵ_1, ϵ_2 - permittivity of the materials

$E_{\text{tan}1}$ - tangential component of the electric field in material 1

$E_{\text{n}1}$ - normal component of the electric field in material 1

For the water drop deformation only the component perpendicular to the surface, namely the normal component of the electric field, will influence the tensile stress. Considering also $\epsilon_2 \gg \epsilon_1$ (Water – Air) the expression (5.4) becomes

$$\sigma = \frac{1}{2} \cdot \epsilon_0 \cdot E_{\text{n}1}^2 \quad (5.5)$$

Thus the tensile stress of the water drop surface is proportional to the square normal component of the electric field.

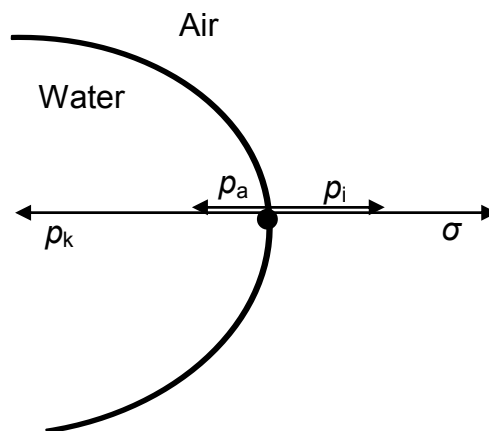


Figure 5.1: The equilibrium requirements of a point on the deformed drop surface

The normal component of the electric field on the surface of a water drop is not constant over the whole surface. In order to fulfil the equilibrium condition of water drop stability, see **Figure 5.1**, the following equation must be valid in every point of the water drop surface [Bra1971]:

$$\sigma = p_k - (p_i - p_a) \quad (5.6)$$

High tensile stress caused by the high normal component of the electric field, i.e. at poles of the water drop, must be compensated by a higher differential pressure p_k . According to (5.1) this is possible if the radii of curvature become smaller. Therefore a free drop under the influence of an electric field will take the form of an ellipsoid in the direction of the electric field lines [Ada1990]. The degree of deformation can be calculated as a ratio of the minor and major axis of the ellipsoid. Using a numerical model the ratio of the ellipsoid axes can be calculated [Tay1964]. The higher the electric field, the higher is the degree of deformation. There is a maximum limit for a stable deformation. If the electrical stress exceeds this limit, the equilibrium condition is not fulfilled anymore and the free drop becomes unstable. The characteristics of water drop instability are presented in **Chapter 5.2**. [Tay1964] and [She1988] found experimentally and theoretically that an uncharged water drop becomes unstable when

$$E = c \cdot \sqrt{\frac{\gamma}{\epsilon_0 \cdot r}} \quad (5.7)$$

where

E - critical electric field stress in V/m

r - radius of the drop before deformation

γ - surface tension of the fluid in N/m

c - constant

From equation (5.7) it can be concluded that the critical electric field stress increases with increasing surface tension and decreasing radius.

Different authors have estimated c with a small difference, except for [Kam1993] as is presented in **Table 5.1**. Kamra measured water drops falling at their maximum velocity in a horizontal electric field. Thus the water drops must have deformed in the horizontal direction before the electric field was applied. Their measured value of the constant c is lower than those presented by other authors. The theoretical calculations by Taylor are

based on the assumption that the drop is spheroid before its disintegration, and therefore the constant value is smaller than other values. [Abb1969] demonstrated that Taylor's spheroid assumption accurately predicts the electric field necessary to disintegrate charged water drops.

Table 5.1: Constant c of equation (5.7) by different authors

Author	Constant c	Method
Kamra [Kam1993]	0,273	Experimental, drops suspended by vertical winds in a horizontal electric field
Nolan [Nol1926]	0,414	Experimental, free falling water drops in a horizontal field
Macky [Mac1931]	0,42	Experimental, free falling water drops in a vertical field
Sherwood [She1988]	0,454	Theoretical
Wilson [Wil1925]	0,455	Experimental, soap bubble on a wet aluminium plate in a vertical electric field
Taylor [Tay1964]	0,461	Theoretical

Water drops on hydrophobic surfaces behave in a similar way to that of water drops in the free space. According to [Wind1994] the electrohydrodynamic behaviour of water drops in a free space can be simulated by water drops on a hydrophobic surface. The electric field necessary to disintegrate a water drop on a hydrophobic surface is the same as for a water drop in the free space and can be calculated using (5.7) with $c \approx 0,4$ which is close to the value of [Nol1926] and [Mac1931].

5.2 Discharge Mechanism at the Water Drops

The movement of the water-air boundary on the insulating surface under the influence of the electric field can influence the starting conditions of the discharge processes.

When the critical electric field at the water drop is reached the drop becomes instable. The instability of the water drop can be characterized by:

- formation of conical tips at the poles of the water drop
- development of threads on the drop surface
- splitting into two or more small drops.

The discharge development at the water drops was described by [Mac1931] as starting from the conical tips of the water drops and was said to be comparable with a discharge at a metal tip having positive or negative polarity. At a later stage the oscillographic technology became more precise and [Eng1984] proved that the assumptions in [Mac1931] are valid only for positive polarity. For discharges at negative poles some differences were observed in comparison with negative metal tips. The explanation given by [Eng1948] was that water does not contain free electrons and therefore a stable negative tip discharge is not possible.

Starting from these considerations, the discharge mechanism for an inhomogeneous field can be considered in order to describe the discharge mechanisms taking place at the water drops. The subsequent sections will deal with the ionization coefficient, the attachment coefficient, the second emission coefficient as well as the Streamer mechanism.

5.2.1 Ionization Coefficient

For a sufficiently long mean free path and appropriate field strength, the electrons can, in collision with a neutral molecule, have such a large kinetic energy ΔW that the molecule is ionized and a further electron is released. The collision is successful if ΔW attains at least the ionization energy W_i :

$$\Delta W \geq W_i \quad (5.8)$$

The mean value of ΔW is calculated from the partial voltage $\Delta U = E \cdot \lambda$ and the mean free path $\lambda_{m,e}$ of the electrons; for atmospheric air $\lambda_{m,e}$ is about 10^{-6} m. The condition for ionization is written as:

$$E \cdot \lambda_{m,e} \geq U_{ion} \quad (5.9)$$

where $U_{ion} = W_i / e$ is the ionization voltage of the air.

If the ionization condition is fulfilled, an independent multiplication process of the electrons by collision ionization sets in. Depending on the electric field strength, a certain number dn of new electrons is produced over a distance dx :

$$dn = \alpha \cdot n(x) \cdot dx \quad (5.10)$$

$\alpha = \alpha(E)$ is called the ionization coefficient of the electrons.

For a primary electron number n_0 and inhomogeneous field, the integration gives:

$$n(x) = n_0 \cdot \exp\left(\int_x \alpha dx\right) \quad (5.11)$$

The exponential increase of the electron number is named electron avalanche. At the head of the avalanche electron density may be very high and for a high number of carriers can cause great concentration of field lines. Behind the head of the avalanche the positive ions remain, see **Figure 5.2**. These move towards the cathode, where they may liberate secondary electrons under certain conditions.

The real free paths λ_v of the individual electrons constitute a statistical distribution, therefore λ is the mean value by definition. The probability that an electron of the mean free path λ will travel a distance greater than or equal to λ_v is taken to be $\exp(-\lambda_v / \lambda)$. Ionization by a single electron occurs only when $\lambda_v \geq U_{\text{ion}} / E = \lambda_1$. Over a distance x there is an average of x / λ collisions, but the number of ionizations is a factor $\exp(-\lambda_1 / \lambda)$ smaller.

The ionization coefficient α can be calculated as:

$$\alpha(E) = \frac{1}{x} \left[\frac{x}{\lambda} \exp(-\lambda_1 / \lambda) \right] = \frac{1}{\lambda} \exp(-U_i / E \cdot \lambda) \quad (5.12)$$

Since the mean free path is inversely proportional to the pressure p at constant temperature the ionization coefficient is expressed:

$$\frac{\alpha(E)}{p} = A \cdot \exp(-B \cdot p / E) \quad (5.13)$$

where A and B are constants. In the literature there are several values for the constants A and B. In **Chapter 5.3** a comparison of the existing values is presented.

5.2.2 Attachment Coefficient

In electronegative gases negative ions are formed by the attachment of electrons on neutral molecules. The collision process over a distance x requires

$$\eta \cdot n(x)dx \quad (5.14)$$

electrons; $\eta = \eta(E)$ is called attachment coefficient of the electrons.

The attachment coefficient can be expressed also like a function of E/p and constants A and B:

$$\eta = A \cdot p \left\{ 1 - e^{-\frac{B}{E/p}} \right\} \quad (5.15)$$

The difference between the ionization coefficient and the attachment coefficient is the effective ionization coefficient:

$$\alpha_e = \alpha - \eta \quad (5.16)$$

The effective ionization coefficient is decisive for the production of charge carriers. In air the effective ionization factor becomes positive at $E/p = 25 \text{ kV/cm} \cdot \text{bar}$, i.e. above this value a positive balance in charge carriers occurs.

5.2.3 Second Emmision Coeficient

The voltage on an electrode arrangement in gases can only be increased to the point where a breakdown occurs, i.e. a change over to a self-sustaining discharge. This differs from the non-self-sustaining discharge in that the charge carriers required along the path are created by the mechanism itself rather than liberated by external ionization. According to Townsend, ignition of gas discharge in a homogeneous field can be expressed as new electrons produced by secondary emission at the cathode. Secondary electrons can be created by incident ions or photons. If the supply via positive ions is the prevailing process then the number of secondary electrons n_{sec} will be proportional to the number of positive ions n_+ incident on a certain cathode region:

$$n_{\text{sec}} = \gamma_s \cdot n_+ \quad (5.17)$$

γ_s is the secondary emission coefficient. Depending on the experimental conditions γ_s can take values in the range $10^{-8} \dots 10^{-1}$.

The Townsend model is based on the assumption that an avalanche produced by n_{e0} primary initial electrons in the vicinity of the cathode, on crossing the spacing s , generates a total of

$$n_{e0}(e^{\alpha s} - 1) \quad (5.18)$$

positive ions. On striking the cathode, by secondary emission these release

$$\gamma_s \cdot n_{e0}(e^{\alpha s} - 1) \quad (5.19)$$

secondary initial electrons. If this number is larger than the original initial electrons, the current in the configuration increases rapidly without any external assistance, i.e. the gap breaks down.

The condition for ignition follows directly from this:

$$\gamma_s (e^{\alpha s} - 1) \geq 1 \quad (5.20)$$

$$\text{or } \alpha s = \ln(1/\gamma_s + 1) \quad (5.21)$$

The right-hand side of the equation (5.21) hardly changes in the usual ranges of γ_s , and so the ignition conditions for a homogeneous field becomes [Kind1985]:

$$\alpha s \geq k \quad (5.22)$$

where $k \geq 2,5$. The analogous derivation for the inhomogeneous field gives [Sch1923]

$$\int_0^s \alpha dx \geq k \quad (5.23)$$

In both cases α depends on the electric field strength, whose value on developing the electrical discharges is known as the breakdown field strength. For an inhomogeneous field the integration must be done along the expected breakdown path; this is the line of force along which the above integral yields the highest value. If the ignition condition is already fulfilled for $x < s$, then at least the inception voltage is attained.

In electronegative gases the loss of electrons by attachment must be taken into account. Derivation of the ignition condition for the homogeneous field thus leads to the expression [Mos1978]:

$$\gamma_s (\exp[(\alpha - \eta)s] - 1) \geq \frac{\alpha - \eta}{\alpha} \quad (5.24)$$

Analogous to (5.22), the ignition condition follows approximately with $\alpha_e = \alpha - \eta$ as:

$$\alpha_e s \geq k \quad (5.25)$$

5.2.4 Streamer mechanism

By increasing the number of electrons from the starting avalanche from 10^6 to 10^8 , the electric field changing near the electron avalanche can no longer be neglected, see **Figure 5.2**. The slow positive ions form the avalanche tail and the fast electrons form the head of the avalanche. The forward growth of the discharge is accelerated by the photo-ionization process preceding at the speed of light, reaching values of 1...10 m/ μ s. Due to the space charge, at the head of the avalanche an electric field intensification $E(x) = E_{\max}$ will be present, where E_0 is the applied field. Therefore, the impact ionization processes and the recombination processes also increase respectively.

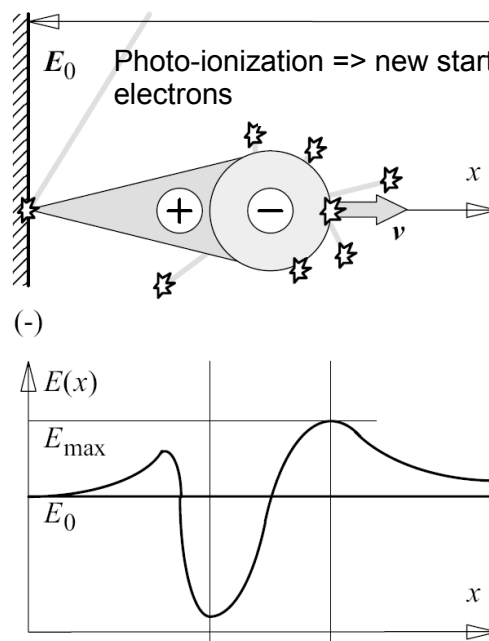


Figure 5.2: Electric field distortion due to the space charge of an electron avalanche [Küc2005]

As is presented in **Figure 5.2**, due to photo-ionization the electrons released from the initial avalanche will be the start electrons for secondary avalanches. From the sum of the avalanches, a conductive streamer is developing, see **Figure 5.3**.

The necessary condition for a breakdown development is that the electron's formation through impact ionization must be predominant over the electron's attachment, i.e.

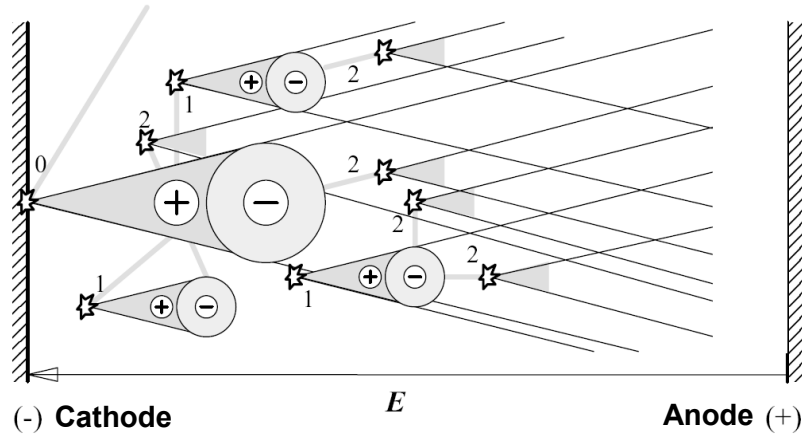


Figure 5.3: Development of a ionization channel (Streamer mechanism)

0, 1, 2 – start points for avalanches developed through photo-ionization [Küc2005]

the effective ionization coefficient, α_e must be bigger than zero. Also the critical number of electrons

$$N_{cr} = 10^6 \dots 10^8 \quad (5.26)$$

must be achieved. The ignition condition for an inhomogeneous field is analogous to the Townsend mechanism and can be written:

$$\int_0^d (\alpha - \eta) dx \geq \ln \{N_{cr}\} = 14 \dots 18 \quad (5.27)$$

In areas with higher electric field strength, the impact ionization processes are dominant ($\alpha > \eta$) and in areas with lower electric field strength the attachment processes are leading ($\alpha < \eta$), see **Figure 5.4**. The presented considerations are valid for an inhomogeneous field with negative and positive tip.

In the following the positive and negative polarity effect of a tip-plate arrangement will be presented, see **Figure 5.5**. First the mechanism in an arrangement of a positive tip will be analyzed.

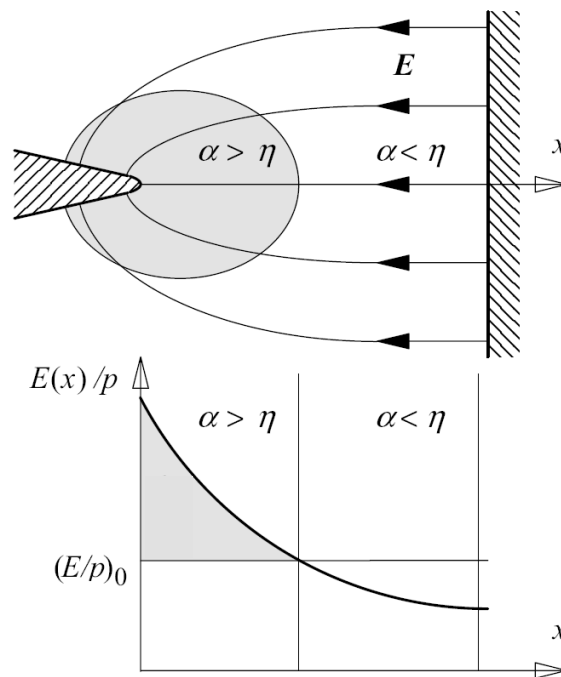
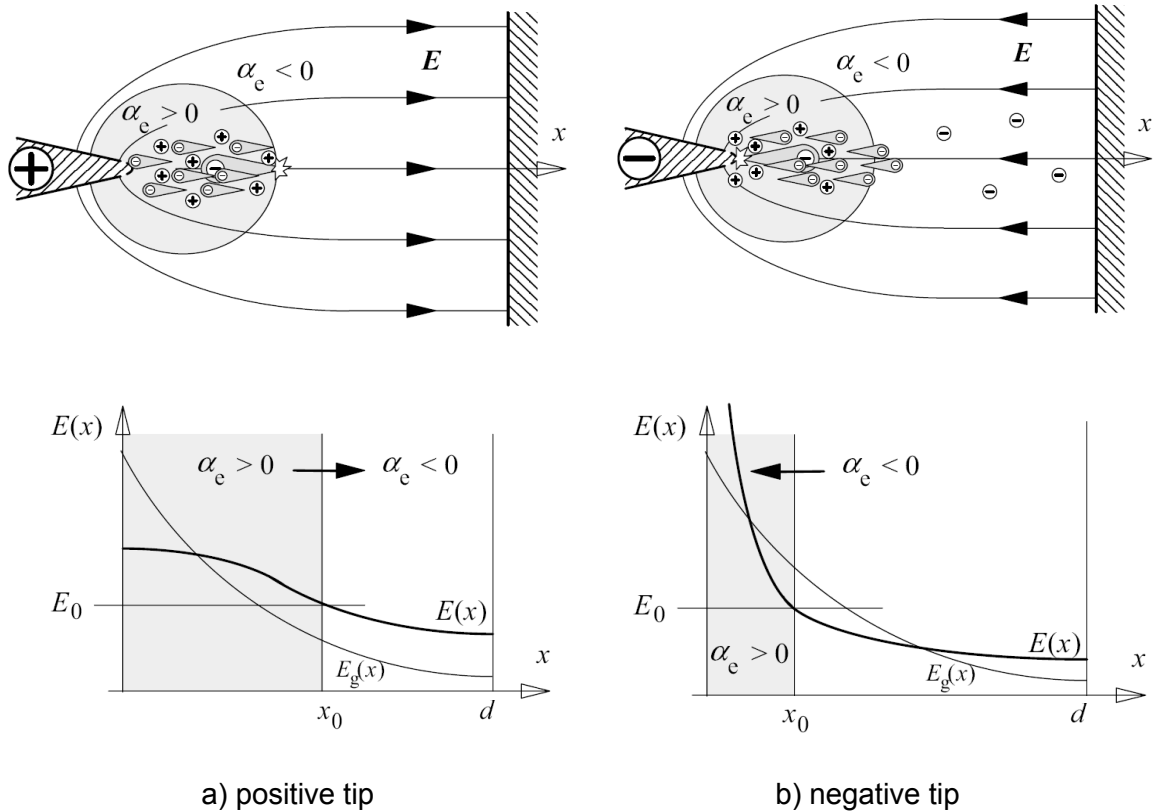


Figure 5.4: Avalanche in inhomogeneous field with a negative tip [Küc2005]

The electrons formed in front of the tip by collision ionization are drawn away by the anode. A positive space charge remains, which reduces the electric field strength at the tip without resulting in a breakdown. When the voltage is increased further, short duration discharges appear in the weakly glowing space charge region and the ionization boundary is displaced.

The frequency and range of the discharges increase with increasing voltage, until finally there is a complete breakdown. In the configuration with a negative tip and positive plate rather different behaviour occurs, **Figure 5.5 b**. A positive space charge results in front of the tip when the inception voltage U_i is exceeded, but now the electrons travel in the direction of the plate electrode. If the gas is not able to form negative ions by attachment of electrons, for direct voltage this immediately results in a breakdown since the positive space charge further increases the field strength in front of the tip; stationary incomplete discharges are not possible. In air a space charge consisting of negative ions is formed which can reduce the electric field strength in front of the tip to such a small value that the collision ionization is stopped and the ionization boundary is displaced to smaller values, $x=x_0$. The discharge sets in again when the negative space charge traveled away. The result is a pulse type of mechanism, which leads to regular current pulses of 10 ns duration of great technical significance, namely as external partial discharges.



up: development of Streamer in the region of high electric field strength and positive effective ionization factor

down: electric field strength distribution along x-axis without space charge ($E_g(x)$) and considering the space charge ($E(x)$) with the displacement of the ionization boundary

Figure 5.5: Polarity effect in strong inhomogeneous field with positive and negative tip [Küc2005]

5.3 Determination of the Ionization Coefficient

In **Chapter 5.2** the discharge mechanism was presented generally. When a water drop is present on the insulating surface the discharge mechanism presents some particularities. Due to the fact that the discharges take place on the insulating surface, without the presence of any metallic electrode the second emission coefficient γ_s is almost zero. During experiments the inception voltage is the only parameter which can be measured. Based on values of the inception voltage, the electric field strength at the water drop edges must be deduced. Water drops deform under the electric field stress and therefore an analytical calculation of the electric field strength is not possible. The electric field strength values at the water drop can be obtained only from electric

field simulations. In order to correlate the results of the electric field simulation with the measured inception voltage, the partial discharge inception requirements must be fulfilled. From the electric field simulation results it is possible to see how the streamer ionization coefficient changes along the insulating surface near drop. According to [Wind1994] and [Gal1991] a comparison of the first ionization coefficient α with the attachment coefficient η in air for the arrangement of the water drop on the insulating surface reveals that up to 2,5 mm, $\alpha > \eta$.

In order to fulfil the condition for Streamer development, the effective ionization factor should be positive ($\alpha_e > 0$). As the attachment coefficient is neglected, the parameter of interest is the ionization coefficient α . It is known that the ionization coefficient is related to the electric field strength and the gas pressure by the similarity law:

$$\alpha / p = f(E / p) \quad (5.28)$$

The ionization coefficient can be measured using different methods, e.g. steady state Townsend [Yos1969], or it can be calculated, knowing the inception voltage or the electric field, respectively. There are several formulations in the literature for the calculation of the ionization coefficient. They are defined differently depending on the E/p interval. Here the region of interest is below $2,5 \frac{\text{kV}}{\text{mm} \cdot \text{bar}}$. An overview of the existing formulations is given in **Table 5.2**.

Windmar used an arrangement which consists of a uniform electric field gap with hydrophobic insulating surface. In the gap a water drop of defined size and resistivity is centrally placed. In order to simulate conductive channels which have been formed by breakdown, a metal wire from both electrodes was introduced into the gap almost in contact with drop.

Korolev used the method of measuring prebreakdown current. For a uniform electric field with electron emissions current from the cathode, i_{em} , impact ionization in the gas, and secondary processes at the cathode, the total current in the external circuit is given by:

$$i = i_{em} \frac{\exp(\alpha d)}{1 - \gamma_s [\exp(\alpha d) - 1]} \quad (5.29)$$

Table 5.2: Ionization coefficient expressions according to different authors

Author	Ionization coefficient	
Windmar [Wind1994]	$\frac{\alpha}{p} = \exp\left(\frac{\frac{E}{p} - 58,2}{4,95}\right)$	$\frac{E}{p} \leq 2,625 \frac{\text{kV}}{\text{mm} \cdot \text{bar}}$
Korolev [Kor1998]	$\frac{\alpha}{p} = A \cdot \exp\left(-\frac{B}{\frac{E}{p}}\right)$	$A = 0,64 \frac{1}{\text{mm} \cdot \text{bar}}$ $B = 19 \frac{\text{kV}}{\text{mm} \cdot \text{bar}}$ $2,7-13,2 \frac{\text{kV}}{\text{mm} \cdot \text{bar}}$
Friedrich [Fri1992]	$\frac{\alpha}{p} = C \cdot \left[\frac{E}{p} - \left(\frac{E}{p} \right)_M \right]^2 - A$	$A = 0,2873 \frac{1}{\text{mm} \cdot \text{bar}}$ $C = 1,6053 \frac{1}{\text{mm} \cdot \text{bar}}$ $\left(\frac{E}{p} \right)_M = 2,165 \frac{\text{kV}}{\text{mm} \cdot \text{bar}}$
Rao & Raju [Rao1971]	$\frac{\alpha}{p} = C_1 \cdot \frac{E}{p} - A_1$	$A_1 = 80,0006 \frac{1}{\text{mm} \cdot \text{bar}}$ $C_1 = 16,7766 \frac{1}{\text{kV}}$
Meek [Mee1978]	$E_r = k \cdot \frac{\alpha \cdot e^{\alpha x}}{\sqrt{\frac{x}{p}}}$	$k = 5,6 \cdot 10^{-5} \text{kV} \cdot \left(\frac{\text{mm}}{\text{bar}} \right)^{0,5}$
Hartmann [Har1984]	$\frac{\alpha}{p} = M \left\{ A \left[1 + \frac{C}{N \left(\frac{E}{p} \right)^3} \right] \cdot e^{-B \cdot p/E} - o \cdot \psi \right\}$	$A = 1,75 \cdot 10^3 \quad B = 4 \cdot 10^4$ $C = 1,15 \cdot 10^{12} \quad M = 1 + 10^{-2} \cdot H$ $N = 1 + 3,2 \cdot 10^{-2} \cdot H$ $O = 1 + 1,15 \cdot 10^{-1} \cdot H^{0,1}$ $\psi = \frac{0,9}{1,49 + e^{-\frac{p}{587}}}$ $p - \text{pressure at } 0^\circ \text{C}$ $H - \text{water content in } \text{g/m}^3$

The coefficient α is determined for the region of electric field where $\gamma_s \approx 0$ from the slope of the straight line corresponding to the dependence $\ln(i/i_{em}) = \alpha d$ obtained experimentally.

Friedrich measured the effective ionization coefficient in synthetic air (80 % N₂: 20 % O₂, both N₂ and O₂ has a purity of 99,99 %) with the time resolved method $2,5 < E/p < 7,9$ kV/mm·bar . Rao and Raju investigated also the effective ionization coefficient and showed that it fits a linear equation for the range $7,934 < E/p < 14$ kV/mm·bar .

The data from the previous two authors can be used for dry air because of the measurement accuracy and the state of art technique that Friedrich used as well as the high values of E/p that Rao and Raju used for their experiments.

Meek derived the expression of ionization coefficient considering a plane parallel gap in air assuming that the positive space charge is concentrated in a spherical volume of radius r , equal to that of the avalanche. The Meek's streamer criterion is valid for uniform field and x represents the gap length.

Based on the empirical formulation for the corona onset gradient field proposed by Peek, Hartmann developed a mathematical physical model to obtain the ionization coefficient whatever the values of the quoted geometrical and physical factors are. The various parameters in the Hartmann's expression have been chosen to match the experimental values for dry air and for air under controlled humidity conditions. This expression covers the whole E/p domain.

The ionization coefficient in the range 0,5 - 3 kV/mm·bar is calculated based on the expressions from **Table 5.2** . For the same electric field strength the calculated values of α are very different from one expression to another, as presented in **Figure 5.6**. The results obtained using Meek's expression are almost constant, while the values obtained using Rao & Raju and Hartmann are negative along the range of interest. The negative values are effective ionization coefficients α_e but as the attachment coefficient $\eta \ll \alpha$ also the ionization coefficient α will be negative. Using Friedrich's expression the ionization coefficient is constant and it is zero along the given range. The values of α from Windmar and Korolev expressions are zero to 2 kV/mm·bar and then increase in the region of 2 – 3 kV/mm·bar.

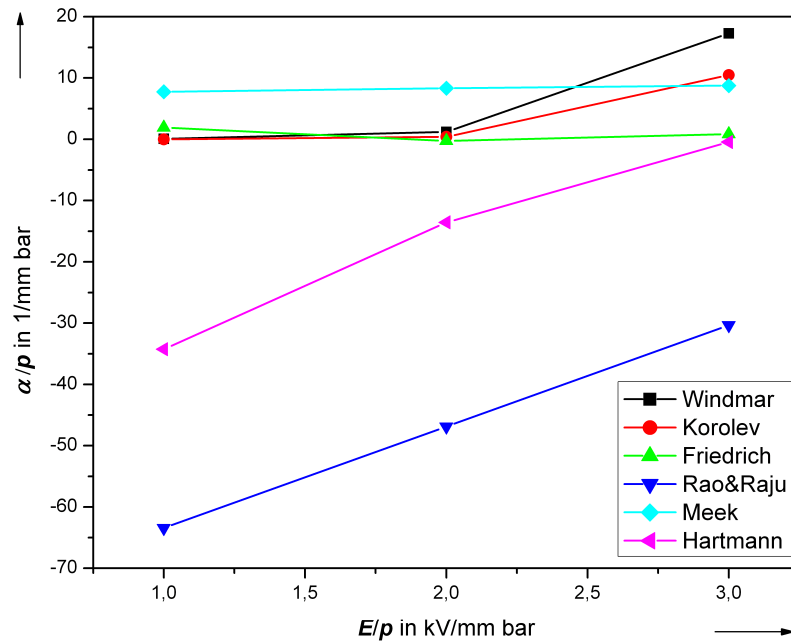


Figure 5.6: Ionization coefficient in air according to different authors

The results show that parameters obtained mathematically or empirically are valid only for the arrangements used to obtain them and are not suitable to calculate the ionization coefficient at water drops on an insulating surface. Therefore, in this work other criteria to correlate the electric field strength obtained from simulations with the measured inception voltage will be developed.

The PD inception voltage at water drops on an insulating surface is affected by several factors. In the following chapter the influence of the ambient conditions and atmospheric negative ions will be presented.

5.4 Inception Voltage Influencing Parameters

5.4.1 Ambient Conditions

Air temperature and humidity are parameters that influence the discharge processes. According to the kinetic gas theory the particle (electrons or ions) density n is a function of the absolute temperature T , pressure p as follows:

$$n = \frac{p}{k \cdot T} \quad (5.30)$$

where k is the Boltzmann constant, $k = 1,37 \cdot 10^{-23} \frac{\text{Ws}}{\text{K}}$. The electron mean free travelling path is then expressed as:

$$\lambda_{m,e} = \frac{k \cdot T}{\pi \cdot r^2 \cdot \rho} \quad (5.31)$$

and the ion mean free path as:

$$\lambda_{m,i} = \frac{k \cdot T}{4\pi \cdot r^2 \cdot \rho} \quad (5.32)$$

The ionization coefficient can be expressed as a function of the free path:

$$\alpha = \frac{1}{\frac{k \cdot T}{\pi \cdot r^2 \cdot \rho}} \cdot e^{-\frac{\lambda_i}{\frac{k \cdot T}{\pi \cdot r^2 \cdot \rho}}} \quad (5.33)$$

thus by increasing the temperature, the ionization coefficient value increases, and by increasing the pressure, the ionization coefficient value decreases. Therefore, a correction of the ionization factor and electric field strength, respectively, must be made with respect to ambient conditions. According to [IEC 60052] a relative density correction factor must be used, see expression (5.46). An explanation can be given also by the effect of the ion mobility increasing at higher temperature and therefore the probability of avalanche formation being higher at high temperature than at low temperature.

So far, only the influence of the air density on the electrical discharge was presented, therefore the influence of the humidity on the discharge mechanism will now be analyzed [Pol1985], [Kik2008].

The humid air density ρ_{ha} is lower than the dry air density and can be expressed as a function of pressure (p_{ha} humid air pressure, p_s saturation pressure), temperature (T), gas constant (dry air gas constant $R_{da} = 287 \frac{J}{kg \cdot K}$, water vapour constant

$R_v = 416 \frac{J}{kg \cdot K}$) and relative humidity φ [Gei1927].

$$\rho_{ha} = \frac{1}{T} \left(\frac{p_{ha}}{R_{da}} - \varphi \cdot p_s \left(\frac{1}{R_{da}} - \frac{1}{R_v} \right) \right) \quad (5.34)$$

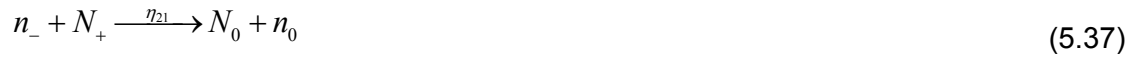
Considering equations (5.33) and (5.34) it can be concluded: by increasing the humidity of the air the density of the air is lower and the ionization coefficient values

increase. The effective ionization coefficient contains also the attachment coefficient of the electrons, which increases with the electronegativity of the air.

But when PD takes place on the insulating surface, in the neighborhood of the triple zone of a water drop, the negative ion density is the key parameter for discharge development. Therefore the following section will give a detailed overview of the dependence of the negative ion density on the atmospheric humidity.

5.4.2 Atmospheric Negative Ion Density

Atmospheric air can be described in terms of six species: neutral molecules (n_0), small (molecular) ions (n_+ , n_-), neutral particles (N_0) and large ions (N_+ , N_-). If q is the rate of small ion creation and $q' = q/n_0^2$, the following reactions take place [All1987]:



where

cosmics – atmospheric air

Σ - combination coefficient (n_- , n_+)

γ - combination coefficient (N_- , N_+)

η_{21} - combination coefficient (n_- , N_+)

η_{20} - combination coefficient (n_- , N_0)

η_{12} - combination coefficient (n_+ , N_-)

η_{10} - combination coefficient (n_+ , N_0)

The rate constants are the ionization and combination coefficients. The reactions involving clustering and hydration of small ions are accounted later by the influence on the combination coefficients.

When a unipolar spherical charge is introduced into nonturbulent air, with no loss of surfaces, the density ν of charged particles decays by self-repulsion [Wat1970] according to

$$\frac{d\nu}{dt} = -\frac{\mu e \nu^2}{E_0} \quad (5.42)$$

where

μ - mobility of any charged particle

e – elementary charge

E_0 – applied electric field

The density of the various species in the vicinity of the electrodes can be computed by solving the following set of equations:

$$\frac{dn_-}{dt} = -\alpha n_- n_+ - \eta_{21} n_- N_+ - \eta_{20} n_- N_0 + q \quad (5.43)$$

$$\frac{dn_+}{dt} = -\alpha n_- n_+ - \eta_{12} n_+ N_- - \eta_{10} n_+ N_0 + q - \frac{\mu_+ e n_+^2}{\epsilon_0} \quad (5.44)$$

$$\frac{dN_-}{dt} = -\eta_{12} n_+ N_- + \eta_{20} n_- N_0 \quad (5.45)$$

$$\frac{dN_+}{dt} = -\eta_{21} n_- N_+ + \eta_{10} n_+ N_0 \quad (5.46)$$

$$\frac{dN_0}{dt} = \eta_{21} n_- N_+ + \eta_{12} n_+ N_- - \eta_{10} n_+ N_0 - \eta_{20} n_- N_0 \quad (5.47)$$

These equations assume that the discharge deposits a positive charge of molecular ions and that this produces the only space charge that needs to be considered, using (5.28).

In the absence of a space charge all derivatives from (5.37)-(5.41) are zero, and this is the equilibrium condition of an unperturbed atmosphere. Starting from this the background densities of all species before discharge occurs is calculated. Eq. (5.37) becomes

$$\alpha n_- n_+ + \eta_{21} n_- N_+ + \eta_{20} n_- N_0 = q \quad (5.48)$$

According to [Cha1967] typical values are: $n_- = n_+ = 10^7$ to 10^9 m^{-3} and $N_- = N_+ = N_0$ where $N_0 = 10^9$ to 10^{11} m^{-3} . Under background conditions, the term $\alpha n_- n_+$ is small and can be neglected and eq. (5.42) becomes

$$\eta_{21} n_- N_+ + \eta_{20} n_- N_0 = q \quad (5.49)$$

For small positive ions, the terms $\alpha n_- n_+$ and $\frac{\mu_+ e n_+^2}{\epsilon_0}$ are small (**Table 5.3**) so that

$$\eta_{12} n_+ N_- + \eta_{10} n_+ N_0 = q \quad (5.50)$$

Since the derivatives are zero (5.39) and (5.40) become

$$\eta_{12} n_+ N_- = \eta_{20} n_- N_0 \quad (5.51)$$

$$\eta_{21} n_- N_+ = \eta_{10} n_+ N_0 \quad (5.52)$$

Using (5.45) and (5.46) results in

$$N_+ N_- = \frac{\eta_{10} \eta_{20}}{\eta_{12} \eta_{21}} N_0^2 \quad (5.53)$$

From (5.47) assuming the symmetrical behaviour of negative and positive ions

$$N_+ = \frac{\eta_{10}}{\eta_{12}} N_0 \quad (5.54)$$

$$N_- = \frac{\eta_{20}}{\eta_{21}} N_0 \quad (5.55)$$

Table 5.3: Values of combination coefficients [All1987]

Coefficients	Unit	at low humidity	at high humidity
α	$\text{m}^3 \text{s}^{-1}$	$2,5 \cdot 10^{-12}$	$1,6 \cdot 10^{-12}$
η_{21}	$\text{m}^3 \text{s}^{-1}$	$10 \cdot 10^{-12}$	$2,5 \cdot 10^{-12}$
η_{12}	$\text{m}^3 \text{s}^{-1}$	$8 \cdot 10^{-12}$	$2 \cdot 10^{-12}$
η_{10}	$\text{m}^3 \text{s}^{-1}$	$5,1 \cdot 10^{-12}$	10^{-12}
η_{20}	$\text{m}^3 \text{s}^{-1}$	$6,4 \cdot 10^{-12}$	$1,3 \cdot 10^{-12}$
γ	$\text{m}^3 \text{s}^{-1}$	$2 \cdot 10^{-15}$	$2,1 \cdot 10^{-15}$
q	$\text{m}^3 \text{s}^{-1}$	10^7	10^7
μ_-	$\text{m}^2 \text{s}^{-1} \text{V}^{-1}$	$2 \cdot 10^{-4}$	$6,7 \cdot 10^{-5}$
μ_+	$\text{m}^2 \text{s}^{-1} \text{V}^{-1}$	$1,6 \cdot 10^{-4}$	$5,3 \cdot 10^{-5}$

From (5.46) and (5.50)

$$\frac{n_+}{n_-} = \frac{\eta_{21}}{\eta_{12}} \quad (5.56)$$

It is known that

$$\frac{n_+}{n_-} = \frac{\mu_-}{\mu_+} \quad (5.57)$$

Using the Langevin theory [Lan1903] the combination coefficients are associated

$$\eta_{21} = \eta_{20} + \frac{e\mu_-}{\epsilon_0} \quad (5.58)$$

$$\eta_{12} = \eta_{10} + \frac{e\mu_+}{\epsilon_0} \quad (5.59)$$

From (5.50) and (5.53) results

$$\frac{n_+}{n_-} = \frac{\eta_{21}}{\eta_{12}} = \frac{\mu_-}{\mu_+} = \frac{\eta_{20}}{\eta_{10}} \quad (5.60)$$

The consequence of the above relation is that $N_- = N_+$ and

$$n_- = \frac{q}{2\eta_{20} N_0} \quad (5.61)$$

$$n_+ = \frac{q}{2\eta_{10} N_0} \quad (5.62)$$

Since q is constant, N_0 is the only independent variable which determines the n_- and n_+ under both equilibrium (background) and nonequilibrium conditions. The background value of the neutral particle density, N_0 depends upon atmospheric pollution as indicated by **Table 5.4**.

Table 5.4: Neutral particle density N_0 [All1987]

Degree of pollution	N_0 in m^{-3}
Large city centre	$5 \cdot 10^{10} < N_0 < 4 \cdot 10^{12}$
Large city limits	$6 \cdot 10^9 < N_0 < 4 \cdot 10^{11}$
Countryside	$10^{10} < N_0 < 3 \cdot 10^{11}$
Sea	$10^{10} < N_0 < 4 \cdot 10^{10}$

The ion balance of the natural atmosphere is determined by the rates of creation of ions by natural processes and loss by combination, either with opposite charge ions to form neutrals or with neutral nuclei to form large ions [All1987].

The detachment of electrons from atmospheric negative molecular ions is known as the principal cause of initiation of positive corona in a divergent electric field [Loe1965], [Ren1974], [Ber1980].

When PD takes place the negative ion density is the significant changing parameter. Starting from a natural background number of negative ions, n_- , it was observed after PD inception that the negative ion density is reduced to values below that of

background [All1987]. Additionally, in moist air under the electric field, the O_2^- ions hydrate with water molecules resulting in large negative ions as follows:



with $n = 0, 1, 2, 3, \dots$ thermo-kinetic constants being known [Bad1972], [Pol1985]. The described process is named clustering and declustering process and it is reversible. The large negative ion density exponentially increases when rising humidity and due to the electric field strength variations at a given humidity, the ion density changes.

The dependence of the breakdown electric field strength on the absolute humidity is: by increasing the absolute humidity the breakdown of electric field strength also increases. According to [IEC 60052] the electric field strength is normalized to standard atmospheric conditions $p_0=1013$ hPa and $T_0=293$ K using the relative density correction factor δ according to:

$$\delta = \frac{p}{1013} \cdot \frac{273+20}{273+g} \quad (5.64)$$

where p is hPa and g in °C.

Then the breakdown voltage U_d is corrected with δ as is presented below:

$$U_d = \delta \cdot U_0 \quad (5.65)$$

But the influence of the absolute humidity on the PD electric field strength is different from that for the breakdown [Fri1992]. This dependence will be analyzed and presented later on in this work.

5.5 Goals of this work

The aim of this work is to analyze the early ageing conditions of an electrically stressed insulating surface. For this the influence of water drops under electric field stress to the partial discharge inception phenomena shall be investigated. Single water drops will be placed on the polymeric surfaces and stressed by alternating and direct voltage. In order to achieve the main goal, several steps shall be followed.

The influence and the importance of relevant parameters like water drop volume, conductivity of the water, surface roughness, and type of electrical stress will be set up. So as to analyze and quantify the influence of relevant parameters, an adequate experimental setup shall be chosen. A visual investigation tool of the water drop on the insulating surface is very important. Attention will also be given to the influence of the measurement systems on the measurement values. The presence of the equipment shall not affect the electric field distribution on the insulating surface. At the same time the measurements shall be repeatable therefore the positioning of water drop, voltage generation and measurement are chosen very carefully.

The influence of the ambient conditions on the discharge activity at the insulating surface shall be also taken into account.

During measurements single water drops will be placed on the surface and their behaviour will be analyzed. Different parameter combinations, which are definitory for water drops behaviour, will be varied and the influence of those parameters will be established. The results from the experiments will be systematized and a water drop behaviour model will be developed. Moreover, the deformations of the water drop, as a result of the electro-hydro-dynamic forces, can have an influence on the local electric field intensifications, **Figure 5.7**.

To expose the interaction between the modification of the electric field on the surface due to the presence of water drop and changing of the electric field distribution upon deformation of water drop, electric field calculations shall be carried out. Important input parameters for modelling and simulations will be the measured values from experiments. Using a field simulation tool, the influence of water drop deformations on the electric field intensification shall be quantified. Knowing exactly the local electric field intensifications at the water drops, the partial discharge inception conditions can be better estimated and preventive measures to avoid material ageing can be taken.

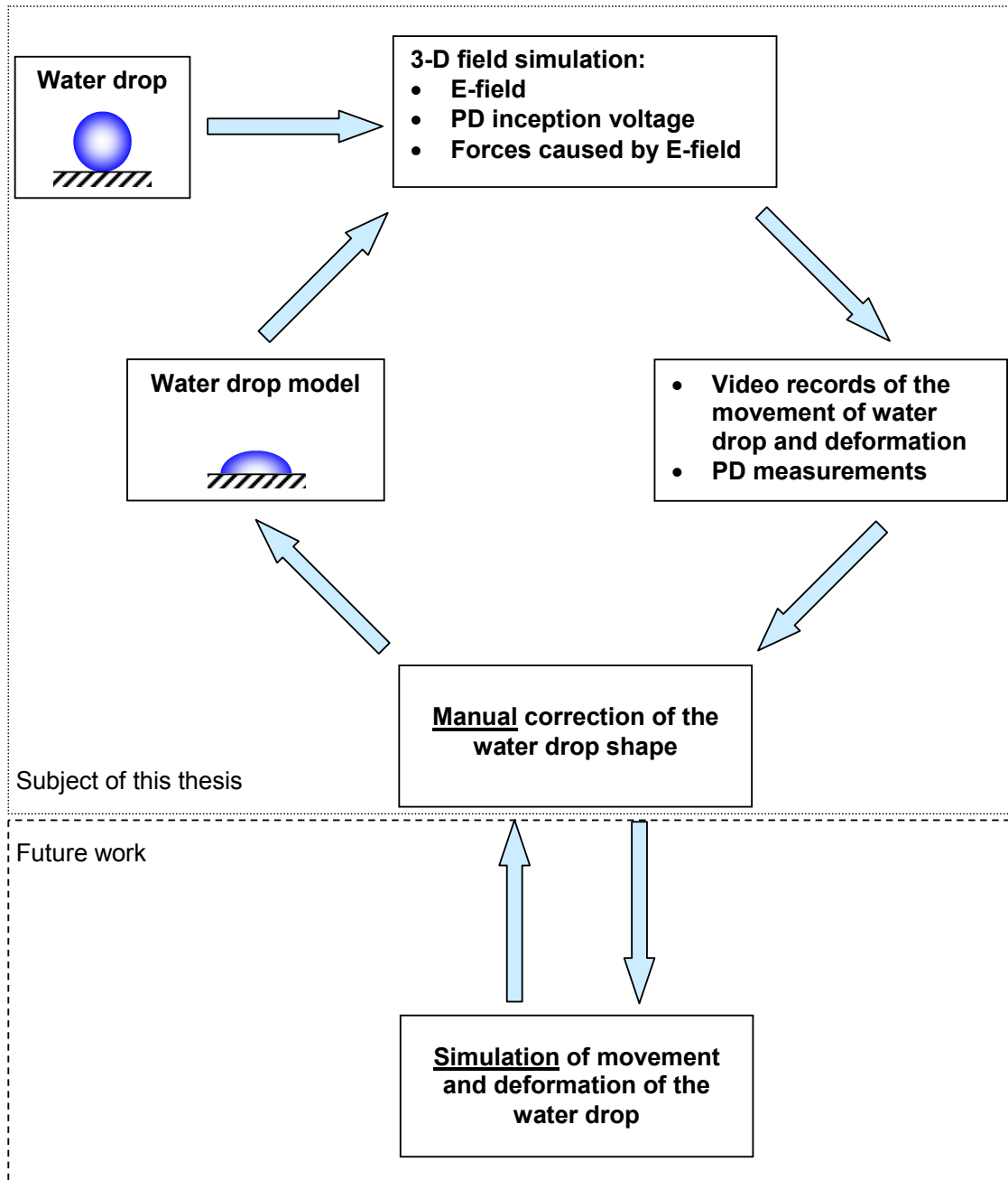


Figure 5.7: Scientific approach

The findings from this work will be evaluated considering the real applications and they will be integrated in the ageing progress of solid polymeric materials. Based on results and conclusions the ageing model can be improved.

6 Experimental Techniques

6.1 Test Setup

6.1.1 Model Insulator

Real insulators exhibit different curvatures and inclination angles. In the following an ideal insulator model will be used. The relevant demand in choosing the model geometry is the electric field on the surface. This should be homogeneous and tangential to the insulating surface when any water droplet is present. In this way the local inhomogeneous electric field will be caused only by the presence of the water drop [Wind1994].

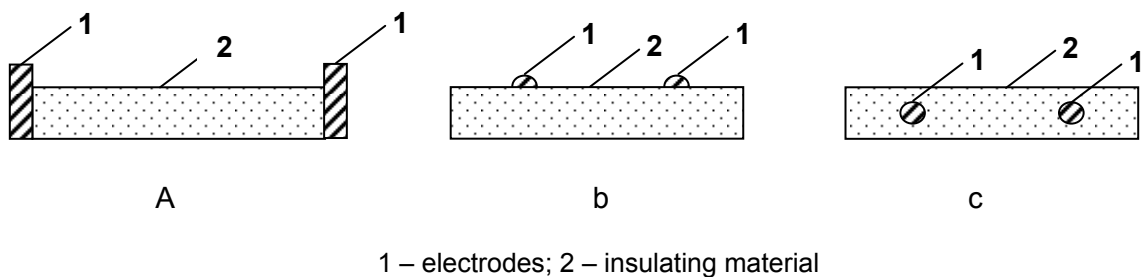


Figure 6.1: Three different geometries for model insulator

a – parallel plate arrangement; b – electrodes on the sample; c – embedded electrodes

In **Figure 6.1** three different possible arrangements are presented. First, a parallel plate capacitor is presented, where the dielectric is silicone rubber. The advantage of this arrangement is that it is a very simple arrangement to obtain a homogeneous electric field between the electrodes. But due to higher distance between the electrodes, a higher applied voltage will be necessary and it is possible to produce flashovers between the electrodes. In the second arrangement the electrodes are placed on the insulating material and are closer to each other. The advantage is that the required voltage in order to obtain the same electric field values is lower but a flashover between the electrodes is still possible. Therefore in the third arrangement the electrodes are embedded in the material. The necessary voltage to obtain the required electric field is lower and the most important advantage is that any discharges will develop between the electrodes. The electric field is concentrated only in the region between the electrodes (the zone of interest) and also the conductive connection

between the water drop placed on the surface and the high voltage electrodes is avoided. The water drop used for experiments is placed on an insulating surface.

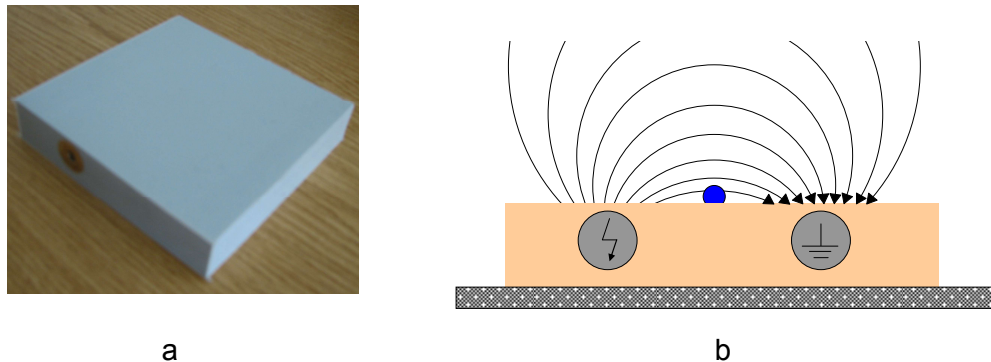


Figure 6.2: Model insulator used for experiment (a) and electric field lines distribution in air (b)

Measurements are made using the sample presented in **Figure 6.2**. It is based on the sample developed in [Keim2003]; only the position of one of the high voltage terminals has been changed in order to avoid flashovers at the terminals. Because of high hydrophobicity of the polymeric materials, silicone rubber was used for the insulator model. During measurements discharges take place on the specimen surface. Due to the recovery property of the silicone rubber, the measurements render reliable results.

Two cylindrical electrodes are embedded in a cubical silicone rubber block of 100 x 100 x 20 mm. Separated by a distance of 20 mm from each other, one electrode is contacted to high voltage, and the other one is grounded, see **Figure 6.4**. In the area where the drop is placed, the force lines of the applied electric field are tangential to the insulating surface.

The material used is Wacker Powersil 600, an elastomer formula, having high tracking and arc resistance, which is used also in the insulator industry. The cross linking process takes place at room temperature (RTV), technical data are presented in **Table 6.1**.

The mixing of the two components is done in a vacuum chamber and the void free casting of the samples is carried out in an open mould by qualified staff at the Institute's casting unit. At the open side of the mould, due to the different surface tension of the material, the surface will not be flat.

Table 6.1: Properties of material (Wacker Powersil 600) used for the model insulator

Material	RTV-Silicone Rubber
Number of components (Ratio 9:1)	2
Viscosity of mixture	15000 mPa s
Cross linking	Room temperature
Density	1,13 g/cm ³
Relative permittivity	2,9
Arc resistance according to [IEC 61621]	> 300 s
Tracking resistance according to [IEC 60587]	Class 1A 3.5

Therefore, the side B from **Figure 6.3** will be the test side (top side) of the model insulator. Before the moulding process starts the inner surface of the mould cast is smoothed. When water drops are placed on this side, the contact angle at the water drops is between 100-120° which denotes a wettability class WC 1.

The electrodes are made from brass, having a radius of 7,5 mm and a length of 99,0 mm. In order to prevent breakdown at the electrodes, the length of the electrodes was chosen shorter than the length of silicone rubber block, and the voltage

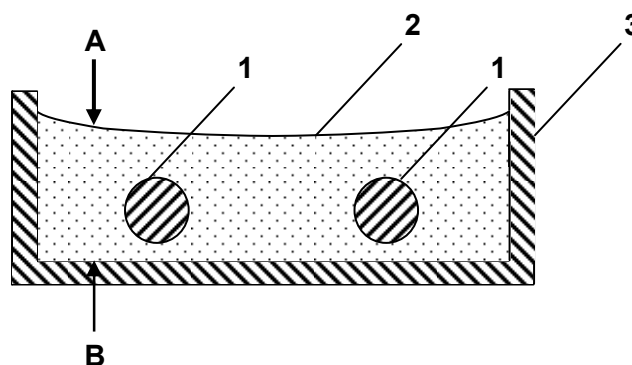


Figure 6.3: Mould cast of the model insulator

1 – electrodes; 2 – Wacker Powersil 600; 3 – casting mould;

A – later bottom side; B – later top side

connections are made at opposite sides, as shown in **Figure 6.4** and **Figure 6.5**. One end of the electrodes is rounded with a radius of 7,5 mm. For the experiments, water drops will be placed on the insulating surface, between the electrodes, as is presented in **Chapter 6.1.4**.

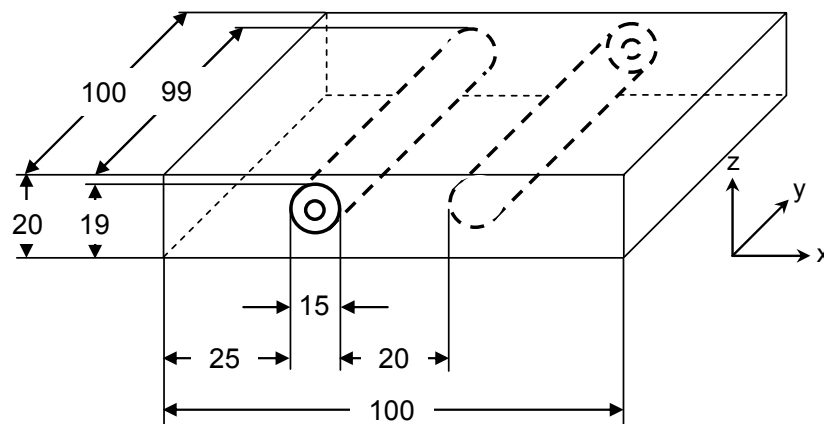


Figure 6.4: Model insulator – three dimensional overview

Before each experiment the tested surface of the sample is cleaned with distilled water to eliminate any dust particles. The sample is placed exactly horizontal using a bubble level. Thus, the possible influence of the surface inclination is excluded.

At the electrodes of the model insulator alternating and direct voltage stress is applied. Using a high voltage transformer, a 50 Hz alternating voltage is used. The voltage increases slowly until the first discharges occur. The measured amplitude of the high voltage varies from 1 - 30 kV depending on the other parameters of the water drop (like volume, conductivity, etc.). For direct voltage stress a Greinacher doubling circuit with a ripple factor of 2,5 % is used. A detailed description of the high voltage circuit is given in **Chapter 6.2**.

6.1.2 Optical Mirror System and High Speed Camera

In order to record the dynamic movement of the water drops in the millisecond range, a digital PCI 2000 SC Redlake high speed camera is used. The system consists of a video camera with a CCD-chip, an optical lens system and a graphic board. The camera software enables image capture and data saving as avi file (video) or bmp files (still pictures) of the colour recordings. The maximum recording rate is 2000 frames/s, and the recording time is 2 seconds. At 2000 frames/s the high speed camera records 4096 frames of a resolution of 240 x 92 pixels, and at 1000 frames/s, 2048 frames with

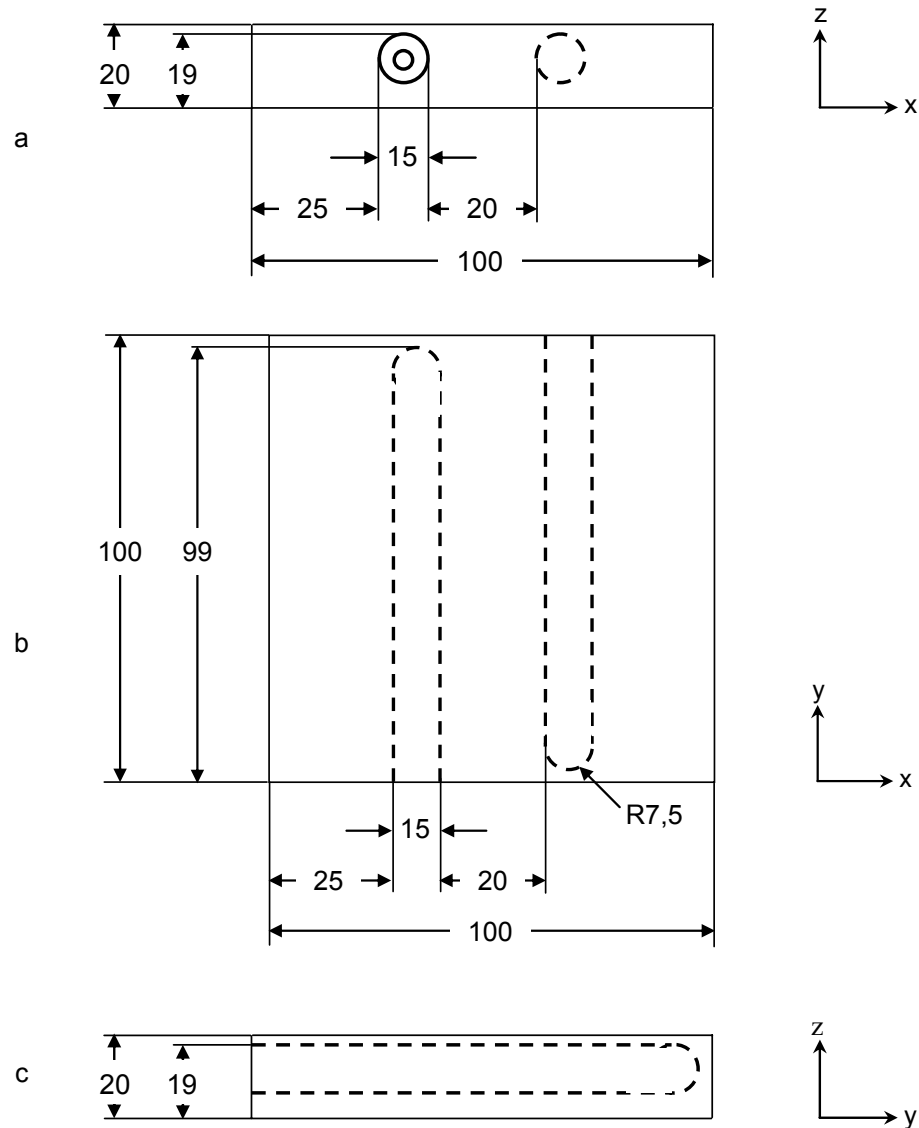


Figure 6.5: Model insulator; front, top and side view

a – front view; b – top view; c – side view

240 x 210 pixels resolution. At the higher recording rate the height of the frames is reduced. The maximum resolution, 480 x 420 pixels is possible when the recording rate is 50 frames/s. For this recording rate the recording time is 10,2 s. The dimensions of one pixel are $4,7 \mu\text{m} \times 4,7 \mu\text{m}$. Upon a recording zoom-in, the horizontal – vertical resolution remains 1:1 which guarantees that the pictures are not distorted.

The camera has an electronic gate which can take values from 1/60 s to 1/1200 s. In order to provide enough light intensity at high shutter speeds the test setup needs high illumination. According to the technical data of the camera for a 1000 frames/s recording rate an illumination intensity of 17,2 Lux is necessary. For a 2000 frames/s

recording rate the double illumination intensity is required. In the case of the recordings taken for this work two xenon lamps of 150 W and 40 W were used which were installed in such a distance that their generated heat has no influence on the test parameters.

Due to the high recording rate in relative short time the high speed camera system has also a cache memory module on the graphic card. When the recording starts the information from the CCD-Chip is digitized in real time and saved on the cache memory module. The information is saved as long as storage capacity on the module is available, which is a ring buffer module. When the buffer is full, the first saved data will be deleted and the new data saved (FIFO principle). This ring buffer technology is used for the trigger function of the camera system. In this way, with the pre trigger function it is possible to record the last 2 seconds before the trigger signal. In addition, it is possible to record after the trigger signal. For the recordings made in this work the pre trigger as well as post trigger functions were used.

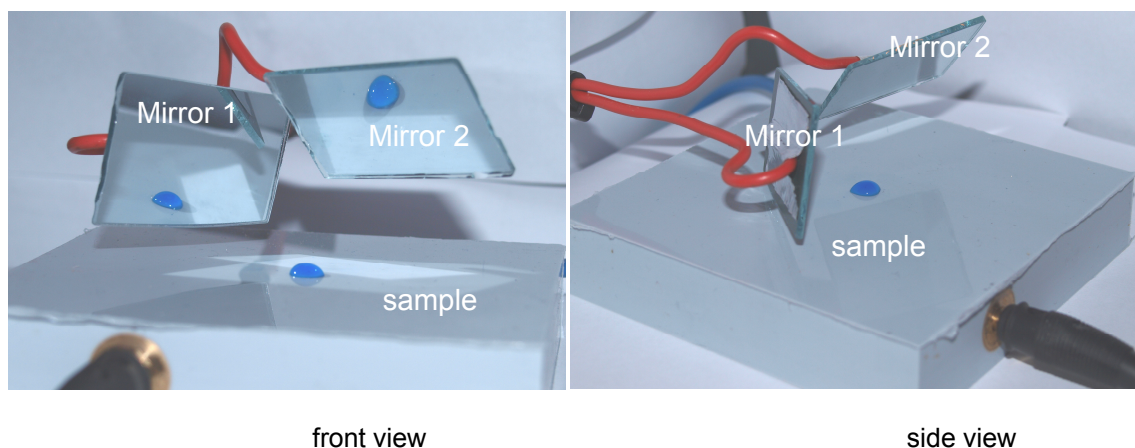


Figure 6.6: Optical system used with the high speed camera

The video recording can be started by the software interface or by an external trigger signal of maximum 5 V. The external trigger method was used in order to correlate the start of the recording with the inception of the partial discharge activity. The trigger signal is a TTL signal generated by a transient recorder and transmitted to the graphic card of the camera. In this way the high speed camera recordings are synchronised with the voltage applied to the tested specimen.

After the video recording has been finished, the data can be saved from the ring buffer to the hard disk. Using the MiDAS Player software, the video recordings are replayed with various setting options such as: play rate, start point, sequences or video play.

The data can be saved as separate sequences at different times and as a video as well. For the water drop behaviour, single sequences are used and are presented in this thesis.

An optical mirror system was introduced to allow the recording of three different views of the water drop movement at the same instant. In **Figure 6.6** the optical system and the sample are presented. The sample is placed in front of the camera so that the front view of the water drop is visible. Mirror 1 is used to catch the side view of the drop and it is placed on the side of the drop at an angle of 60° . Mirror 2 is placed on the top of the sample having an inclination angle of 45° . This mirror allows the recording on the same frame and at the same time of the water drop's top view. In order to focus all views, the mirrors are placed so that the optical paths from the camera to the water drop views have all approximately the same length (at least such that all three views can be focused). In **Figure 6.7** the coordinate system with the three view planes is shown. The x-y plane represents the front view of the water drop; the x-z plane is the top view whereas the y-z plane is the side view of the drop. The main electric field is oriented in x-direction.

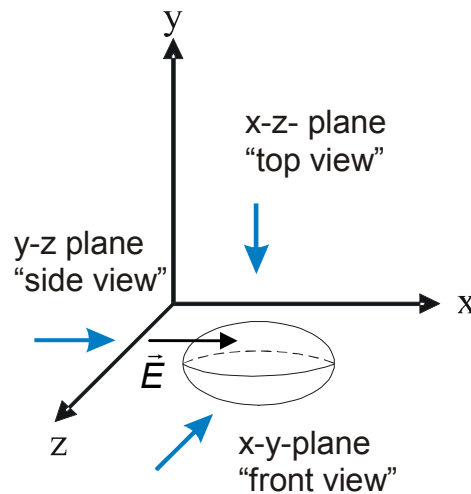


Figure 6.7: Three views of the water drop in the coordinate system

The recordings made with the high speed camera and with the help of the optical system are presented in **Chapter 7.1** and give three dimensional information about the behaviour of the water drop on the insulating surface. Using this system it is possible to record three dimensional frames using only one high speed camera instead of three high speed cameras. The high speed camera system and the mirror system are clamped on a mechanical holder together with the model insulator. In this way mechanical vibration of the system and disturbances of the recording system are avoided.

6.1.3 Calculation of the Applied Electric Field

In this chapter the electric field distribution along the model insulator presented in **Chapter 6.1.1** is analyzed. First an analytical calculation of the electric field strength is made and then compared with field simulation. The presence of the mirror system near the sample surface can disturb the electric field. As the arrangement with mirror system cannot be analytically calculated, the field simulations are used. The electric field distribution with the mirror system is then compared with the electric field distribution without optical system.

The electrodes are embedded in silicone rubber which is surrounded by air. The electric field is spread in the silicone block and in the air. At the interface between two dielectric materials electric field lines and equipotential lines are refracted. The amount of charge accumulated on the insulating surface at a certain voltage value is unknown. The electric field distribution along the surface has to be calculated in two steps. Firstly only the two cylindrical electrodes surrounded by air are considered, then the silicone block is introduced.

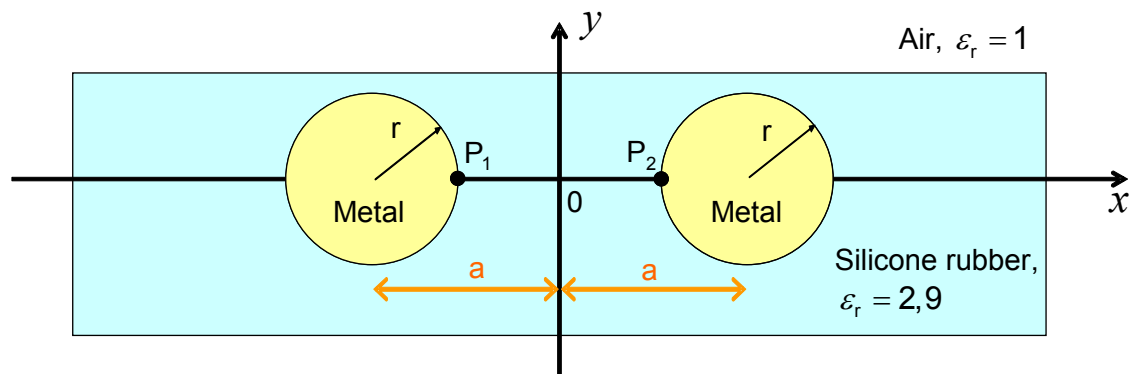


Figure 6.8: Schematic representation of the arrangement in the coordinates system

Considering only two cylindrical electrodes, the electric field distribution is calculated using the superposition principle [Kor2006]. The considered arrangement and coordinate system are presented in **Figure 6.8**. Using equation (6.1) and (6.2), the electric field in x-direction and y-direction, respectively is calculated.

$$E_x = \frac{Q}{2\pi \cdot \varepsilon \cdot l} \cdot \left(\frac{x+a}{(x+a)^2 + y^2} - \frac{x-a}{(x-a)^2 + y^2} \right) \quad (6.1)$$

$$E_y = \frac{Q}{2\pi \cdot \varepsilon \cdot l} \cdot \left(\frac{y}{(x+a)^2 + y^2} - \frac{y}{(x-a)^2 + y^2} \right) \quad (6.2)$$

Due to the fact that the charge is not known, only the direction of the electric field as a function of coordinates can be determined. In order to obtain the charge value, the capacitance of the arrangement must be calculated. The capacitance of an arrangement consisting of two electrodes in a homogeneous dielectric (air) can easily be calculated. But when the electrodes are embedded in silicone rubber, there are two dielectrics (silicone rubber, air) and another method must be used in order to calculate the capacitance of the arrangement.

The electric field distribution of the arrangement is known. At the material boundary the law of refraction is used to obtain the electric field pattern (configuration) for the neighbouring material. The equipotential lines are perpendicular to the electric field lines. If the electric field is represented by field lines and equipotential lines, a mesh of rectangles is built. The sides of the mesh cells are field lines and equipotential lines. Each cell can be considered as a parallel-plate capacitor. The distance between the plates is the distance between two equipotential lines and the width of the capacitor is the distance between two electric field lines. Depending on the position the dielectric between the plates is air or silicone rubber. By connecting these small capacitors in series or in parallel the total capacitance of the arrangement can be calculated and finally the charge of arrangement.

As the area of interest is the silicone rubber surface, where the water drop is placed, the electric field distribution along the surface is calculated. By using equations (6.1) and (6.2) for $y = 0,85$ (the electrodes are not symmetrically embedded) the electric field along a homogeneous dielectric can be calculated. The new equations depend only on x values.

Given that the electric field is spread in air and in silicone rubber the calculation of electric field using equations (6.1) and (6.2) is not possible. In order to use the previous equations the arrangement must be modelled. Therefore, the reflection method is used. After this method is applied the whole area is considered as one homogeneous dielectric. The cylindrical electrodes are considered as line charges. The silicone rubber block has four interfaces at which the electrodes must be reflected. By neglecting the boundary effect, two side interfaces which are perpendicular to the electrodes will not be considered. Firstly, the electrodes are reflected at the upper interface. The new value of the reflected charge is calculated using equation (6.3). This reflected charge must be reflected at the bottom interface, where the new reflected value is smaller. The new charge value is reflected to the upper interface. This

procedure is endless. Upon each reflection the amount decreases according to equation (6.4).

$$Q' = \frac{\epsilon_1 - \epsilon_2}{\epsilon_1 + \epsilon_2} \cdot Q \tag{6.3}$$

$$Q^{(n)} = \left(\frac{\epsilon_1 - \epsilon_2}{\epsilon_1 + \epsilon_2} \right)^n \cdot Q = (-0,371)^n \cdot Q \tag{6.4}$$

After a certain number of reflections, when the amount of the reflected charge can be neglected, the reflection method can be interrupted. In this work the reflection method is applied twelve times for the upper and twelve times for the bottom interface. Left and right sides of the silicone block are also reflected by themselves, upper and bottom interfaces, respectively. **Figure 6.9** presents a schematic representation of the reflection method for the considered arrangement.

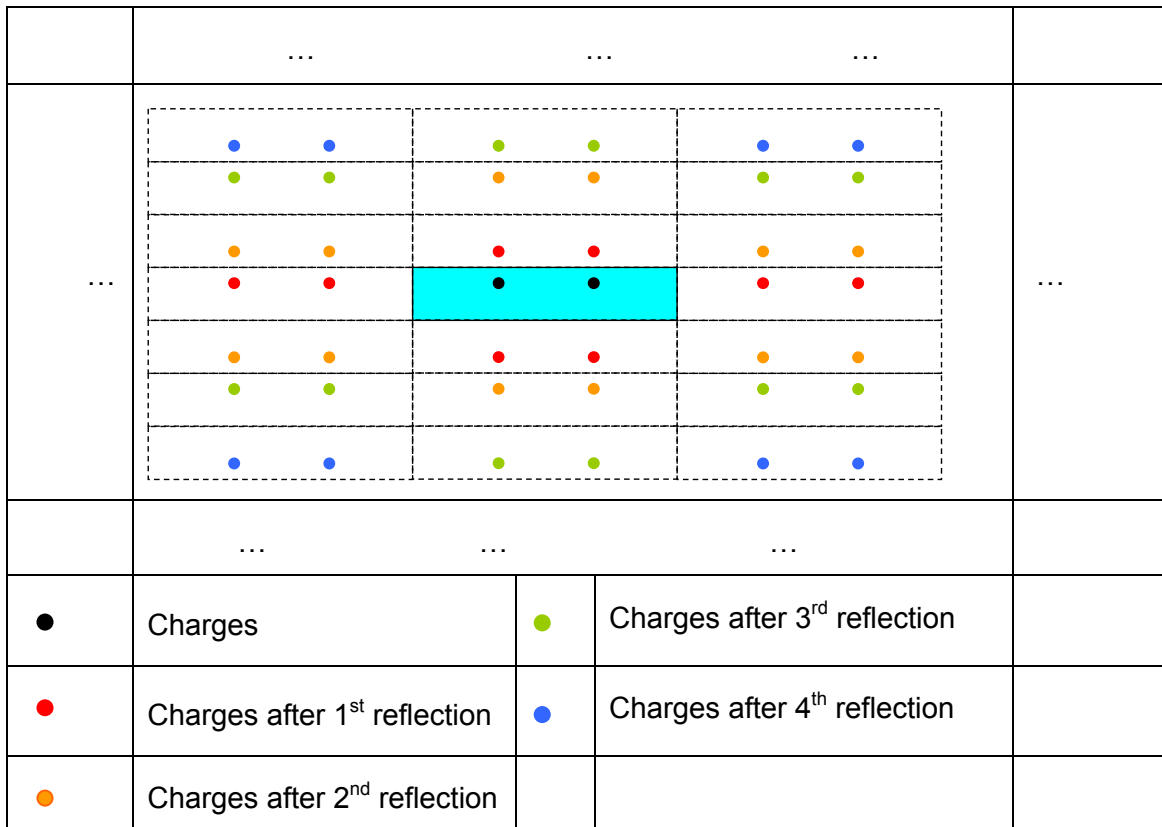


Figure 6.9: Schematical diagram of the charge reflection method

After the charge reflection method has been applied, the electric field distribution in the dielectric “silicone rubber” is calculated using equations (6.1) and (6.2) where ϵ_r is the relative permittivity of silicone rubber. The tangential components of the electric field in air and in silicone rubber are presented in **Figure 6.11** and the normal component in

Figure 6.12. Due to the steady property of the tangential component, the tangential component of the electric field in air is the same as the tangential component in silicone rubber. The normal component of the electric field in air is calculated using the reflection law at the boundary of two dielectrics, **Figure 6.10**, equation (6.5)

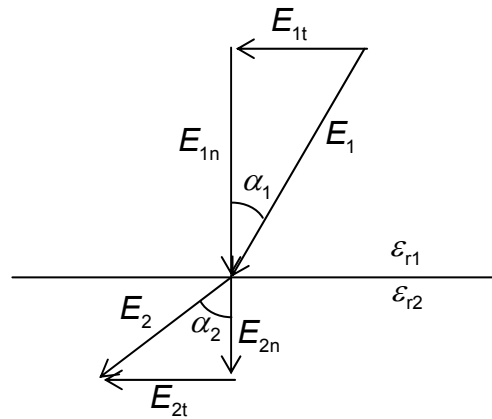


Figure 6.10: Reflexion law at the boundary of two dielectrics

$$\frac{\tan \alpha_1}{\tan \alpha_2} = \frac{\epsilon_{r1}}{\epsilon_{r2}} \quad (6.5)$$

The absolute amount of the electric field can then be calculated using (6.6).

$$E_{\text{abs}} = \sqrt{E_x^2 + E_y^2} \quad (6.6)$$

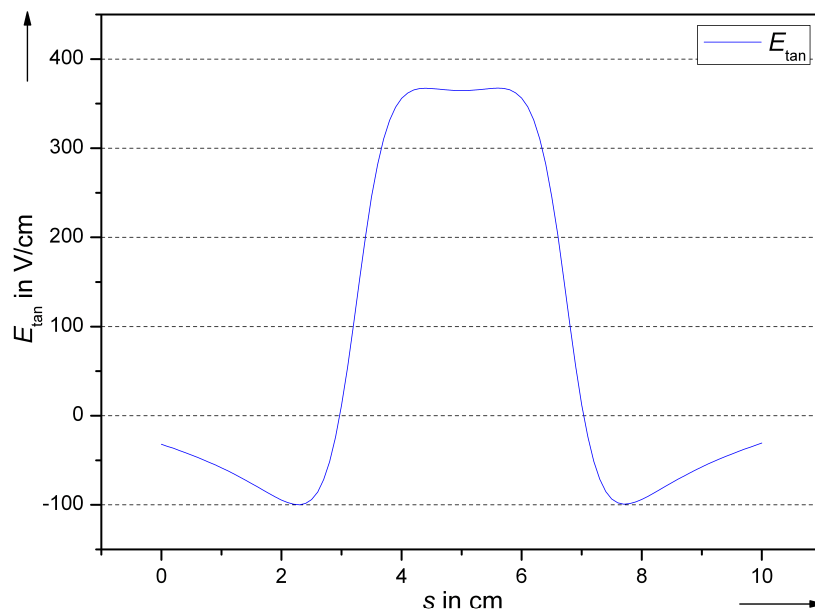


Figure 6.11: Tangential component of the electric field on the insulating surface

Figure 6.11 – Figure 6.13 present the tangential, normal and absolute components of the electric field distribution along the sample surface. The normal and absolute components are presented as well in air as in sample material (silicone rubber). The values on the y-axis correspond to a voltage of 1 kV between the electrodes.

The electric field distribution on the insulating material is simulated using CST EM Studio software [EMS2009]. The electrostatic solver is used. The discretization of the

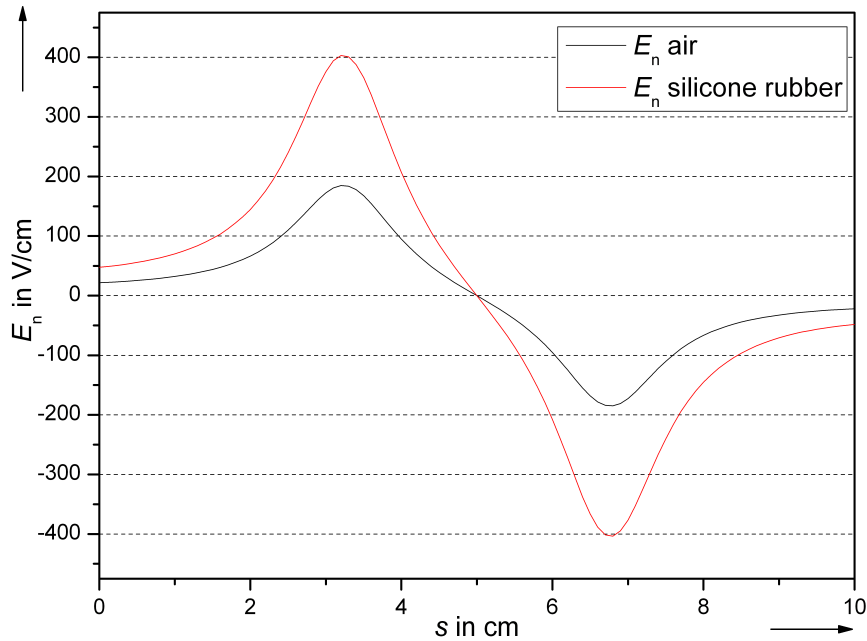


Figure 6.12: Normal component of the electric field on the insulating surface

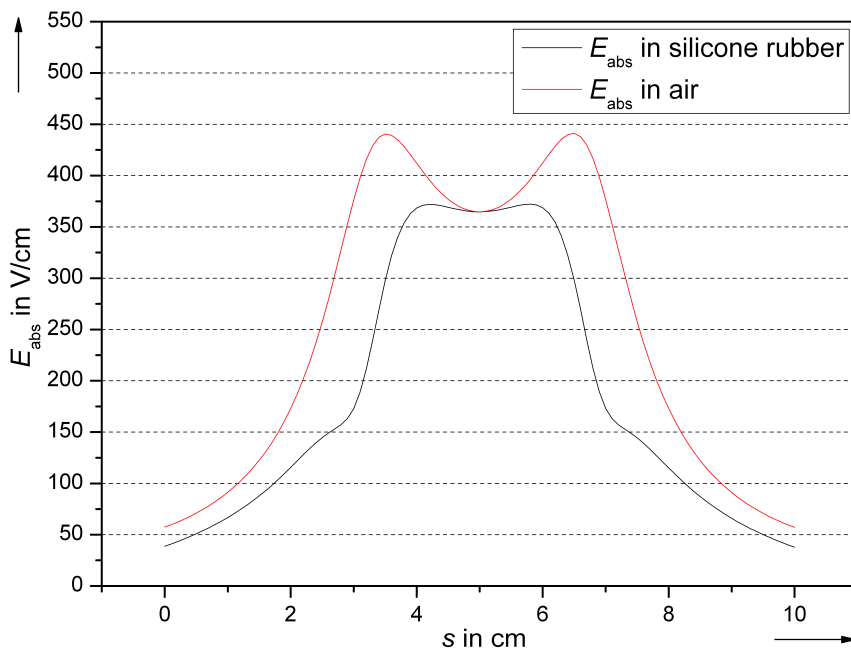


Figure 6.13: Absolute values of the electric field on the insulating surface

model can be made using two different mesh types. The model is divided into small hexahedral or tetrahedral cells, see **Figure 6.14**. A tetrahedron is a polyhedron composed of four triangular faces, three of which meet at each vertex. The tetrahedral mesh reproduces the contour of the shapes better than the hexahedral mesh. Therefore all the simulations in this work are done using tetrahedrons.

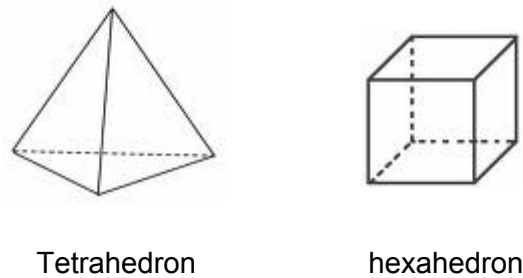


Figure 6.14: Discretization units

The electric field simulations are performed taking into account the voltage, geometry and material parameters used for the analytical calculation. Firstly, from the simulation of the model insulator the electric field distribution is analyzed and compared with the analytical calculation. The comparison between the calculated and simulated tangential component of the electric field strength is presented in **Figure 6.15**.

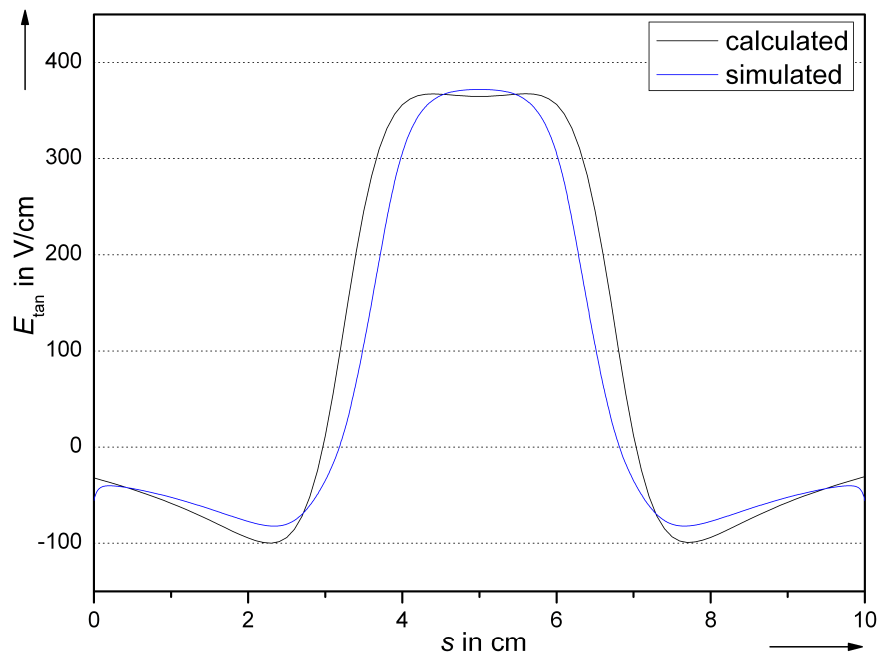


Figure 6.15: Comparison of the calculated and simulated tangential component of the electric field in air

In **Figure 6.16** the absolute component of the electric field strength once calculated and once simulated is presented.

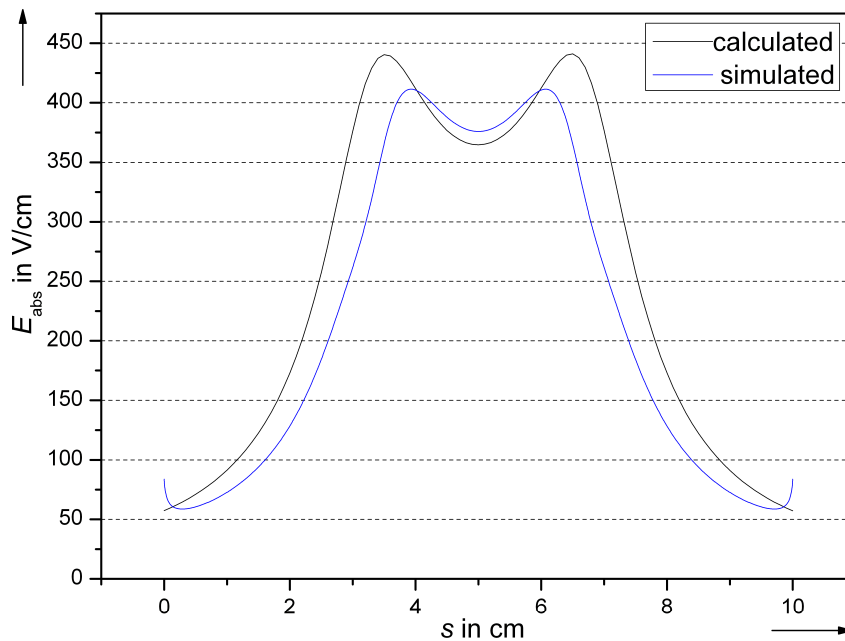


Figure 6.16: Comparison of the calculated and simulated absolute component of the electric field in air

The results show that the calculated and the simulated electric field values are sufficiently similar. The differences between the curves shown in **Figure 6.15** and **Figure 6.16** are caused by the different discretization steps. In the case of the calculated curve, the number of steps is smaller than the number of steps used by the electrostatic solver. The electric field lines in the silicone rubber and in air are presented as arrows in **Figure 6.17**. The area between the electrodes is zoomed below. The electric field lines in air upon the model insulator are parallel to the surface, i.e. the electric field is homogeneous.

During measurements the mirror system is present near the model insulator, as shown in **Chapter 6.1.2**. The presence of the conductive layer from the optical system can cause local distortion of the applied electric field. Due to the geometry of the arrangement, an analytical calculation is no longer possible. Therefore, the electrostatic solver is used. Firstly, the arrangement is modelled and then simulation parameters are set as in the previous arrangement. Only the area between the electrodes, where the electric field lines are parallel to the sample, is analyzed. Thus, in the following diagrams only the area between the electrodes $s = (4..6)$ cm is plotted. In **Figure 6.18** the distribution of the tangential electric field with and without the mirror system is

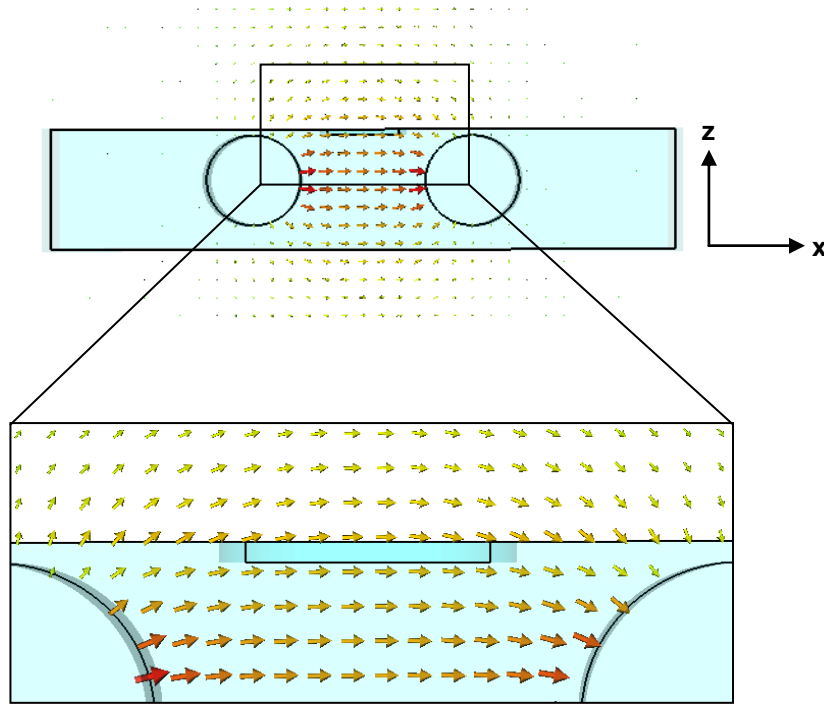


Figure 6.17: Electric field distribution in region between the electrodes

presented. Firstly, it is observed that the electric field is approximately homogeneous in the region between the electrodes, where later on the water drop will be placed and secondly the influence of the mirror system is negligible. The difference between the arrangement with mirror system and without mirror system is 2 % of the applied electric field. The difference is constant along the considered path.

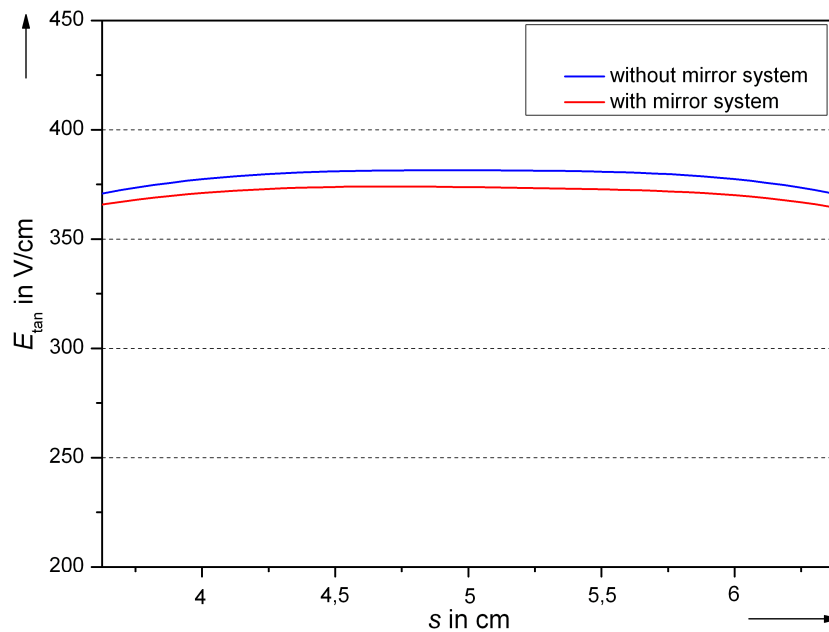


Figure 6.18: Distribution of the tangential electric field strength in the region between electrodes, with and without mirror system

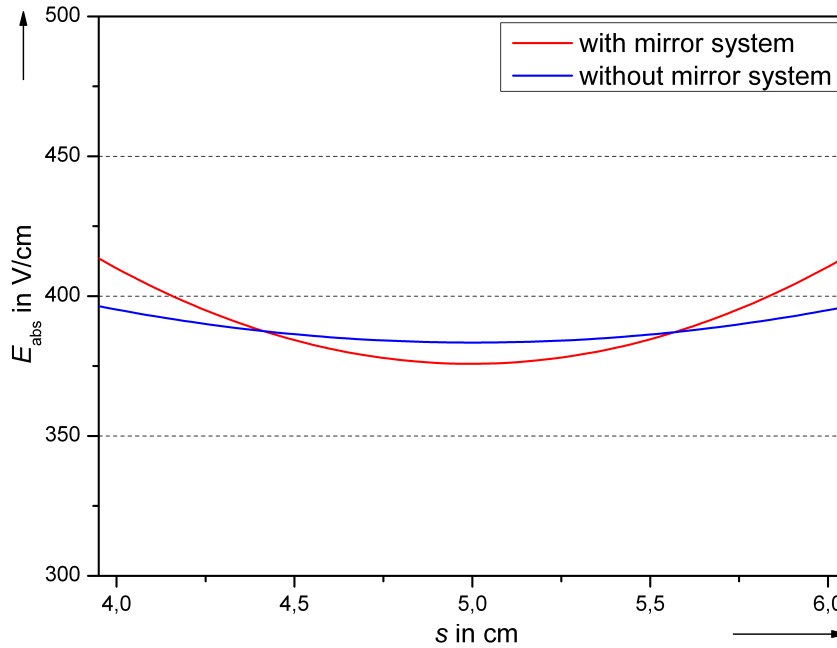


Figure 6.19: Distribution of the absolute electric field strength in the region between electrodes, with and without mirror system

The absolute values of the electric field with and without the mirror system are plotted in **Figure 6.19**. Here the difference is 3 % of the applied electric field. The higher difference of the absolute values can be caused by the normal component of the electric field which is more affected by the presence of the mirror system. As the tangential component is the parameter of interest and the difference is only 2 %, it can be concluded that the influence of the mirror system on the values of the electric field can be neglected. The most important deduction is that the mirror system is not affecting the homogeneity of the electric field in the area of interest. The electric field values, calculated in this chapter are used later in **Chapter 8.2.2** to obtain the validation criterion of the simulation results.

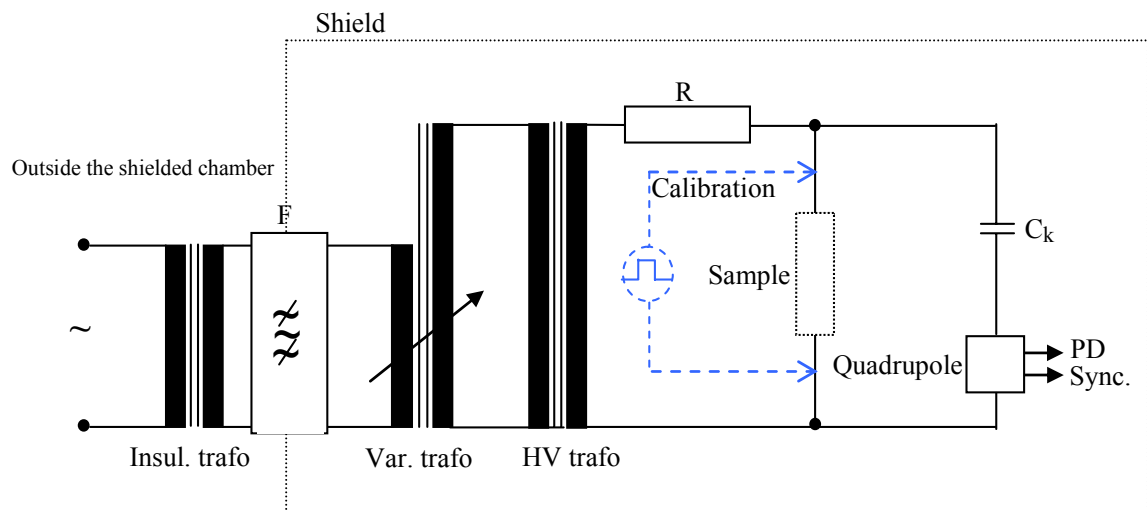
6.1.4 Water Drops

In order to analyze the behaviour of the water drops on an insulating surface, different parameters of the water drops were varied during the experiments. Water drops are placed on the model insulator presented in **Figure 6.2**, in the area between the electrodes using a microliter pipette with a volume range from 1 μl to 100 μl and an accuracy of $\pm 0,1 \mu\text{l}$. The drops are placed on the surface holding the pipette perpendicular to the insulating surface. In this way the water drop is symmetrical and round. By changing the inclination angle of the pipette, the water drop will be elongated and the start shape will no longer be spherical. This will influence the deformation

shape of the water drop under electric field stress. For the experiments double-distilled water is used and the volume of the water drops varies from 10 μl to 100 μl . Due to the rapid evaporation, drops smaller than 10 μl are not used. During experiments the conductivity of the water is varied from $5 \cdot 10^{-6}$ S/cm to $500 \cdot 10^{-6}$ S/cm. As the model insulator is grey and the water drop is transparent, the changing of the water shape is difficult to identify. Therefore, Methylene Blue ($\text{C}_{14}\text{H}_{18}\text{ClN}_3\text{S}$) is used to colour the water drop blue. Thus, the contrast is higher and the light reflexions from the lamps are minimized. The influence of the colorant on the conductivity of water drop depends on the concentration of the colorant in water which is measured before each experiment.

6.2 High Voltage Equipment and PD Measurement System

The measurements were carried out in the PD measurement chambers of the High-Voltage Institute. The high-voltage circuit presented in **Figure 6.20** consists of an



Insul. Trafo	Insulation transformer	$U_2=550$ V; 60 kVA
Var. trafo	Variable ratio transformer	400/0-550 V; 32 kVA
HV trafo	High voltage testing transformer	MWB TEO 100 0,38/100 kV;10 kVA
R	Damping resistor	2 k Ω
C_k	Coupling capacitor	1000 pF

Figure 6.20: High-voltage circuit

insulating transformer which is located outside the chamber, the variable ratio transformer, the high voltage transformer, the damping resistor R and the test sample. The partial discharge measurement system is connected in parallel to the sample.

The partial discharge measurement is made according to [IEC 60270] using a system of "Power Diagnostics". The system consists of a coupling capacitor C_k of 1000 pF which includes a voltage divider and a quadrupole that couples the high frequency PD signals to the acquisition unit. The partial discharge values are given as charge values usually in pC range. As the chamber is shielded, all input connections are filtered and the background noise is 1 pC. All measurements presented in this work were carried out in the shielded chamber. The setup is calibrated with the help of a 50 pC reference signal applied to the terminals of the test specimen. This is electrical and classical PD measurement principle and in this work is named phase resolved partial discharge measurement system (PRPD measurement). Beside this measurement system, other PD measurement systems also exist. In **Chapter 6.3** another PD measurement system is presented and in **Figure 7.1** a comparison between both systems is given.

6.3 Photomultiplier System

The partial discharges occurring at individual water drops on an insulating surface usually has values below 1 pC. Therefore, a more sensitive measuring device is required in order to sensitively detect inception of the very first streamers, constituting an important requirement for the purpose of this work. A photomultiplier system (PMT for **photo-multiplier-tube**) has proved to be an appropriate measurement system. The difference between the two systems is that the PRPD measurement system is the classical electrical system for PD measurements whereas the PMT system records light intensity in the ultraviolet spectrum. The PMT system consists of a Hamamatsu H8249-012 photomultiplier module, a +/- 15 V voltage source and an oscilloscope. Optical radiation emitted by the discharge at the water droplet is captured by the photomultiplier module which is fed by the voltage source, and the output signal is connected to an oscilloscope, see **Figure 6.21**.

The PMT module has a rise time in the range of only few nanoseconds, which is sufficient for this purpose because the rise time of the partial discharge optical radiation is in the range of 10 nanoseconds [Tat2008]. The window of spectral sensitivity of the PMT module itself is between wavelengths of 200 and 700 nm, see **Figure 6.22**, but additionally a short pass filter is used.

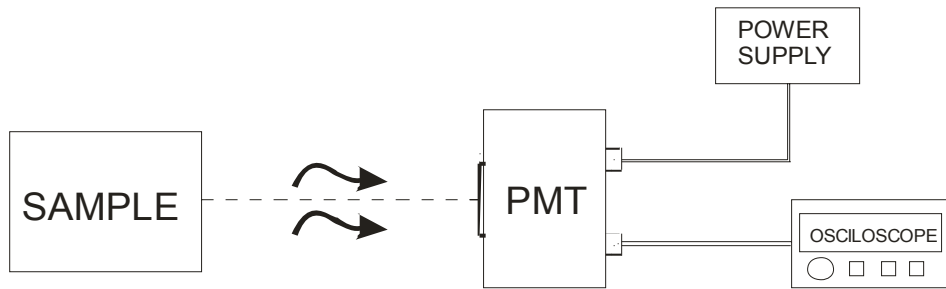


Figure 6.21: Photomultiplier module

The resulting spectral sensitivity of the whole setup is between 200 and 480 nm.

The photomultiplier module is very sensitive to any stray light. For this reason it is encapsulated in a dark, hermetically closed box, see **Figure 6.24**. The capture window of the photomultiplier is focused by a tube to the specimen surface. But this measure is not sufficient to shield against any external light source. Therefore, another hermetically closed box is introduced in which the PMT module and the test specimen are encapsulated, see **Figure 6.23**.

By using two boxes the problem of external light sources has been solved, but due to the fact that the boxes are nearly perfectly closed, the ozone produced by the electrical discharges is accumulated inside the box. Ozone molecules absorb (97-99) % ultraviolet light at wavelengths between 150 and 300 nm.

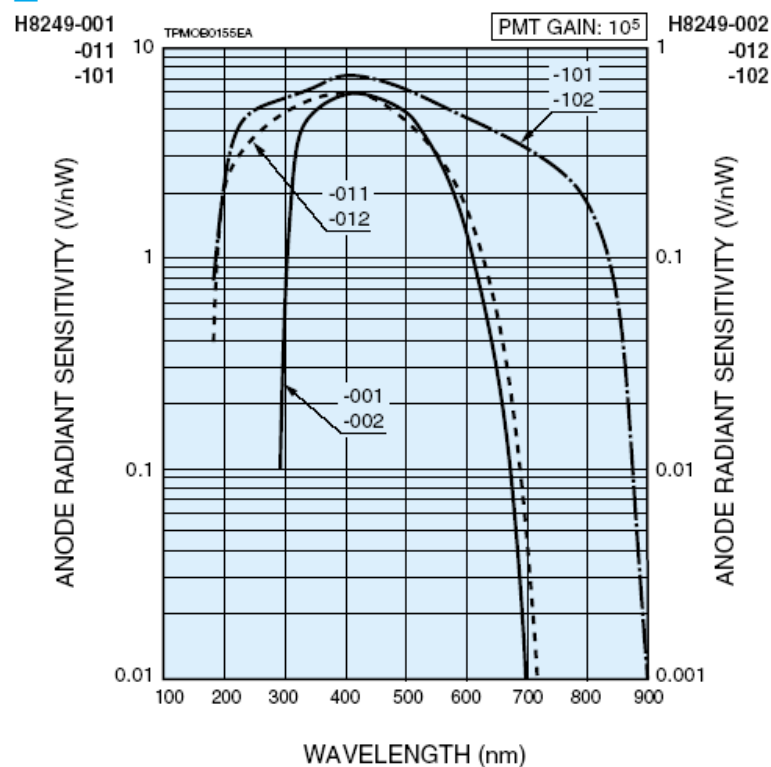


Figure 6.22: Characteristic of the photomultiplier module H8249-012 [Ham2007]

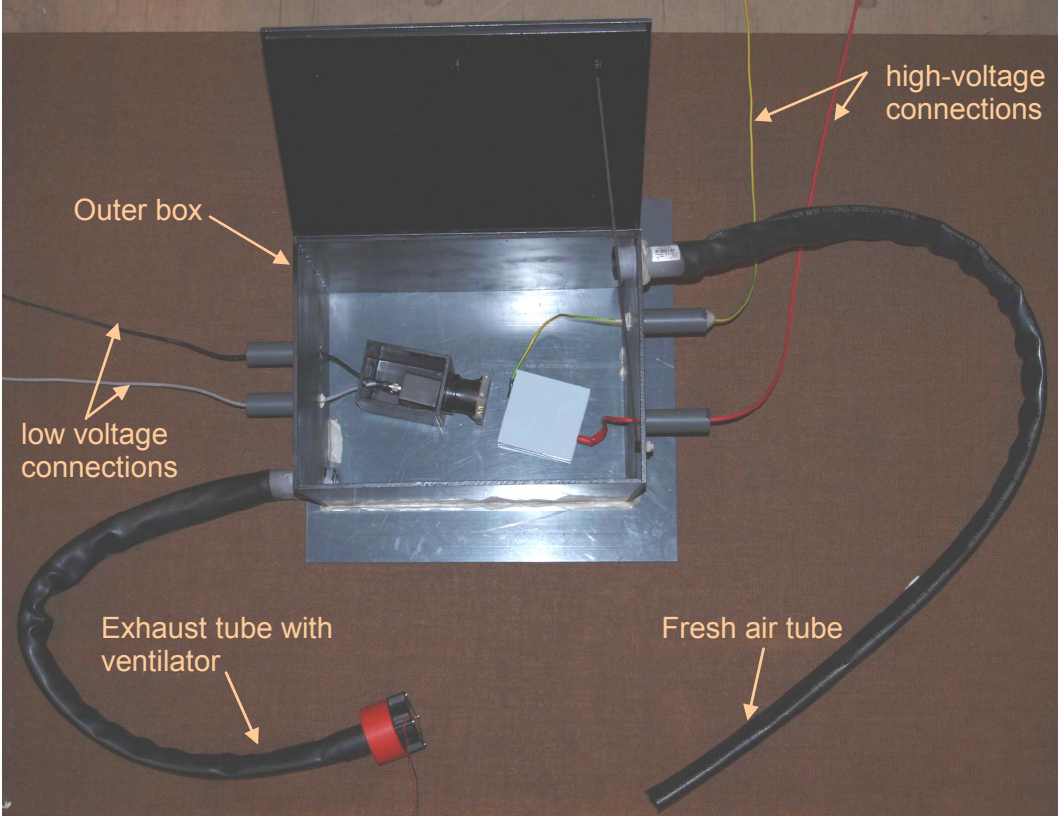


Figure 6.23: PMT measurement system

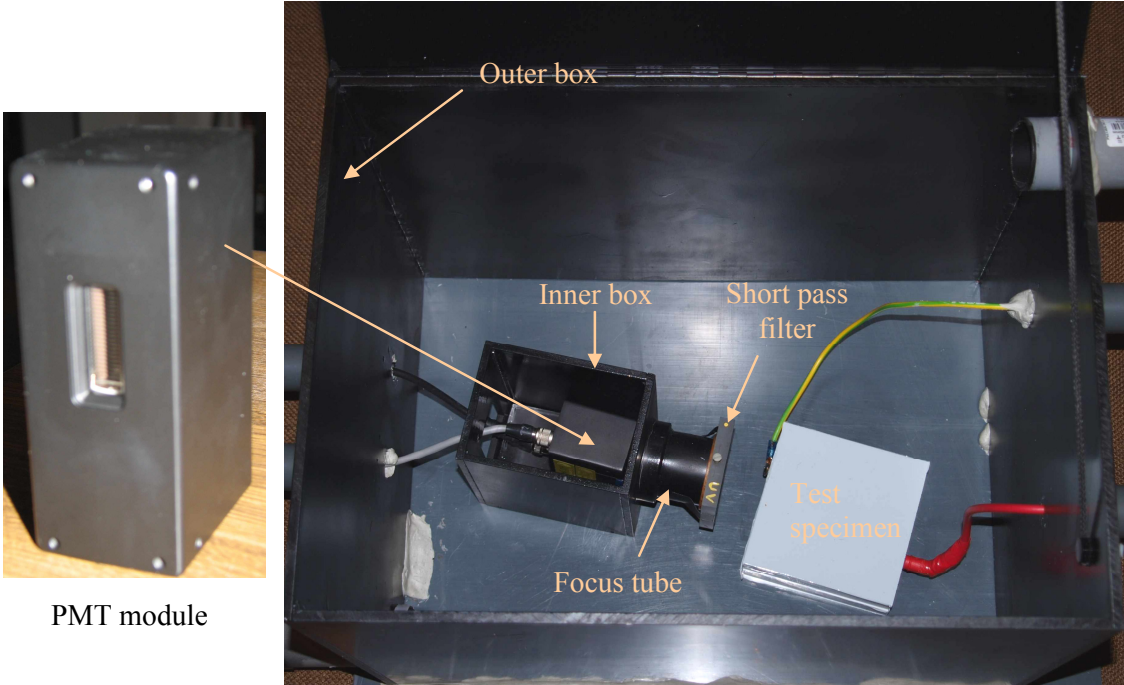


Figure 6.24: Hermetically closed boxes used for PMT the module

This is exactly the wavelength of the light emitted by electrical partial discharges. To avoid this effect the outer box is connected by a flexible tube to a ventilator which

exhausts the air with ozone out of the box as presented in **Figure 6.23**. The outer box has also a fresh air tube, thus the exhausted air is replaced by fresh air and in this way the air pressure and temperature inside the box is the same as outside the boxes. Due to the fact that ozone density is higher than air density, i.e. ozone settles on the bottom, the exhaust tube is placed at the bottom of the outer box. The fresh air tube is mounted at the top of the outer box in the opposite side of the box.

6.4 Climate Chamber

As an important part of this work the influence of ambient humidity and ambient temperature on the PD activity at the water drop on an insulating surface was investigated. Experiments at different values of relative humidity and temperature were performed using a climate chamber System Weiss, Type WK3-340/40. The inner volume is 340 litres and the inner dimensions are 750 x 580 x 765 mm³. The humidity can be varied from 10 % to 98 % RH, and the temperature from 5 °C to 95 °C. Humidity and temperature are independently controlled with a temperature deviation of 0,5 K. The refrigerating machine capacity is about 3 K/min. The chamber is equipped with a high-voltage bushing, allowing the connection of the test sample to the HV source.

6.5 UV Camera

In order to localize the partial discharges a MegaVis UV camera system is used for some of the measurements. The system consists of a 12 bit CMOS camera with a recording rate of 500 frames/s with a resolution of 1024x1024 pixels. The pixel size is 20 µm x 20 µm. The camera is connected to an Intensified Relay Optic (IRO) system equipped with an extremely fast gated high precision shutter control. It improves the performance of the camera and achieves the highest UV sensitivity. The spectral sensitivity of the high speed camera with the IRO is between 200 and 680 nm. The camera system has external TTL Trigger and synchronisation input channel.

In order to facilitate the localization of the partial discharges, the recordings made with the UV camera system are made from the top side, as presented in **Figure 6.25**. In order to analyze the drop shape deformation, before and after the voltage is applied, a picture of the water drop is taken. The superposition of these pictures with those

recorded during voltage application allows a precise localization of the partial discharges.

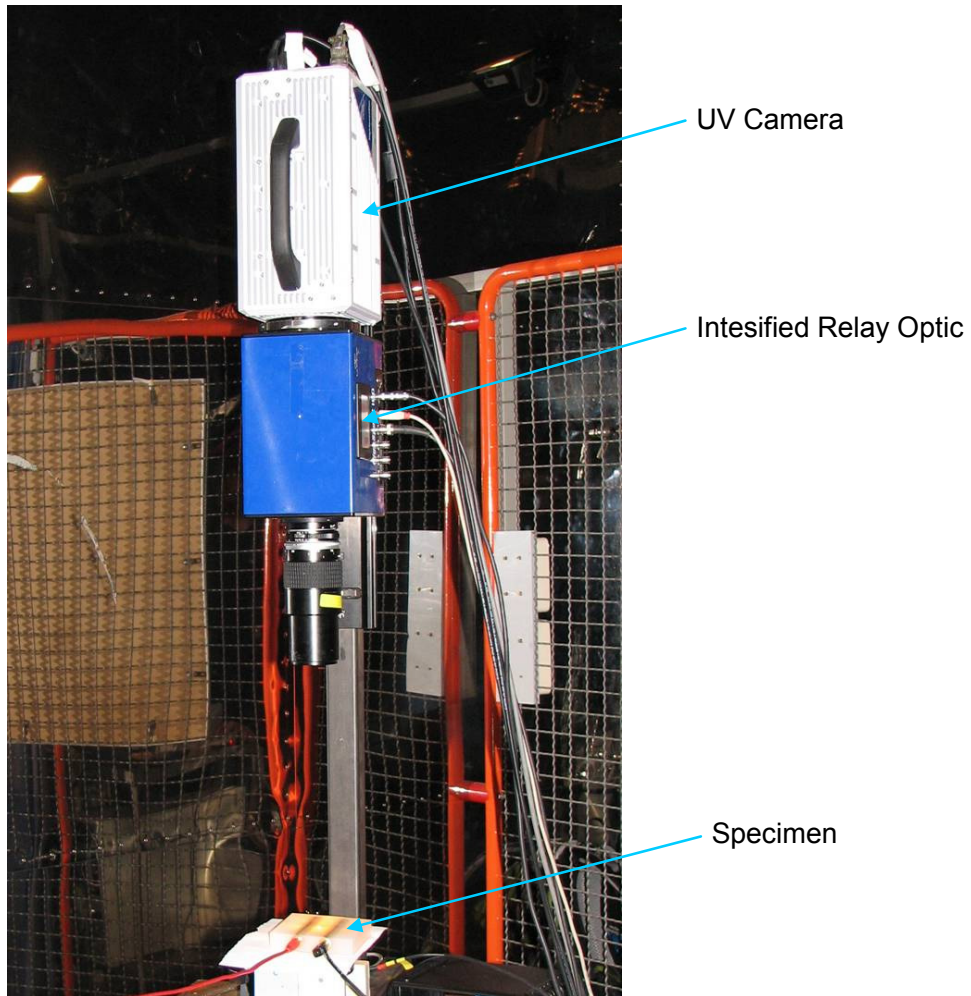


Figure 6.25: UV camera system

7 Results

7.1 Observations on Water Drops

7.1.1 Water Drop Deformation under Alternating Electric Field Stress

Water drops on an insulating surface are deformed under electric field stress. From a certain value of the electric field strength, the water drops start to change their form and to vibrate. If the electric field continues to increase, this can lead to water drop splitting. In [Kei2003] the behaviour of the water drop on an insulating surface is observed. Different parameters like water drop volume, conductivity and surface material are analyzed. The recordings are made only in two dimensional pictures which do not provide enough information about the deformation of the water drop. Therefore in this work, three dimensional recordings are made. The values of the parameters varied during the measurements are presented in **Table 7.1**. The water drop deformations under alternating and direct voltage stress are recorded. The three views (front, top and side view) are depicted from the complete frame and presented in form of tables. Two different patterns are observed.

For an 80 μl water drop with a conductivity of 55 $\mu\text{S}/\text{cm}$ a series of 11 frames is presented in **Table 7.2**. The recordings for pattern 1 are over one voltage period (20 ms). The water drop deformations are repeated during voltage application in a cyclic manner, even over one voltage period. Frame 1, 3, 6 and 8, 2 and 7, 4, 5 and 9, for example are identical. The water drop movement is correlated with the frequency.

Table 7.1: The varied parameters during recordings

Type of electrical stress	Volume in μl	10	20	30	40	50	60	70	80	90	100
	Conductivity in $\mu\text{S}/\text{cm}$										
AC, 50 Hz or DC	5	mn	mn	mn	s, m	m	s, m	mn	s, m	m	m
	35	mn	mn	mn	s, m	mn	s, m	mn	s, m	mn	mn
	55	mn	mn	mn	s, m	mn	s, m	mn	s, m	mn	mn
	100	mn	mn	mn	m	mn	m	mn	m	mn	mn
	500	mn	mn	mn	m	mn	m	mn	m	mn	mn

Note: m = measurement, mn = measured but not presented in this thesis and s = simulation

7 Results

Table 7.2: Water drop movement along a complete voltage period according to pattern 1
 Parameters: $V = 80 \mu\text{l}$; $\gamma = 55 \mu\text{S}$; $f = 50 \text{ Hz}$

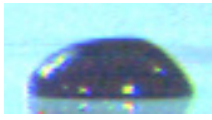

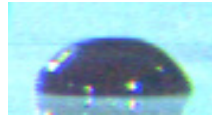

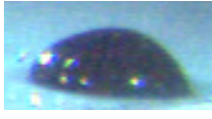
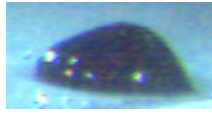
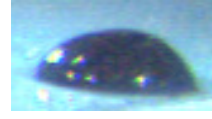

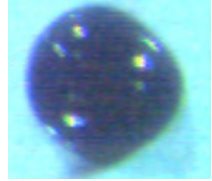
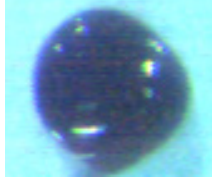
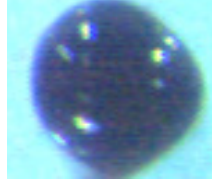
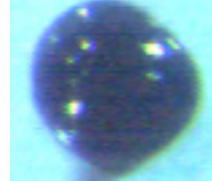
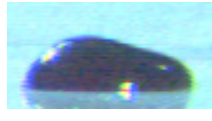
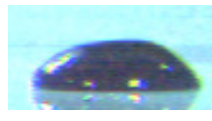
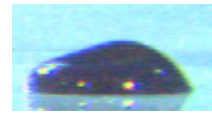
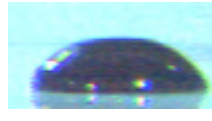
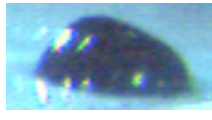
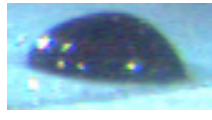
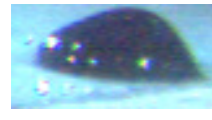
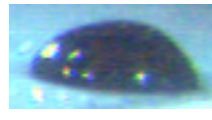
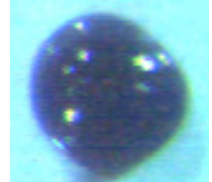
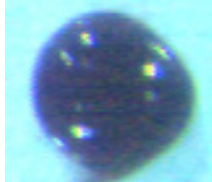

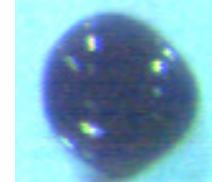
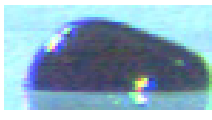
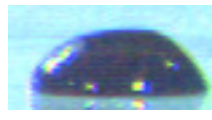
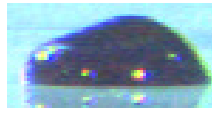
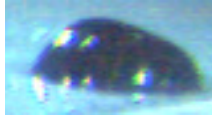
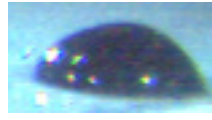
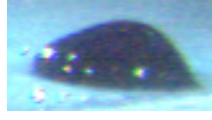
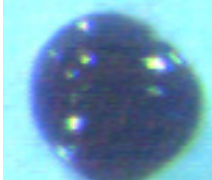


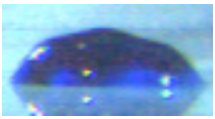
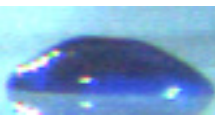
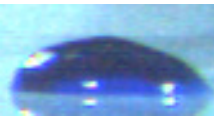
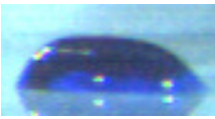
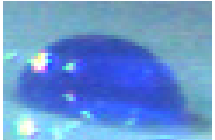
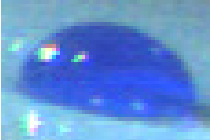
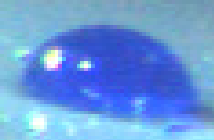
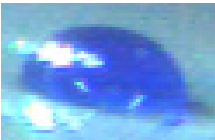
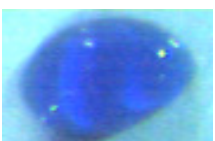
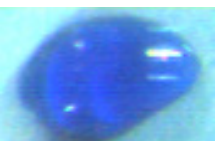
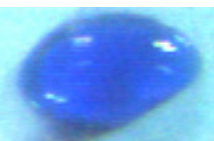
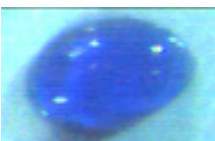
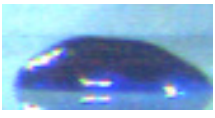
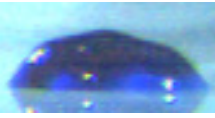
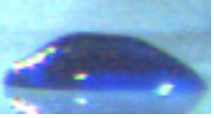
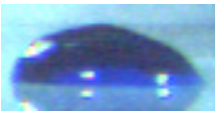
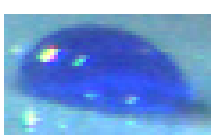
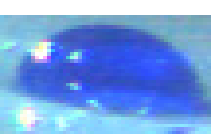
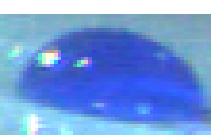
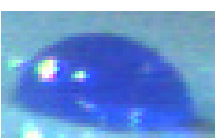
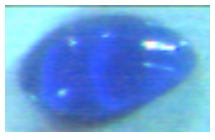
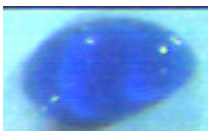
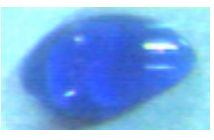
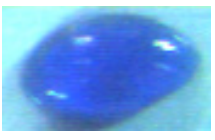
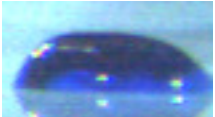

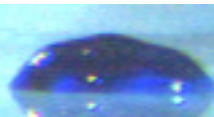
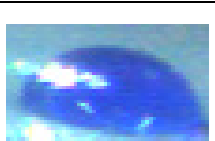
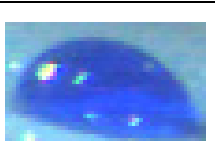
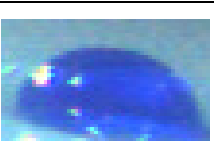
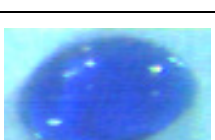
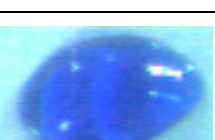
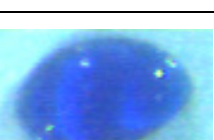
Frame	1	2	3	4
Front view x-y plane				
Side view x-y plane				
Top view y-z plane				
	$t = 0 \text{ ms}$	$t = 2 \text{ ms}$	$t = 4 \text{ ms}$	$t = 6 \text{ ms}$
Frame	5	6	7	8
Front view x-y plane				
Side view x-y plane				
Top view y-z plane				
	$t = 8 \text{ ms}$	$t = 10 \text{ ms}$	$t = 12 \text{ ms}$	$t = 14 \text{ ms}$
Frame	9	10	11	
Front view x-y plane				
Side view x-y plane				
Top view y-z plane				
	$t = 16 \text{ ms}$	$t = 18 \text{ ms}$	$t = 20 \text{ ms}$	

Table 7.3: Water drop movement along a complete voltage period according to pattern 2
 Parameters: $V = 60 \mu\text{l}$; $\gamma = 35 \mu\text{S}$; $f = 50 \text{ Hz}$

Frame	1	2	3	4
Front view x-y plane				
Side view x-y plane				
Top view y-z plane				
	$t = 0 \text{ ms}$	$t = 2 \text{ ms}$	$t = 4 \text{ ms}$	$t = 6 \text{ ms}$
Frame	5	6	7	8
Front view x-y plane				
Side x-y plane view				
Top view y-z plane				
	$t = 8 \text{ ms}$	$t = 10 \text{ ms}$	$t = 12 \text{ ms}$	$t = 14 \text{ ms}$
Frame	9	10	11	
Front view x-y plane				
Side view x-y plane				
Top view y-z plane				
	$t = 16 \text{ ms}$	$t = 18 \text{ ms}$	$t = 20 \text{ ms}$	

The water drop deformations presented here can be divided in three groups: “centre deformation” for Frames 1, 3, 6, 8 and 10; “left deformation” for Frame 4, 5 and 9; “right deformation” for Frame 2 and 7.

The second pattern observed during recordings is presented in **Table 7.3**. The shape of the water drop is crossed by a wave-like structure. The water drop has a volume of 60 μl with a conductivity of 35 $\mu\text{S/cm}$. The concentration of the colorant is lower, resulting in a brighter colour of the drop. Five types of deformations are observed. Frame 1,6 and 11 as well as Frame 2 and 7, 3 and 8, 4 and 9, 5 and 10 have the same shapes. It can be observed that the shapes are repeated twice along one period. Because of the type of deformation presented by pattern 2 (wave-like structure) the top view shows less modification of the shape. The two patterns were observed also by [Kei2003], but due to the two dimensional recordings of the water drops, only the front view of the drops were described. In this work the three dimensional recordings allow observations of the water drops also from a side view and a top view.

From the recordings of the high speed camera system, for each pattern the most common deformations are selected. From these recordings the most critical (worst case) deformations of the water drops are chosen and they are modelled in **Chapter 8**.

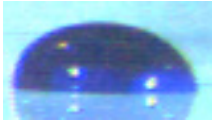
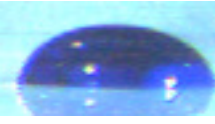

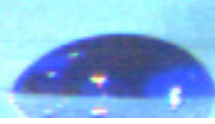

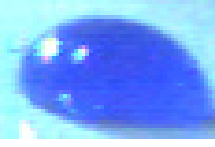
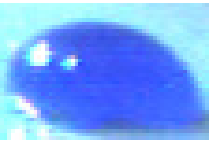
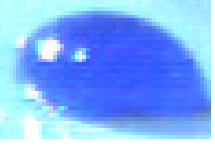

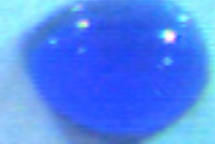
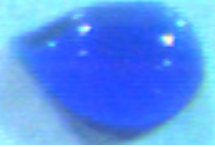

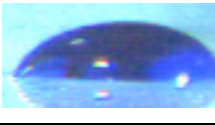

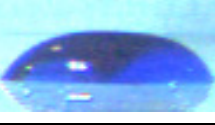
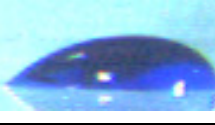
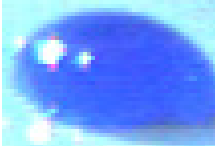


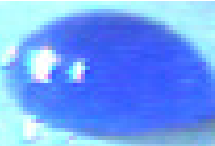


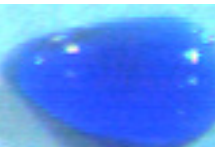
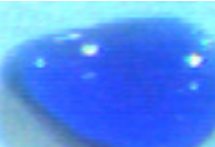

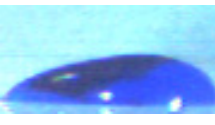
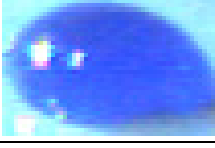


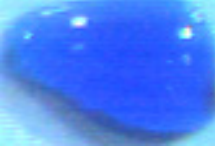
7.1.2 Water Drop Deformation under Direct Electric Field Stress

When the water drops are stressed by direct electric field the deformations of the drops are different compared to alternating electric field stress. The charge will be accumulated on the surface, and at a certain time the water drops will receive an impulse. After the impulse, due to the inertia, the water drop oscillates in a damped oscillation for several cycles. Typical water drop deformations are presented in **Table 7.4**. Frames 1 to 10 present a water drop of 60 μl volume and having 35 $\mu\text{S/cm}$ conductivity. From a recording time of 2 seconds (512 frames) 10 frames are presented. At $t = 0$ no water drop deformation is observed. After 0,46 s the water drop starts to elongate asymmetrically towards the electrodes. Frames 3, 4, 5, 6 and 7 show the development of the elongation of the water drop. At $t = 1,456$ s the water drop receives the second impulse and the elongation becomes larger.

In comparison with [Kei2003] observations, the water drops stressed by direct electric field recorded in this work are not stable. When the critical charge level is reached they deform asymmetrically towards the electrodes.

Table 7.4: Water drop movement under direct electric field stress






















Parameters: $V = 80 \mu\text{l}$; $\gamma = 55 \mu\text{S}$; direct voltage

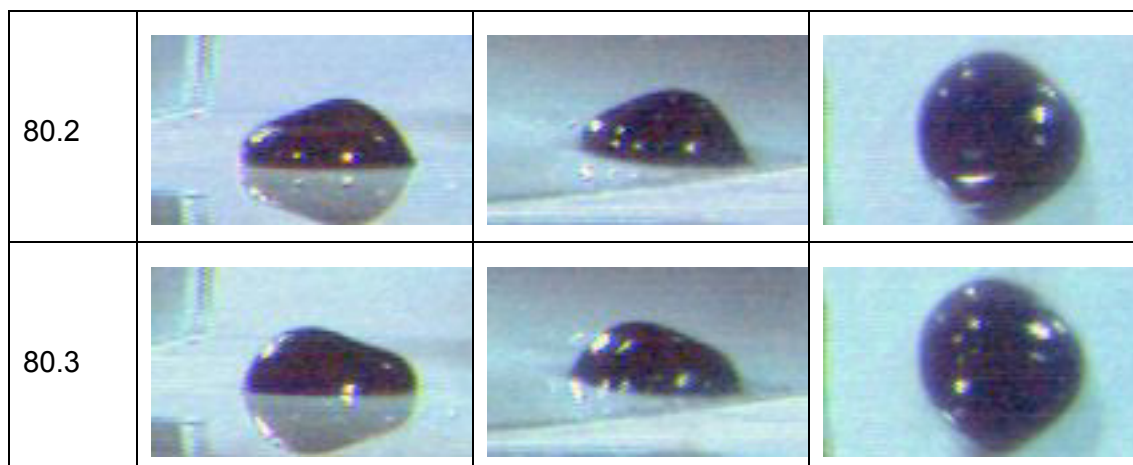
Frame	1	2	3	4
Front view x-y plane				
Side view x-y plane				
Top view y-z plane				
	$t = 0 \text{ s}$	$t = 0,460 \text{ s}$	$t = 0,488 \text{ s}$	$t = 0,496 \text{ s}$
Frame	5	6	7	8
Front view x-y plane				
Side x-y plane view				
Top view y-z plane				
	$t = 0,508 \text{ s}$	$t = 0,516 \text{ s}$	$t = 0,540 \text{ s}$	$t = 0,692 \text{ s}$
Frame	9	10		
Front view x-y plane				
Side view x-y plane				
Top view y-z plane				
	$t = 1,456 \text{ s}$	$t = 2 \text{ s}$		

7 Results

The pictures chosen for modelling and simulations from **Chapter 8** are presented in **Table 7.5** in all three view planes.

Table 7.5: Recordings chosen for simulations

Frame	Front view	Side view	Top view
40.a			
40.b			
40.c			
60.a			
60.b			
60.c			
80.a			



7.2 Partial Discharge Activity at Water Drops

7.2.1 Comparison between PD System and PMT System Recordings

In the beginning, the partial discharge activity at the water drop on a insulating surface was measured exclusively using a PD measurement system as presented in **Chapter 6.2**. Due to the fact that the charge values are below 1 pC (the sensibility of the PD measurement system), when the discharge ignites the PD measurement system is not sensitive enough to record the first discharges at the water drop. Therefore, the photomultiplier system (PMT) was introduced.

A comparison between both measurement systems is presented in **Figure 7.1**. The considered background noise level is 1 pC for the PRPD system and 2 mV for the PMT system. The applied voltage is the same for both measurement methods and is given as rms measured values. At a voltage U_1 the partial discharges are detected neither by PRPDM nor by PMTM. When increasing the voltage to U_2 , the PRPD system is still insensitive, but the PMT system already gives a significant signal (peak value of 15 mV) from UV radiation, caused by first partial discharges. At a higher voltage U_3 , the PD system detects partial discharges for the first time, while the other system has reached an output voltage level in the range of 70 mV peak value.

For three different water drop volumes, the inception electric field strength is measured using the PRPD and the PMT measurement system. The values of the inception electric field strength are the absolute values calculated as in **Chapter 6.1.3**. Both systems indicate that the inception electric field strength increases with decreasing drop volume, but from **Figure 7.2** it is clear that the PMT system is more sensitive than the PRPD system.

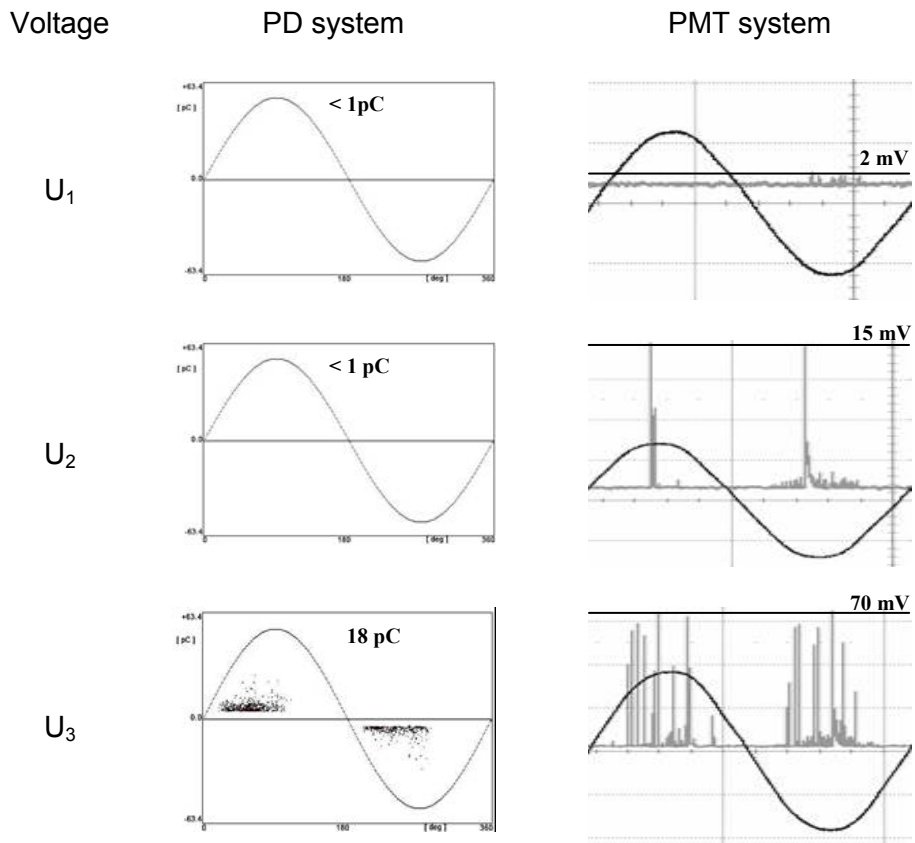


Figure 7.1: Comparison between PRMD system and PMT system

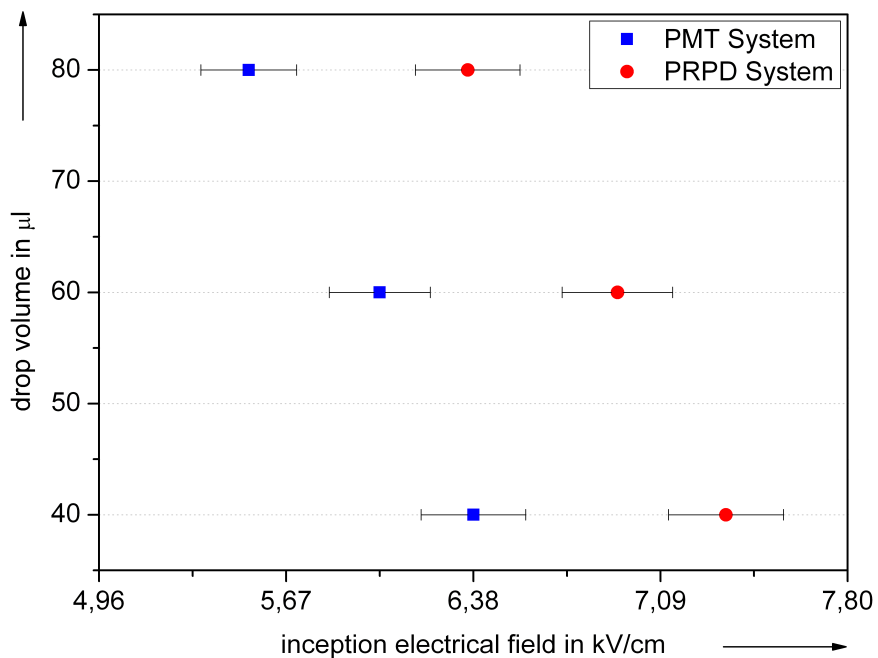


Figure 7.2: Partial discharge measurement using PRPD and PMT systems

(RH = 56 %; T = 24°; γ = 55 μs)

The difference between the values measured with both systems is between 6 - 16%. The values taken by the PMT system are considered as “true” values and are thus the reference.

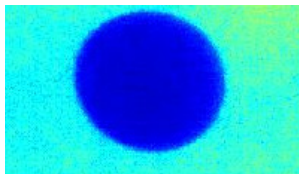
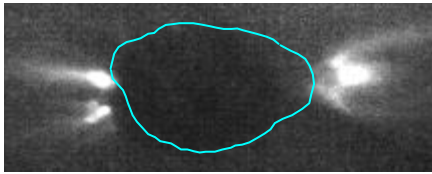
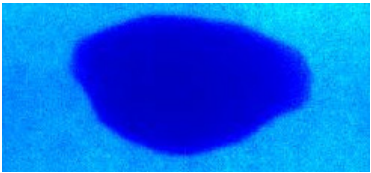
Based on these values, from now on the PMT system will be used for further measurements. Exceptions are made when the high speed camera is used. The necessary illumination for the recordings would damage the PMT system. In order to calculate the “true” values of the inception electric field when only the PRPD system is used, the following correction factor is used:

$$E_{\text{PMT}} = 0,9 \cdot E_{\text{PRPD}} \quad (7.1)$$

7.2.2 Localization of the PD under Alternating and Direct Field Stress

By using a PMT system, the PD activity can be quantified. In order to localize the partial discharge, UV-camera recordings are made². The applied measurement system is presented in **Chapter 6.5**. Before and after each recording the drop image is captured. The picture taken afterwards is superimposed to the discharge picture. The resulting picture contains the contour of the deformed water drop and light emissions from PD.

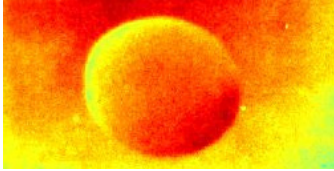
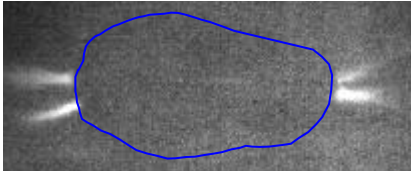
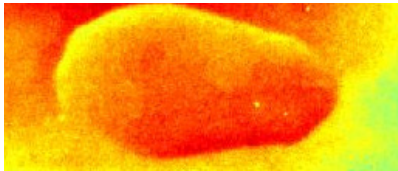
Table 7.6: UV-camera recordings of a 40 µl water drop under alternating field stress

Before voltage application	
Location of the partial discharge during voltage application	
After voltage application	

² Only on some configurations due to limited availability of the UV-Camera. Many thanks to Technische Universität Braunschweig.

In **Table 7.6** a result for 40 μl water drop is presented. The applied electric field is 7,4 kV/cm. The first picture is the top view of the water drop before voltage application and the third one is the same view but after voltage application. The middle picture is

Table 7.7: UV-camera recordings for a 40 μl water drop under direct field stress

Before voltage application	
Location of the partial discharge during voltage application	
After voltage application	

taken during voltage application. The observed white tiles are partial discharges which develop from the deformed water drop contour. As it can be observed, the partial discharges develop from the triple points towards the electrodes in the direction of the electric field lines.

The same procedure is repeated for a water drop under direct voltage stress. A 40 μl water drop is stressed by a 7,89 kV/cm electric field. The visualization of the partial discharge during voltage application is presented in **Table 7.7**. The drop is elongated towards the electrodes. Again the PD starts at the water drop edges. Due to the fact that under direct voltage stress the drop does not scintillate as under alternating voltage stress, the deformation of the water drop is produced by only one strong step movement. The charge accumulated on the water drop is discharged once, and this will produce the strong elongation of the drop. The contour of the drop after voltage application is superimposed on the UV camera pictures. It is obvious that the discharges start at the triple points which are thus the critical points for partial discharge inception.

7.2.3 Inception Voltage at Different Volumes of the Water Drop

Using the sample presented in **Chapter 6.1.1**, the partial discharge inception conditions at a single water drop are investigated. For this purpose, a series of different distilled water drop volumes are placed on the insulating surface. Afterwards, the voltage is increased until the partial discharges are detected. The applied electric field along the surface is calculated, as presented in **Chapter 6.1.3**. The values presented in **Figure 7.3** are mean values and are calculated from a series of ten measurements, with a confidence interval of 95 %.

The inception electric field strength at the insulating surface varies with the water drop volume. The mean value is 6,2 kV/cm. While at 30 μl water drop the electric field strength is 6,75 kV/cm, at a bigger water drop, 80 μl , the electric field strength is only 5,5 kV/cm. By increasing the water drop volume the inception electric field strength decreases. At small drops the surface tension and the intermolecular force of the liquid are equal, resulting in large contact angles. By increasing the water drop the equilibrium between the surface tension and internal forces of the liquid is destroyed, the contact surface between water drop and insulating surface is larger and the contact angle is smaller. Thus, large drops are more deformed than small ones under the influence of the electric field. They form sharper edges which are leading to local field intensifications. The results are compared with the values presented in the literature. [Mor2001] named the interval from 5 kV/cm to 7 kV/cm as the barrier interval for partial discharge inception phenomena.

The inception electric field strength of one 20 μl water drop was measured by [Hof1995] and has a value of 6 kV/cm. In [Phi1999] different water drop volumes, from 10 to 100 μl were used. Two different insulating surfaces were considered, one resulting in a contact angle of 115° and the other one 88°. For these two surfaces the inception electric field strength was measured. Due to the fact that the silicone rubber surface is hydrophobic, the contact angles of the water drops analyzed in this work (denoted as HST in the **Figure 7.3**) are about 100 - 110°. The smaller the contact angle, the lower is the inception electric field strength. The measurements are carried out at 65 % RH and a temperature of 21°C, 11 g/m³. The electric field strength measured at the given ambient conditions fits the interval given by [Phi1999] even though a sensitive measurement system is used (PMT). The values of the inception electric field strength shown by [Lop2001] are valid for water drops with smaller contact angles and are matching with the Phil_{min} values up to 80 μl water drops.

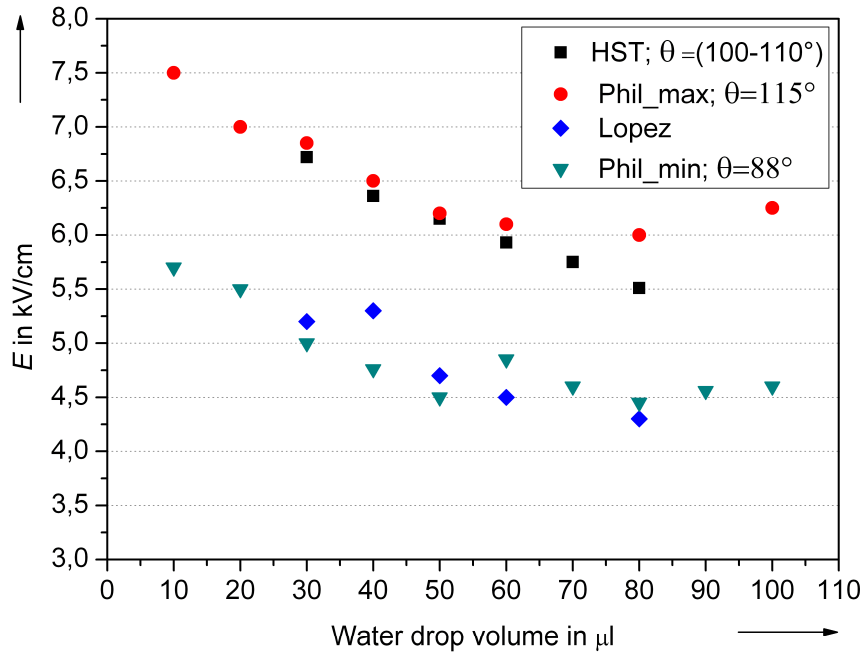


Figure 7.3: Water drop inception field strength as a function of water drop volume and comparison with the literature (HST: T: 22°C; H: 13 g/m³)

The volume of the water drop above the 80 μl , the shape of the drop is governed more by the gravity force than by the internal forces. By varying the ambient conditions, the electric field strength changes, see **Chapter 7.2.4**. For the results presented in **Figure 7.3** the literature provides no information about the ambient conditions. Therefore, the results from this work are not comparable with those presented in the literature. The influence of the ambient conditions should be considered.

7.2.4 Inception Voltage at Different Ambient Humidities

During measurements it was observed that the inception electric field values for the same parameters of the water drop vary from one measurement to the other. This could not be explained without assuming the influence of the ambient conditions. Therefore, the influence of ambient humidity on the PD inception electric field strength at the water drop on an insulating surface in atmospheric air is investigated. Each experiment was performed at a constant temperature, and the relative humidity was varied, increasing from 20 % to 80 % at approximately 10 % steps. The maximum variation in the measured humidity is $\pm 1,2$ % at any given experimental condition. The maximum temperature deviation from the rated condition is 1.5 K.

When the given combination of humidity and temperature is achieved, the PD inception voltage is measured by slowly increasing the voltage until the first discharges were

observed by the PMT. The PD inception voltage is measured five times, and the mean value and standard deviation are calculated. The electric field strength values presented are the rms values of each five measured values and are calculated as in **Chapter 6.1.3**. For the reference value of the inception voltage, i.e. inception voltage at an absolute humidity of 11 g/m^3 , which is considered the normal value in [IEC 60052], ten measurements are taken, and then the mean value is used. The results for PD occurring at the triple point of the water drop under atmospheric conditions are presented in **Figure 7.4** and **Figure 7.5**.

Figure 7.4 illustrates the relationship between inception electric field strength and relative humidity at 283 K (10°C) and 313 K (40°C) for 40 μl , 60 μl and 80 μl water drops.

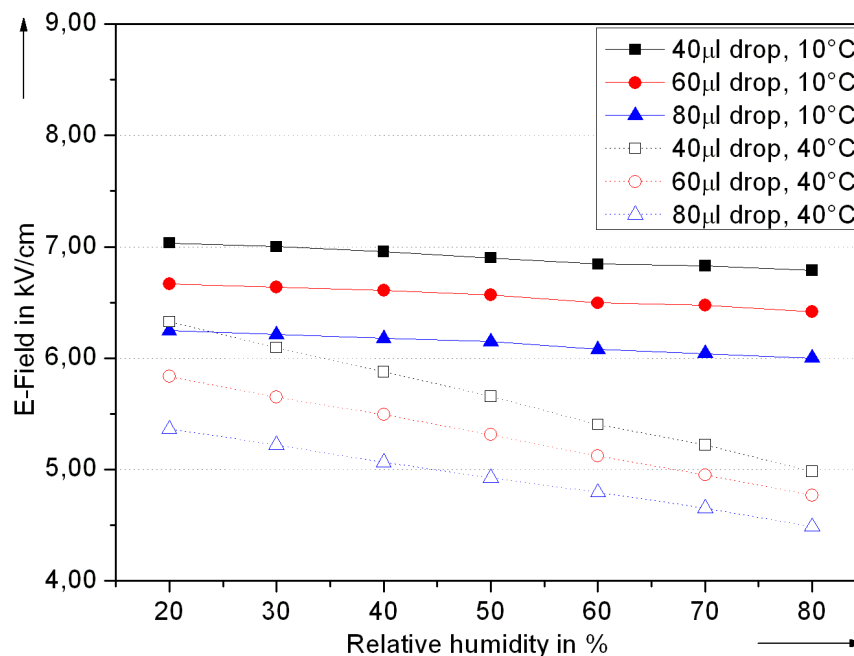


Figure 7.4: Inception electric field strength as a function of relative humidity, normalized to standardized pressure value, p_0

Figure 7.5 presents the dependence between inception electric field and the absolute humidity for the same water drop volumes, where the electric field strength is normalized to standard atmospheric conditions, $p_0 = 1013 \text{ hPa}$ and $T_0 = 293 \text{ K}$ using the relative density correction factor δ according to [IEC 60052]

$$\delta = \frac{p}{1013} \cdot \frac{273 + 20}{273 + \vartheta} \quad (7.2)$$

where p is in hPa and ϑ in $^\circ\text{C}$.

A comparison of the two representations shows that similar trends can be recognized. The first remark is that the inception electric field strength decreases with increasing absolute humidity. In **Figure 7.4**, the curves of inception electric field strength obtained for 10 °C and 40 °C show similar trends, but the slopes at 10 °C are smaller than those measured at 40 °C. This shows, that the ambient temperature also affects the inception electric field strength as expected, and therefore the temperature influence will be analysed in **Chapter 7.2.5**. The absolute humidity seems to be adequate for further investigations. Upon examination of the relationship between the inception electric field strength and absolute humidity, two regions can be identified. For all three drop volumes, below approximately 13 g/m³, the inception electric field strength rapidly decreases with absolute humidity. Between 13 g/m³ and 41 g/m³, the inception electric field strength decreases less pronounced than in the previous region.

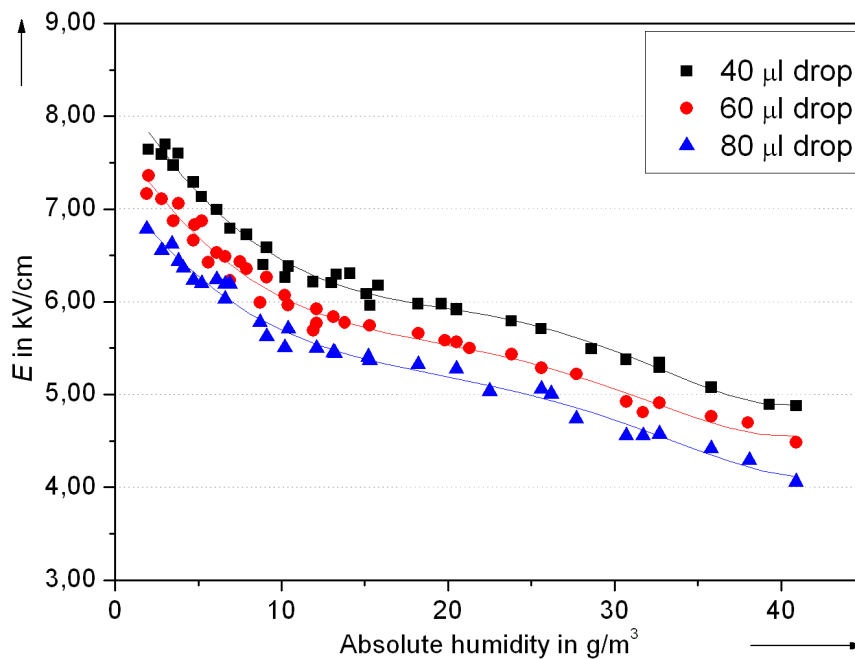


Figure 7.5: Inception electric field strength as a function of absolute humidity

Electric field values normalized to $\delta = 1$

Therefore, the experimental data are split into two regions. In **Figure 7.6**, region I from 2 g/m³ to 13 g/m³ is presented, and **Figure 7.7** exhibits the inception electric field strength measured between 13 g/m³ and 42 g/m³ (region II). The trends of the inception electric field strength, obtained for 40 µl, 60 µl and 80 µl drop volumes, are similar but the influence of the water drop volume, as presented in **Chapter 7.2.3**, is also visible.

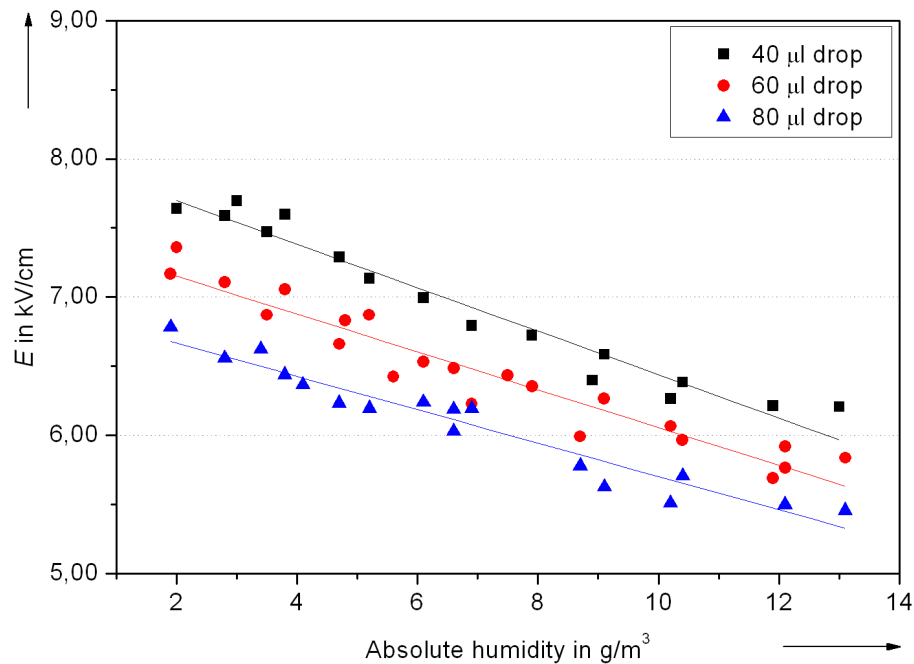


Figure 7.6: Inception electric field strength as a function of absolute humidity
Region I (2-13 g/m³)

The inception electric field strength decreases by increasing the drop volume. Due to the limitation of operating parameters of the PMT, it was not possible to increase the absolute humidity above 42 g/m³. Therefore, the validity of the relationship between inception electric field strength and absolute humidity could not be validated for humidities above 42 g/m³.

Figure 7.6 shows that for all three water drop volumes the inception electric field strength decreases by about 1,1 kV/cm, when absolute humidity increases from 2 g/m³ to 13 g/m³. The decrease rate is thus 2,3 %/g/m³. Considering inception electric field strength E_0 at the standard humidity, H_0 , of 11 g/m³ and the humidity H , the corresponding inception electric field strength can be calculated using

$$E = \frac{E_0}{100} \left[1 - \frac{2,3}{100} \cdot (H - H_0) \right] \quad (7.3)$$

where E and E_0 are in kV/cm. The solid lines in **Figure 7.6** represent the calculated values of inception electric field strength using (7.3).

For region II the inception electric field strength decreases only slowly with absolute humidity, see **Figure 7.7**. From 13 g/m³ to 42 g/m³ the decrease is only 1,6 kV/cm, corresponding to a decrease rate of 0,8 %/g/m³. In this case, the inception electric field strength can be calculated using

$$E = \frac{E_0}{100} \left[1 - \frac{0,8}{100} \cdot (H - H_0) \right] \quad (7.4)$$

The correlation factors between the measured and the calculated values for both regions are presented in **Table 7.8**.

Table 7.8: Correlation factors between the calculated and measured values of the electric field strength

Region	40 μl	60 μl	80 μl
I (2 – 13 g/m^3)	0.976	0.960	0.972
II (13 – 42 g/m^3)	0.989	0.983	0.984

As the correlation factor is almost one, the values of the correlation coefficient indicate that the calculated values are very close to the measured values. And as E_0 , H_0 and H are known, the inception electric field at the water drop on an insulating surface at different ambient conditions can now be calculated.

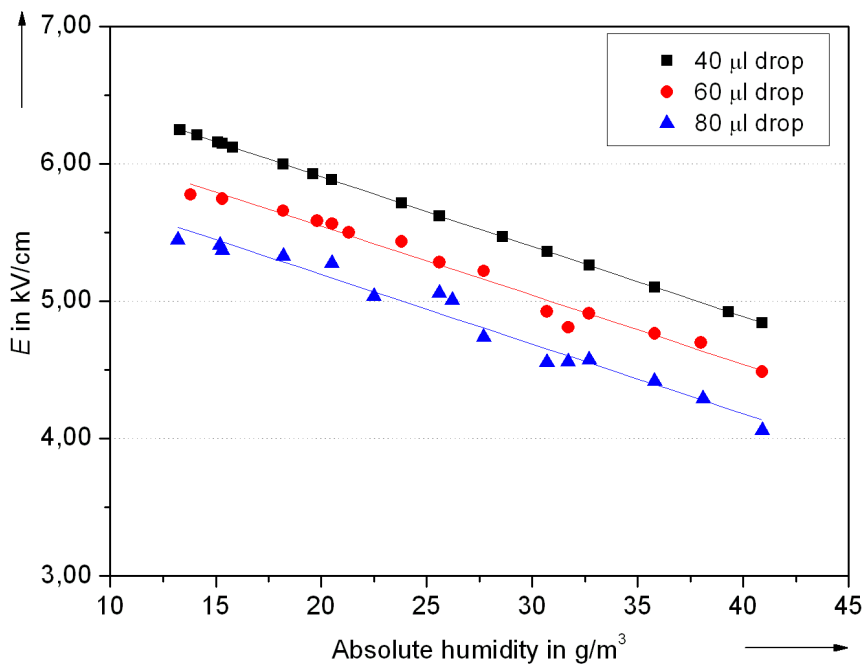


Figure 7.7: Inception electric field strength as a function of absolute humidity

Region II (13-42 g/m^3)

The inception electric field strength curves obtained for PD in atmospheric air occur at the triple point of a water drop on an insulating surface. As it is known, the breakdown voltage increases with rising humidity. The expectation would be that the inception electric field strength would increase also with the increase of the humidity. But the

measurements show that the inception electric field strength decreases with increasing humidity. The results present two different inverse proportional relationships between the inception electric field strength and absolute humidity. Considering data with absolute humidity of 2 g/m^3 and above, the decrease of the inception electric field strength suggests that absolute humidity affects the discharge mechanisms in different ways, depending on the humidity range, region I and II, respectively.

Atmospheric air contains neutral particles, positive and negative ions. Positive and negative ions can be further divided into small ions and large ions. Their concentration in the air depends on atmospheric conditions. If a space charge is introduced in non-turbulent air, the density of charged particles decays, see **Chapter 5.4.2**.

On the insulating surface, in the neighborhood of the triple zone, the first positive discharge can be described as a cladding of positive streamers. The starting point is the electron avalanche triggered by a primary electron, where the primary electron comes from a negative ion. Humidity influences the concentration of o_2^- ions or the negative ions in terms of total concentration of ions; therefore, it controls the amount of detached electrons and corona inception characteristics. Hence, at high humidity a large number of negative ions are present and the probability of avalanche formation will be higher than at low humidity. The number of negative ions increases exponentially with the increase of the absolute humidity. In region I the increase of the negative ions is faster and therefore the probability of avalanche formation is higher, i.e. the decrease of the inception voltage is faster. In region II, the number of negative ions is already high, and upon increase of the humidity the number of negative ions does not change considerably. Thus the probability of avalanche formation increases slowly and the decrease of the inception voltage is slower than in region I, respectively.

Since the PD strength of atmospheric gas depends on the moisture content, the absolute humidity rather than the relative humidity is the parameter of interest for determining the influence of ambient conditions on the PD behaviour at different humidity levels. When using the correction factors presented in (7.3) and (7.4), the calculated values of the inception electric field correlate very well with the measured values which can be used to predict exactly the inception electric field at the water drops on an insulating surface.

The practical importance of this chapter is that the ambient conditions, i.e. absolute humidity, influence PD activities reversely compared with the general breakdown electric field strength. The ambient conditions should always be measured when PD measurements are carried out. Long-term PD activity observations and measurements

will only be of any relevance if the results are obtained under the same humidity conditions or if they are corrected with respect to the humidity level.

7.2.5 Inception Voltage at Different Ambient Temperatures

The ambient temperature is also a parameter that influences the inception electric field strength at water drops on insulating surfaces. Due to the operating interval limitation of the PMT module, the investigated temperatures vary between 278 K (5°C) and 313 K (40°C) but these are typical values for ambient temperature. The ambient humidity is constant and only the temperature varies. The measurements are carried out using the climate chamber presented in **Chapter 6.4**. The first remark from **Figure 7.8** is that the inception electric field decreases with increasing temperature. By increasing the relative humidity, the inception voltage decrease slope is smaller.

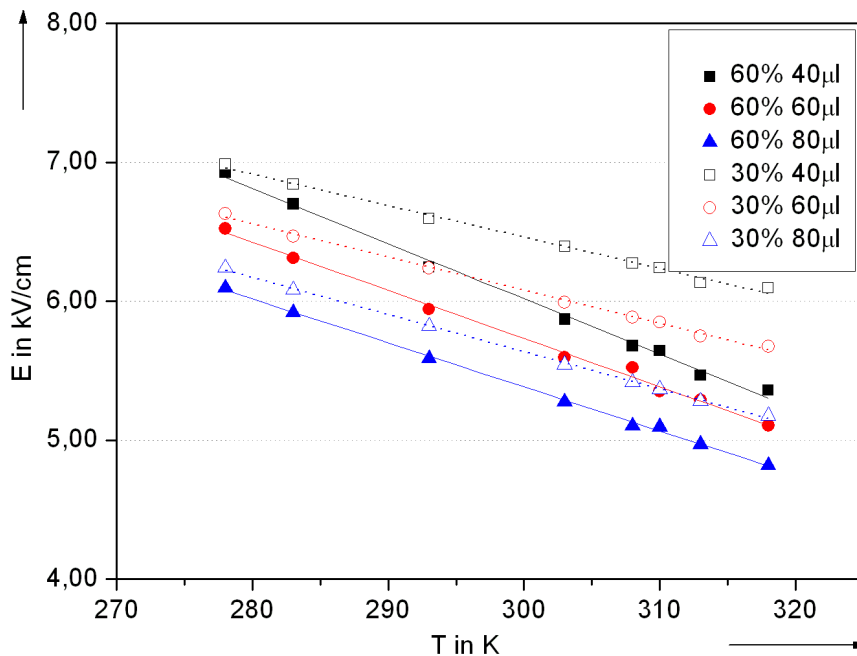


Figure 7.8: Inception electric field strength as a function of ambient temperature normalized to standard pressure p_0

For 60 % relative humidity, the inception electric field strength decreases faster by increasing the temperature. At higher temperatures, the gas density is smaller, the free path become higher and in this way the ionisation conditions will be more favourable than under normal conditions. In this way, the charge particles involved in the ionization process are faster and the probability of inelastic collisions is higher. These results are in line with [Bra2007] at high humidity.

8 Modelling and Simulation of the Water Drops on a Insulating Surface Stressed by Electric Field

8.1 Modelling

The deformations of the water drop should be modelled based on high speed camera pictures presented in **Chapter 7.1**. The electric field intensifications are then analyzed at the deformed drops. Due to the eigenmodes of the water drop and change of the drop's shape during one voltage period, a large number of models should be done. Therefore, the scientific approach is the simulation of the movement and deformation of the water drop. In the simulation hydro-dynamic as well as the electro-dynamic forces should be considered. Since there is no software which can solve both, a new tool should be developed. The development of such software would involve about three researchers for about two years. For this reason a compromise should be made: the deformation of the water drop is modelled manually and then imported in the electric field solver.

Water drops have to be modelled with the help of design software which has to fulfil two basic requirements. First of all, the shape should be precise, and secondly, the volume of the model drop must be the same as for the actual water drop. The *Solid Works* software [Sol2009] has proved to be an adequate tool for this task. Starting from the high speed camera frames each drop has three view planes. For each plane a curve is drawn, and from these three curves, a surface and a volume are automatically generated, respectively. In some cases, when the deformation of the drop is not symmetrical, more than one curve per view plane is necessary. In **Figure 8.1** three curves at different x positions are drawn in order to exactly model the deformation of the drop. The volume difference between the actual water drop and the water drop model (calculated by the software tool) is within +/- 2,5 %.

In **Chapter 7.1** the deformations of the water drop are observed on a hydrophobic surface (silicone rubber surface). From these recordings the most critical deformations are modelled. In this way the maximum electric field intensifications are obtained. In the presence of a hydrophilic surface much more critical deformation can occur and much higher electric field intensifications, respectively. The case of the hydrophilic surface is not a subject of this work and therefore the presented critical deformations are valid only for hydrophobic surface.

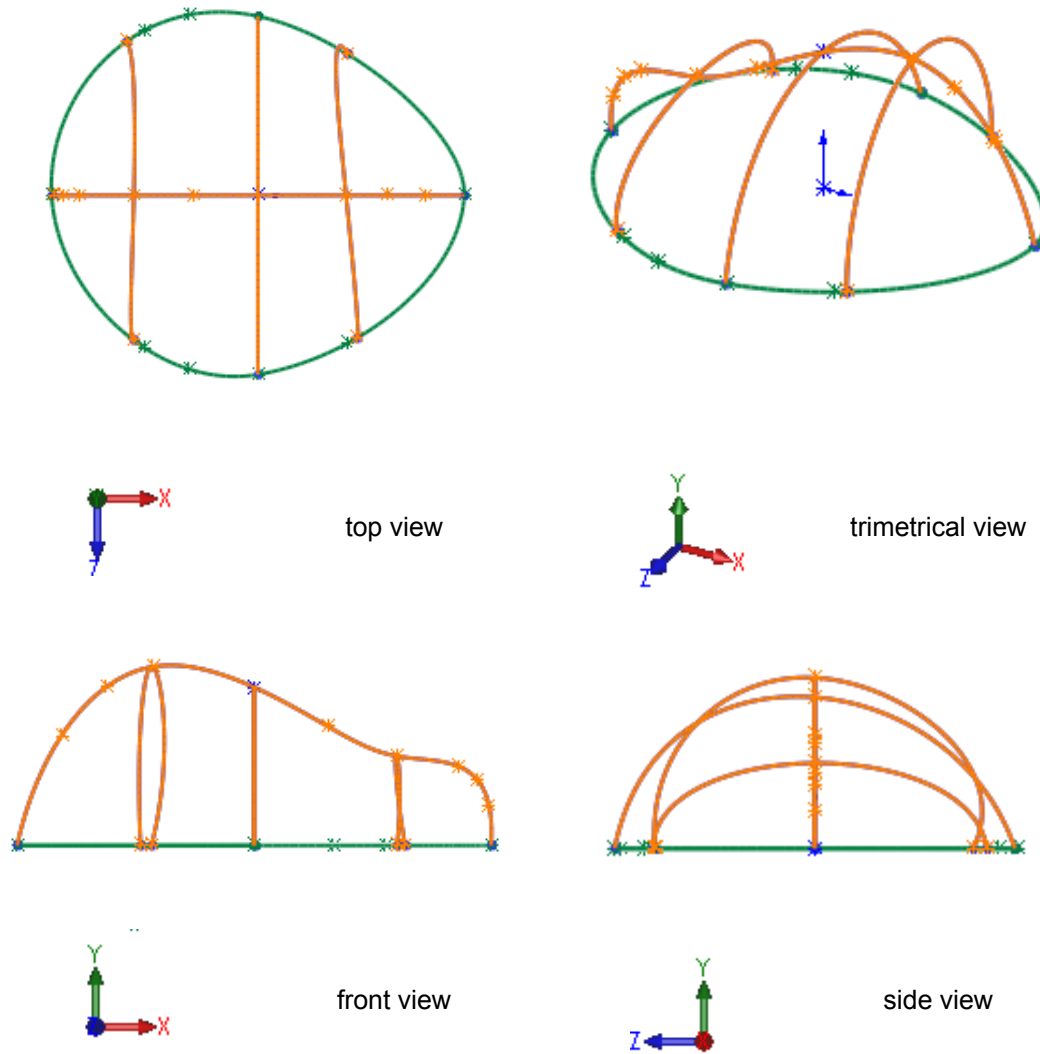



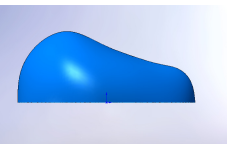
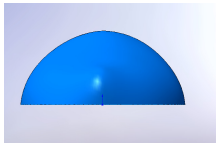
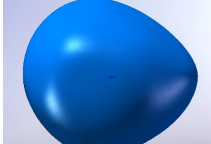


Figure 8.1: Water drop model using contour curves

Table 8.1: Three dimensional view of the deformed water drop (80.c)

Water drop	Front view (xy)	Side view (yz)	Top view (xz)
Recorded frame			
Modelled frame			

The water drop deformations recorded with the high speed camera and presented in **Table 7.5** are modelled in SolidWorks. As an example the three view planes of drop 80.c are presented in **Figure 8.1**. The water drop model shapes are very close to recorded shapes.

The recorded water drops shapes are modeled and simulated and the shapes which exhibit the highest electric field intensification are named the most typical water drops. In the next chapter the typical water drop frames presented in **Table 7.5** are modelled as described above.

8.1.1 Modelling of a typical 40 μl Water Drop

In a sequence of ten pictures during one voltage period, the water drop deformations are repeated and therefore three typical deformations were chosen. The three water drop deformations are modelled. In **Figure 8.2** the recorded and modelled water drop deformations are presented.

In the upper line are the camera recordings and at the bottom the modelled water drops. For drop 40.a the difference between the left and right contact angle is not substantial, they are between 60° and 80° . The volume of the modelled water drop is $41,1 \mu\text{l}$ which is in the $\pm 2,5 \%$ error range.

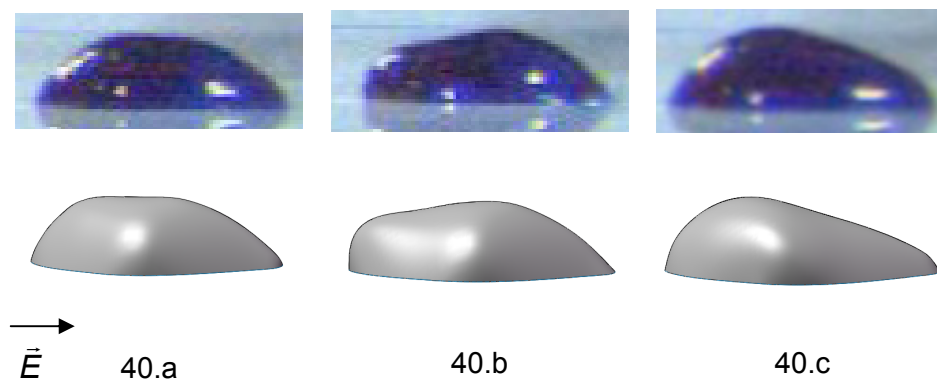


Figure 8.2 Camera recordings and models of three critical deformations for a $40 \mu\text{l}$ water drop
(only front view is shown)

The surface of drop 40.b forms wave-like structure and is not symmetrical. While the left contact angle is 90° , the right one is much smaller. The modelled drop 40.b has a volume of $40,8 \mu\text{l}$. The main volume of the drop 40.c is moved to the left side and the contact angles are between 45° and 70° . The volume of the modelled drops is $41,2 \mu\text{l}$. The contact angles are smaller than it would be expected on a hydrophobic surface. The reason is the electrodynamic forces which stretch the water drop towards the

electrodes. As the liquid oscillates on the surface the tendency is to keep the same contact surface with the solid and therefore the contact angles change drastically.

8.1.2 Modelling of a typical 60 μl Water Drop

In the same way as for the 40 μl water drop already presented, from a sequence of ten high speed camera recordings, three critical deformations of the water drop are modelled. In contrast to the 40 μl water drops where the drop is moving towards the electrodes, in this case the water drop contracts and relaxes more symmetrically to the middle point of the drop.

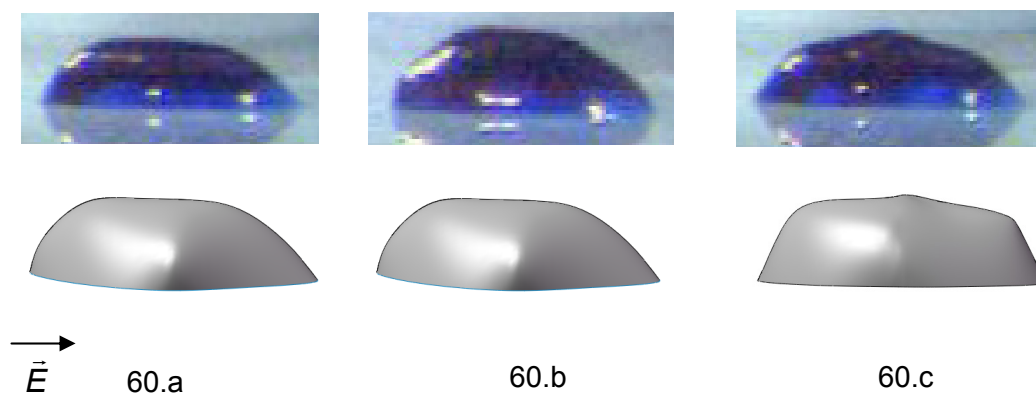


Figure 8.3: Camera recording and models of three critical deformations for a 60 μl water drop
(only front view is shown)

The water drop shapes approximately present symmetry with respect to an imaginary vertical line through middle of the water drop, see **Figure 8.3**.

The volume of the drop model 60.a is 60,2 μl . The right contact angle is smaller than the left one but is in the range $70^\circ - 90^\circ$. The model 60.b is expanded in the electrodes direction and has a volume of 61,3 μl . On the right side the contact angle is similar with model 60.a. The third model, drop 60.c, has an atypical shape. The sharp contour is difficult to be described by curves; it is an unusual deformation for liquids. Both contact angles are in the range of 65° , and the model has a volume of 61,4 μl .

8.1.3 Modelling of a typical 80 μl water drop

Three most critical deformations are modelled for 80 μl water drop. In **Figure 8.4** they are presented together with the corresponding high speed camera recordings. The deformation shapes are similar with the models for 40 μl . A part of the fluid is travelling

like a wave from left side to the right side of the drop and backwards. In comparison with models from 60 μl the curvatures are much softer.

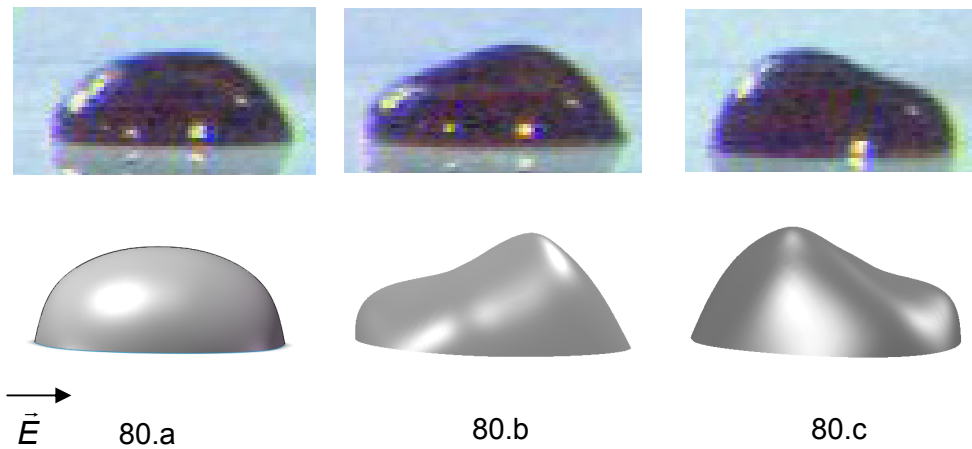


Figure 8.4: Camera recording and models of three common deformations for a 80 μl water drop

Model 80.a presents a symmetrical contour, the left contact angle is 90° and the right contact angle is smaller. The volume of the model is 81,3 μl . In contrast to the previous model, 80.b does not present any symmetry. The main water volume is moved on the right side. The left contact angle is 90° and the right one is more acute than the one in model 80.a. The volume of model 80.b is 79,3 μl . The last model, 80.c shows mirroring similarity to the previous model but the top of the drop is not as sharp as in 80.b. The volume of the model is 80,8 μl .

The models 80.b and 80.c have sharp edges at the top of the drop. As the goals are to precisely model the triple point zone, and to obtain the exact volume of water drop, the top of the model is not the point of interest. Also the highest electric field intensifications are at the triple point and not at the top of the water drop.

8.2 Simulations

8.2.1 Simulation Considerations

The electric field distribution at the water drop on an insulating material is simulated using CST EM Studio software [EMS2009]. The electric field simulations are performed taking into account the voltage value, geometry and material parameters. The shapes of the deformed water drop presented in **Chapter 8.1** are used for the simulations.

The electric field enhancement is analyzed on the insulator surface along a path 0,1 mm above the insulator surface, as presented in **Figure 8.9**. The area of interest is the area between the electrodes where the electric field is homogeneous. Due to the

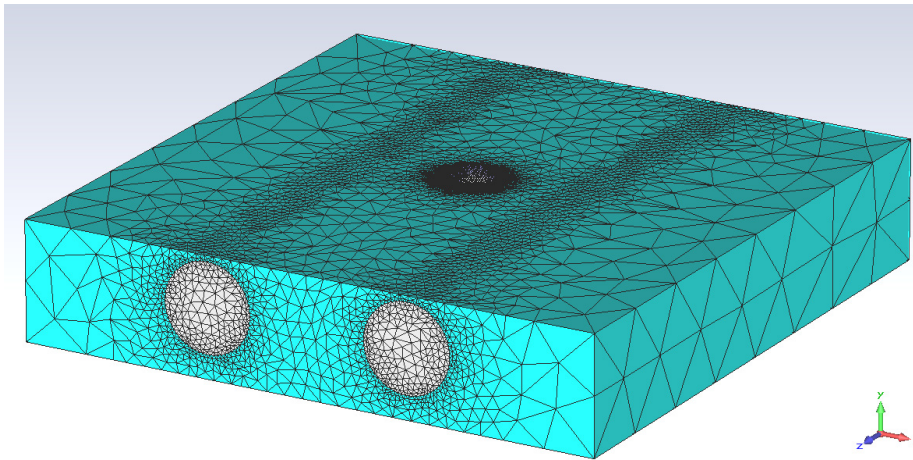


Figure 8.5: Tetrahedral surface mesh settings for the complete sample

curvatures of the water drops, the tetrahedral mesh is the appropriate choice for this application. The surface mesh of the complete specimen is presented in **Figure 8.5**. But the main focus of the simulation is on the region of the water drop edges where the resolution of the mesh is therefore very carefully chosen.

In order to minimize discretization errors, the transit from rough mesh to very fine mesh is done in smaller steps. **Figure 8.6** presents the surface mesh cells in the vicinity of the water drop.

Using the mesh settings described above the electric field distribution is calculated. The values of the electric field in each point of the considered arrangement are presented. The values of the electric field presented by the colour palette correspond to a voltage of 1 kV between the electrodes. In **Figure 8.7** it can be observed that the high electric field strength is concentrated on the region between the electrodes. Moreover, at the water drop even higher values of the electric field strength are present. In **Figure 8.8** a closer view is given, and the critical points are the water drop edges in the direction of the electric field lines. These areas will form the starting points for partial discharges, and in the long run for ageing processes. Therefore, a detailed analysis of the electric field values is conducted. The distribution of the electric field strength on the insulating surface is considered along defined paths from **Figure 8.9**. In order to attain the maximum electric field at the triple point, two paths are used: one in silicone rubber and one in air in the xy plane.

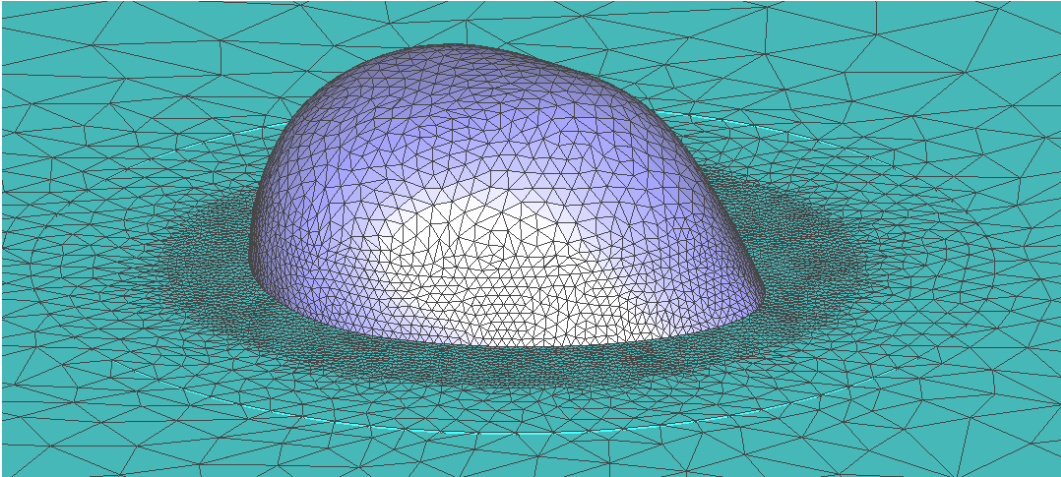


Figure 8.6: Tetrahedral surface mesh settings at the water drop

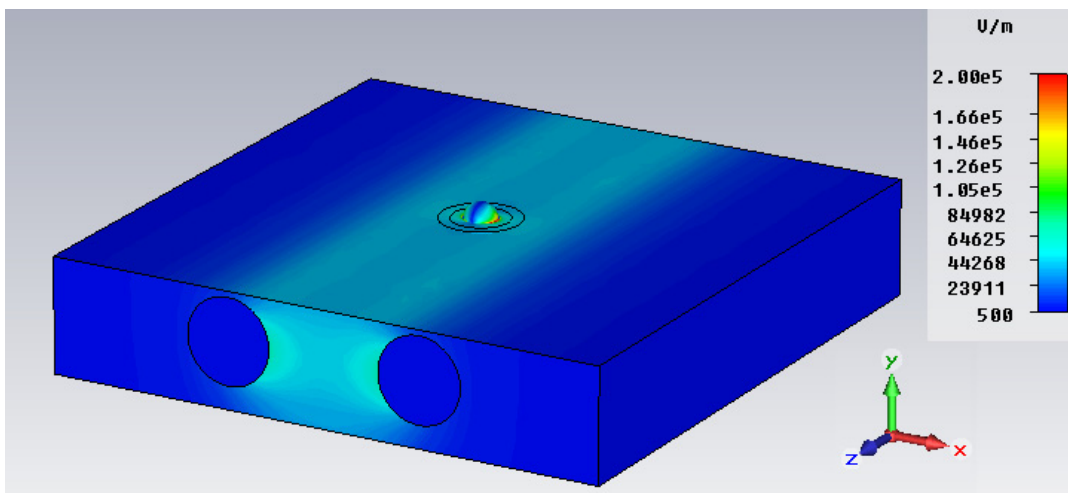


Figure 8.7: Electric field distribution on the specimen surface at $U = 1$ kV

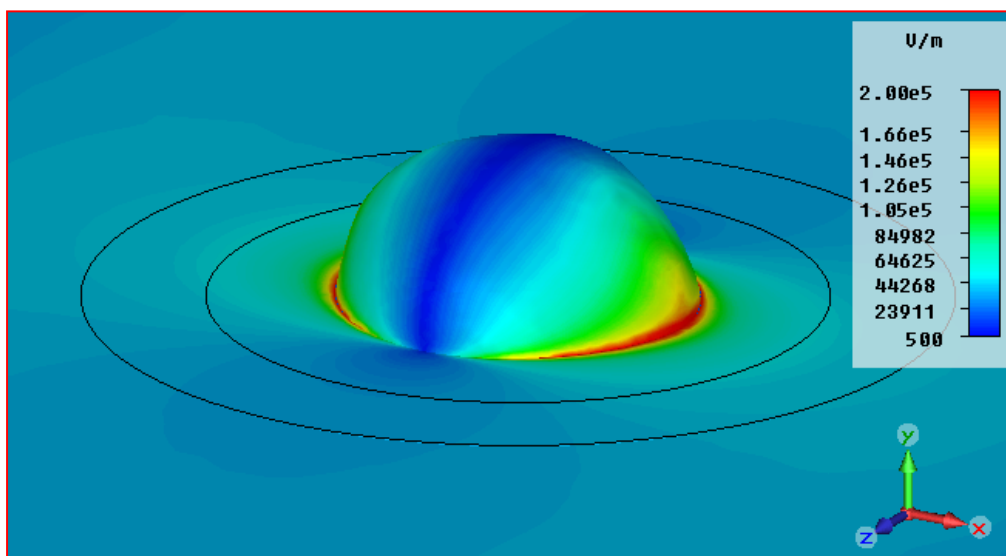


Figure 8.8: Electric field distribution in the vicinity of the water drop at $U = 1$ kV

The reason for the two paths is that at the interface between the insulating material and air, the mesh cell can still possess the properties from the silicone rubber. As the mesh step is 0,09 mm, at a distance of 0,1 mm from surface, for sure the value of the electric field strength corresponds to a mesh cell in air. In the xz plane, due to the asymmetrical deformation of the drop, 12 paths at

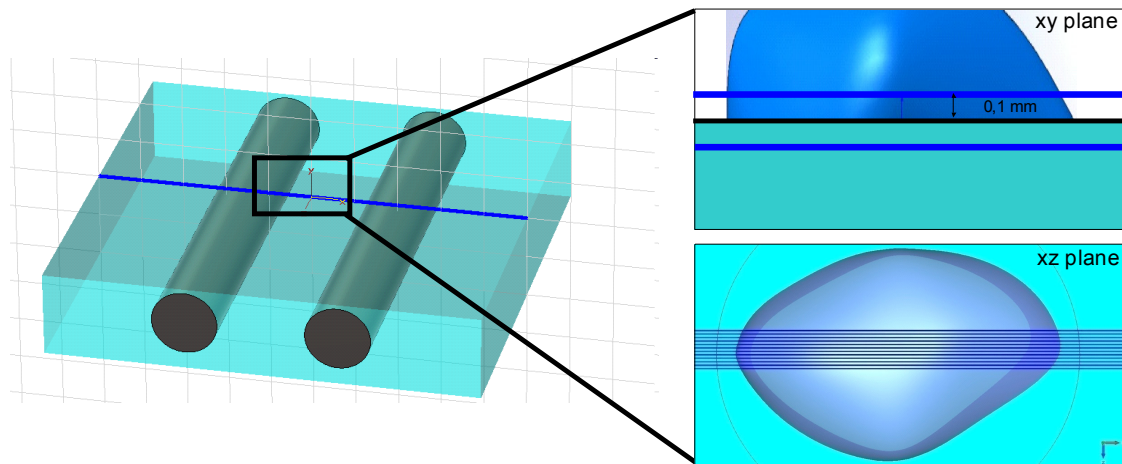


Figure 8.9: Position of the paths for the electric field strength analysis

different z-axis positions are analyzed.

The typical tangential component of the electric field distributions along the insulating surface in the presence of water drop are presented in **Figure 8.10**. The twelve curves correspond to the 12 paths in the xz plane. The curves show different peak amplitudes.

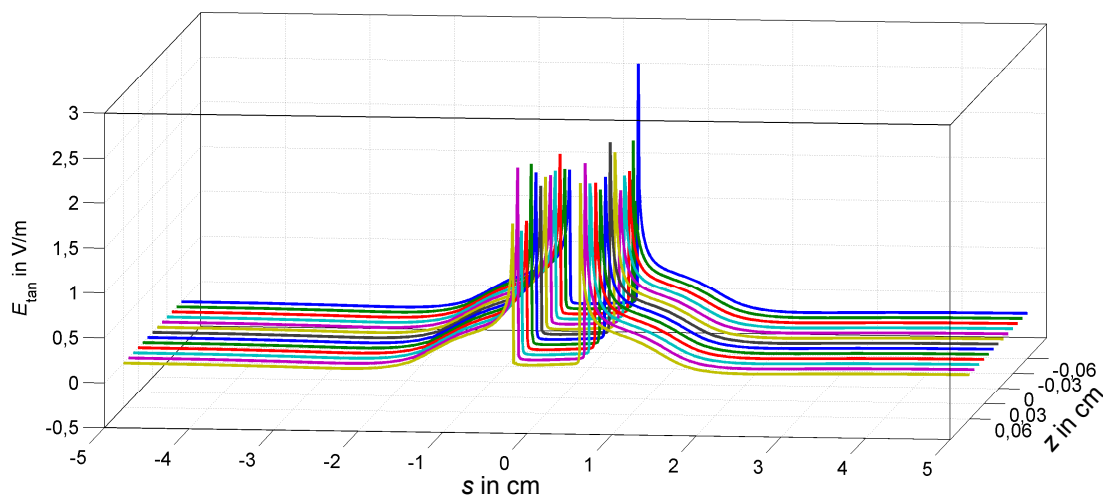


Figure 8.10: Distribution of the tangential electric field strength along the twelve curves in the xz plane

The reason is that the electric field has different values at different z-axis positions. The water drop contour in the xz plane influences the values of the electric field. As the goal is to find the maximum electric field strength at the triple point, the curve with the maximum electric field intensification will be used. The tangential component of the electric field strength is the most affected by the presence of the water drop on the surface. Therefore, the tangential and the absolute electric field strength will be considered.

8.2.2 Global Validation Criterion of the Simulation

In **Chapter 6.1.3** it is shown that the electric field distribution along the insulating surface is theoretically calculated. The objective of this investigation is the analysis of the electric field strength along the insulating surface in the presence of a water drop. In this case, a theoretical calculation of the electric field using the Maxwell's equations is not possible. The arrangement has points on the surface where the three dielectrics meet: air, water and silicone rubber.

These points are named triple points, and are singularity points. Singularity means that the electric field strength in this point tends to infinity. The maximum values of the electric field strength will be found here, and thus the area of interest is exactly

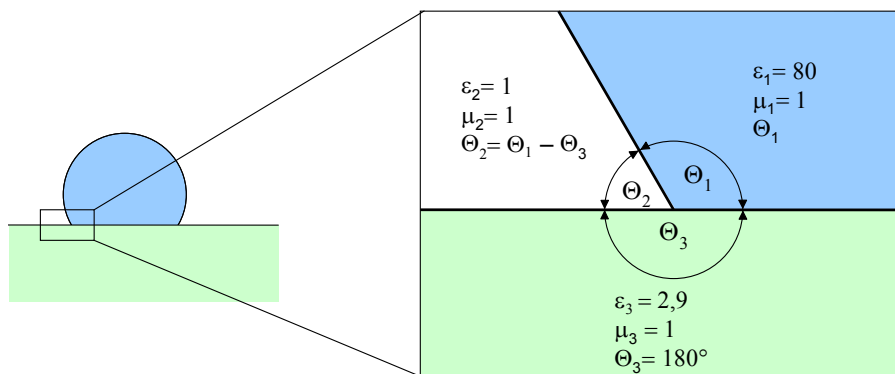


Figure 8.11: Triple point at the water drop

the triple point, whereas the rest of the existing curvature of the water drop can be neglected, as shown in **Figure 8.11**. The angle Θ_2 is obtained as the difference between angle Θ_3 (which is always 180°) and the contact angle Θ_1 of the water drop, here a theoretical case is considered. The electric field distribution along the surface can be expressed by two components [Mei1972]:

$$E_\rho = \sum_{n=0}^{\infty} a_n \rho^{t+n-1} \quad (8.1)$$

$$E_\varphi = \sum_{n=0}^{\infty} b_n \varphi^{t+n-1} \quad (8.2)$$

E_ρ and E_φ are dependent on the distances ρ and φ , the position of the triple point, the singularity exponent t and the factors a_n and b_n . Equations (8.1) and (8.2) are given in cylindrical coordinates. The electric field components are translated in Cartesian coordinates, where only the tangential component of the electric field is considered.

$$M_i = \begin{pmatrix} \cos(t\theta_i) & 0 & \frac{\mu_i \cdot \sin(t\theta_i)}{t\varepsilon_i\mu_i} & 0 \\ 0 & \cos(t\theta_i) & 0 & \frac{\varepsilon_i \cdot \sin(t\theta_i)}{t\varepsilon_i\mu_i} \\ -t\varepsilon_i \cdot \sin(t\theta_i) & 0 & \cos(t\theta_i) & 0 \\ 0 & -t\mu_i \cdot \sin(t\theta_i) & 0 & \cos(t\theta_i) \end{pmatrix} \quad (8.3)$$

For the three dielectrics (water, air and silicone rubber), all of them meeting in the triple point, a material matrix for each dielectric can be written as (8.3). The condition necessary for a non trivial solution of singularity factor t is:

$$\det[m(t) - I] = 0 \quad (8.4)$$

$$m(t) = \prod_{i=1}^3 M_i \quad (8.5)$$

where I is the (4 x 4) unity matrix. By inserting the material parameters and the corresponding contact angle in equation (8.3), the singularity exponent t is calculated as a function of the contact angle θ_i , using equations (8.4) and (8.5).

In **Figure 8.12** the variation of the singularity exponent with the contact angle shows that t has the minimum at a contact angle of (30...40)°, and the values to the left and to the right increase. The singularity coefficient takes values below 1. As can be seen from equation (8.1) and (8.2), only the summand for $n = 0$ will converge to infinity. All the other summands close to the triple point converge to zero. As only the electric field in direct vicinity of the triple point is of interest, only the coefficient a_0 is considered.

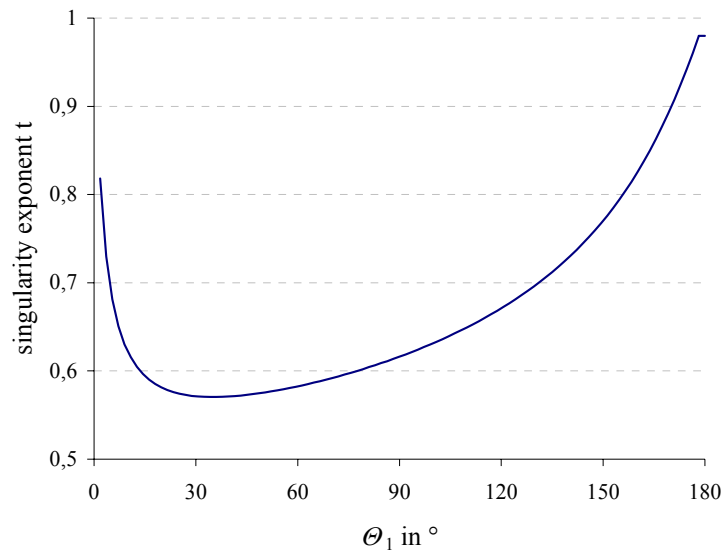


Figure 8.12: Singularity exponent as a function of contact angle

The electric field distributions along the given path for the case of the specimen with water drop and the case of a specimen without drop are subtracted. The resulting curve borders two areas: one area of field enhancement (blue area in **Figure 8.13**) from the triple point to the right and one area of field attenuation (dashed area) left from the triple point.

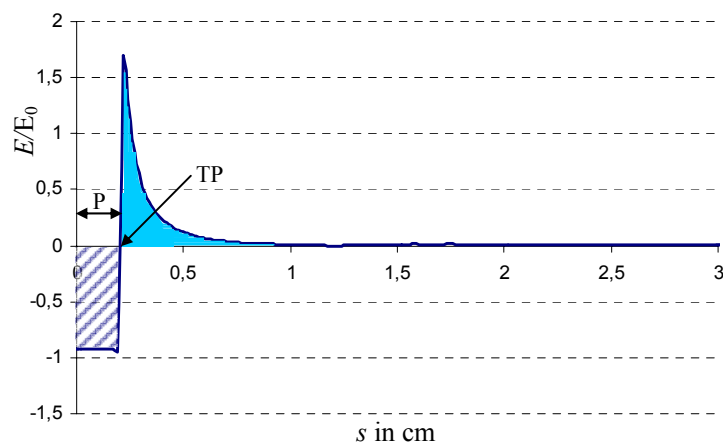


Figure 8.13: Difference of the electric field distribution with drop and without drop, with the area identification

Due to the axis symmetry regarding the y-axis, only the positive part of the x-axis from zero to infinity is presented. In order to calculate the coefficient a_0 , the following assumption is made: the integral from the centre of the drop to the triple point should be the same as the integral from the triple point to infinity. The integral from the axis origin to the triple point describes a rectangular area A_1 , which can be expressed as:

$$A_1 = E_{\text{dif}} \cdot P \quad (8.6)$$

where P is the distance from the centre to the triple point. E_{dif} is the difference between the electric field strength with the distilled water drop and the electric field without water drop on the insulating surface and is expressed as:

$$E_{\text{dif}} = E_t(x, y) \cdot \left(1 - \frac{\varepsilon_w - \varepsilon_a}{\varepsilon_w} \right) \quad (8.7)$$

The area from the triple point to infinity can be calculated as:

$$A_2 = \int_0^{\infty} a_0 \cdot \rho^{t-1} \cdot a^{-\rho} d\rho \quad (8.8)$$

where $a^{-\rho}$ is the function describing the steepness of the electric field distribution and a_0 is an empirical constant. The integral (8.8) cannot be solved analytically. Therefore, a mathematical reformulation is required. The gamma function fits very well with the expression (8.8), and thus the area A_2 can be written:

$$A_2 = a_0 \cdot \frac{\Gamma(t)}{(\ln(a))^t} \quad (8.9)$$

The values of the gamma function are calculated using MatLab software [MATLAB]. Considering the condition that A_1 and A_2 should be equal, the coefficient a_0 is calculated as follows:

$$a_0 = \frac{(\ln(a))^t \cdot E_T \cdot P}{\Gamma(t)} \quad (8.10)$$

Based on these parameters, the electric field strength in the direct vicinity of the triple point can be calculated.

Considering a configuration with a water drop having a volume of 40 μl , a contact angle of 120° and an applied voltage of 1 kV, the electric field distribution along the surface is calculated. The parameters t , P are taken from **Figure 8.12** and **Figure 8.13**. a_0 , a are empirically obtained and the values are given in **Table 8.1**:

Table 8.1: Parameters used for the electric field calculation along the surface for water drop with a contact angle of 120°

T	P	a_0	a
0,67	0,19	15200	240

The comparison of the calculated and the simulated electric field distribution is presented in **Figure 8.14**. As can be seen, the calculated and the simulated electric field values are very similar, especially directly at the water drop. The similarity of the calculated and simulated results means that the results of the simulation are correct. Moreover, the consideration that the integral of the electric field E_{dif} along the surface converge to zero is a good method to verify the electric field values obtained from simulation.

For deformed water drops the analytical calculation of the electric field distribution along the surface is not possible. Only simulation results are available. Using the assumption that the integral of the difference between the electric field values with water drop and without water drop along the surface converge to zero, the accuracy of the simulation results is checked. As it is used to verify the simulation results along the

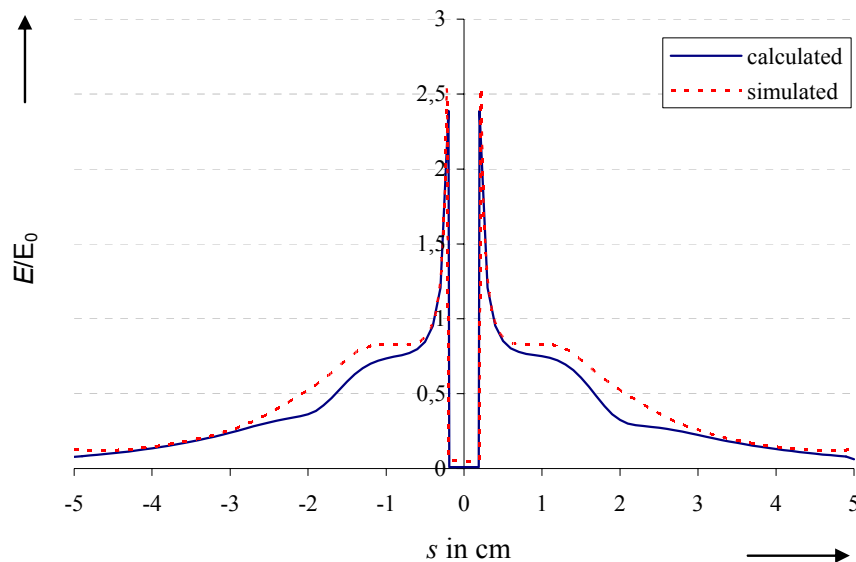


Figure 8.14: Comparison between simulated and calculated field enhancement at the water drop

complete path this validation criterion is named “global criterion”, and it is used to verify further simulations results regarding the electric field intensification in the region of TP.

8.2.3 Local Validation Criterion of the Simulation

The values of the electric field strength obtained from the simulation in the triple points can not be considered by analyzing the electric field enhancement and the necessary conditions to fulfil partial discharge inception requirements, respectively. The reason is the singularity effect. At the junction of materials with different permittivity the electric field vector becomes infinite, as demonstrated mathematically by [Oly1994]. The order

of this singularity is subjected to the so-called edge condition [Bou1946], [Mei1949]. The edge condition states that the electrical energy density must be integrable over any finite domain even if this domain contains singularities [Yeo2006]. For this reason the simulation software is able to calculate a value of the electric field in the triple point. But point field values along the contact line do not converge numerically and therefore cannot be used for analyzing any physical phenomena (partial discharge ignition) in this point.

Therefore, the convergence of the curve in the direct vicinity of the triple point is analyzed. Considering the arrangement presented in **Figure 8.9**, three different mesh resolutions are used. For the calculation the mesh settings of the arrangement is crucial. For each new set of mesh settings, the geometry will be rebuilt. Consequently, for the calculation, each new mesh setup represents a new independent arrangement.

The electric field distribution for a drop having a contact angle of 120° is presented in **Figure 8.15**. The same drop is used in **Chapter 8.2.2** for theoretical calculation. The

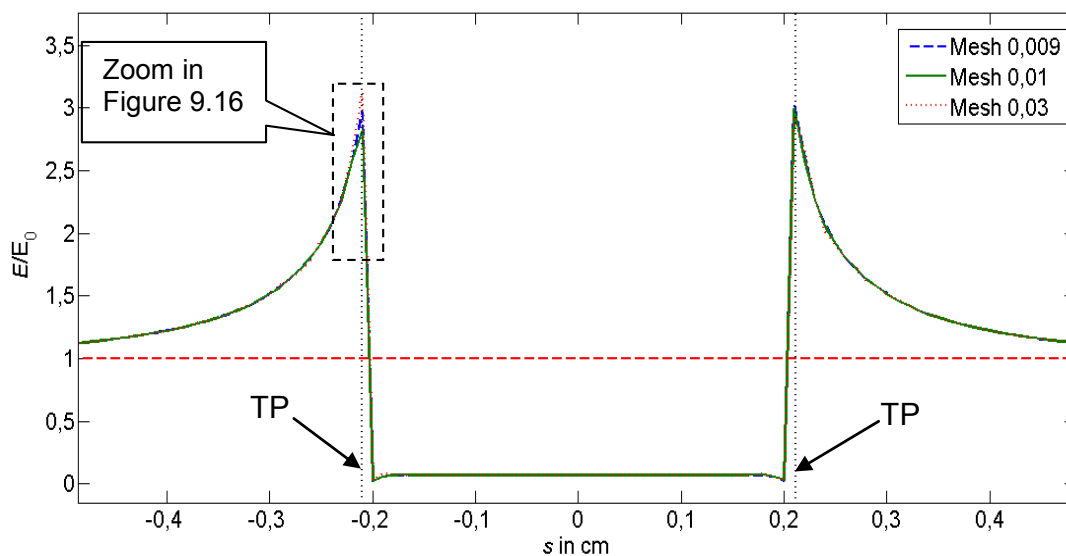


Figure 8.15: Electric field enhancement along the given path for a water drop with contact angle of 120° , using three different relative mesh steps

depicted values of the electric field strength are values relative to the amount of electric field E_0 when no drop is present on the insulating surface. The presented curves correspond to three different relative mesh steps of 0,03, 0,01 and 0,009.

The vertical dashed lines represent the triple points (TP) of the water drop. As the area of interest is the TP zone, **Figure 8.16** presents in detail the three curves for the three mesh steps in the vicinity of the TP. The three curves converge up to a distance of 0,2

mm from the TP. Moreover, the finer meshes converge at an even closer distance (0,1 mm) of the TP. Thus, the point where fine and very fine mesh converge is named converge point (CP).

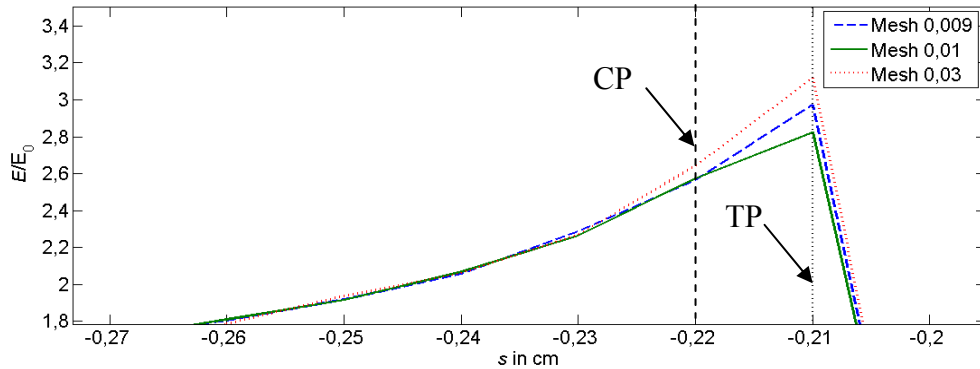


Figure 8.16: Electric field enhancement for undeformed water drop, zoom of the marked area in Figure 8.15

The mesh refinement to steps smaller than 0,009 is limited by the hardware resources. For the mesh step 0,009, 600 000 mesh units were used on a high-performance computer. Theoretically, by using far more mesh cells the CP can also become smaller than 0,1 mm from the TP. On the other hand, a distance of 0,1 mm from the TP is a realistic distance for ionization areas. In this work CP at 0,1 mm (on the x-axis) from TP was considered.

Due to the fact that the TP is a singular point, see **Chapter 8.2.2**, CP will be considered as a reference for local electric field enhancement analysis. As the CP is used only locally (near the TP) this criterion will be named “local validation criterion”. Thus, the accuracy of the simulation results will be verified first by using the “global validation criterion” and then the “local validation criterion”.

8.2.4 Electric Field Enhancement at Undeformed Water Drops

As the silicone rubber surface is hydrophobic and the contact angle of a drop placed on a hydrophobic surface is about 120° , three different ideal water drops were simulated. Using the global and local validation criterion the accuracy of the simulation results is verified. In **Figure 8.17** the electric field enhancement at the three undeformed water drops is presented. First, as reference, a sphere drop is considered then a water drop having a contact angle of 120° and a hemisphere drop. Due to the water drop’s symmetry only one side of the water drop is considered, one maximum value, respectively. The values are relative values with respect to the electric field distribution

without the drop on the insulating surface and are considered as CP. When an ideal sphere water drop is considered, first the contact area between the water and silicone rubber is very small and the contact angle is almost 180° . The local electric field intensification factor is 1,9. At a water drop having a contact angle of 120° the maximum electric field intensification factor is 2,3. The analytical calculation from **Chapter 8.2.2** provides the same values as for the maximum electric field enhancement on the insulating surface. By decreasing the contact angle to 90° (hemispheric drop) the local electric field intensification increases to a factor of 2,5. In

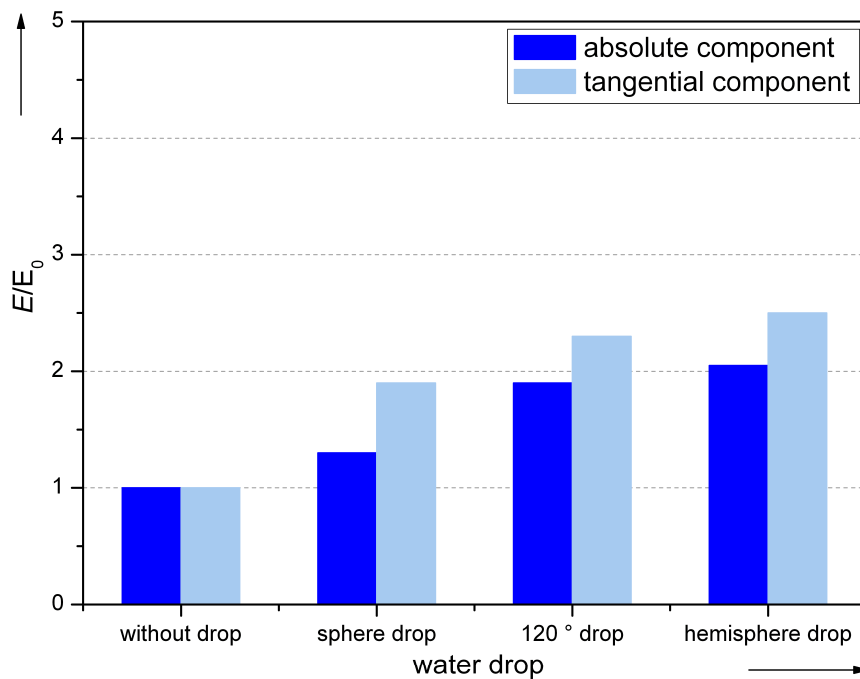
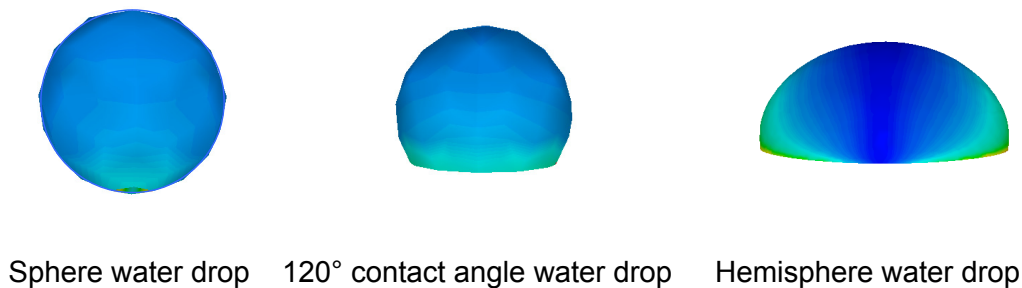


Figure 8.17: Maximum electric field enhancement at undeformed water drops

[Gua2005], [Che2003] a hemisphere water drop is considered and maximum electric field strength intensification in the TP is about 2,5. By comparing the results at a distance of 0,1 mm from TP, the values are smaller in the literature than in this work. But as the TP is a singular point, the value of the electric field strength in TP cannot be considered. The literature always considers the value of the electric field strength in the TP.

The tangential component and the absolute electric field strength are presented. It has been shown that just the presence of undeformed water drops on the insulating surface produces local electric field intensifications. Moreover, the electric field intensification is up to 2,5 when decreasing the contact angle from 180° to 90° . For contact angles smaller than 90° even higher electric field intensifications would be expected.

8.2.5 Electric Field Enhancement at Modelled Water Drops

The deformation of the drop plays an important role in local electric field intensifications at water drops on an insulating surface and a detailed analysis of the deformed drop is necessary.

As presented in **Chapter 8.2.3**, the maximum values of the electric field strength exactly at the triple points cannot be considered. Therefore, the maximum value at a distance of 0,1 mm from the TP is taken. In these points, the numerical values converge. This value is used to quantify the local electric field intensification at the water drops. The electric field values are given in relative values with respect to E_0 , the electric field along the surface when no water drop is present on the surface. The electric field values are analyzed on the right and left side of the water drop.

40 μ l Water Drop

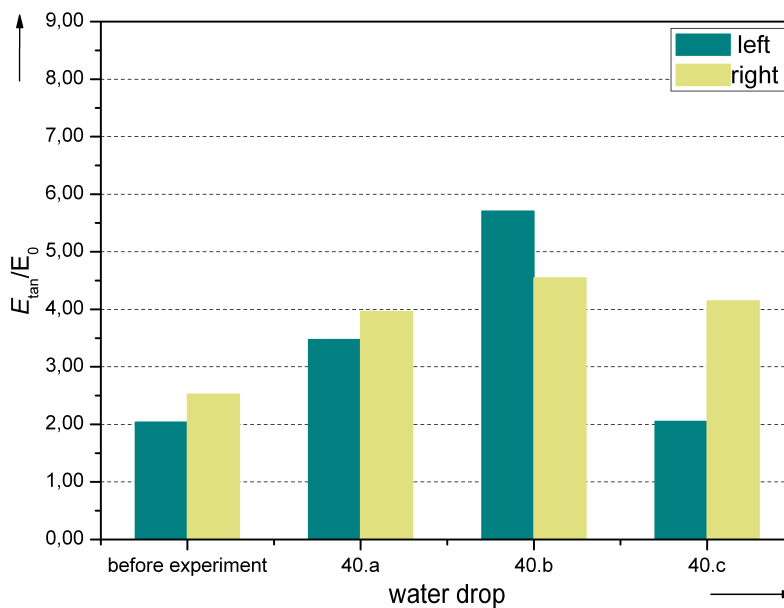
For the 40 μ l modelled drop, the maximum electric field at the CP on the left and right side are presented. The maximum values of the tangential electric field are plotted in **Figure 8.18**.

The first remark is: the tangential component of the electric field enhancement is remarkably higher at the deformed drop than at the drop shape before voltage application. For the drop before measurement, the electric field intensification is up to two or three times higher than the applied electric field strength. The models 40.a, 40.b. and 40.c exhibit local electric field intensifications up to around 6 times higher than E_0 .

The maximum electric field strength, $5,65 E_0$ shows the left side of the 40.b drop, where the shape of the drop is very sharp. The contact angle value is constant almost up to the top of the drop. Although the 40.c model has the same top view as 40.b and the left contact angle is even smaller, the tangential electric field strength is much smaller.

Table 8.2: 40 μl water drop models

Water drop View	Before experiment	40.a	40.b	40.c
Front				
Top				
Side (left)				

Figure 8.18: Maximum tangential electric field intensification at CP for 40 μl drop model

Thus, at the deformed drop the tangential component of the electric field strength depends not only on the contact angle but also on the curvature of the drop near the contact point. In **Figure 8.19** the absolute component of the electric field strength in the region of triple point is presented. Due to the fact that the tangential component is mostly affected by the water drop deformation at the insulating surface, the absolute component values in the CP are similar for all 3 drop models. The values are about 6 times higher than E_0 for deformed drops and about 3 for the water drop model before the experiment. The absolute component of the electric field strength plays the main role in the streamer inception.

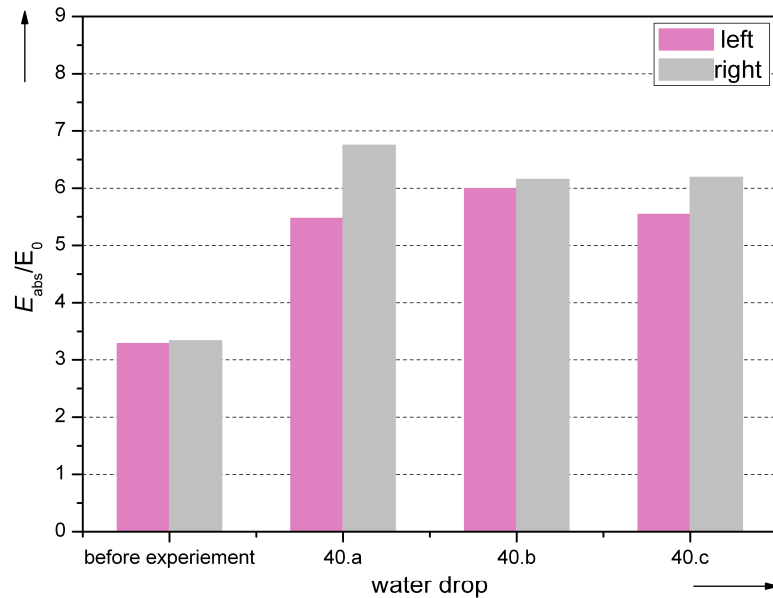


Figure 8.19: Maximum absolute electric field intensification at CP for 40 µl drop model

At an applied electric field $E_0 = 6,1$ kV/cm, which is the inception field strength at the standard atmospheric conditions, the local electric field intensifications are presented in **Figure 8.26**. The maximum absolute electric field values near the TP are between 27,75 and 33,15 kV/cm for the 40 µl water drop. Considering that the partial discharge inception electric field strength in air at normal atmospheric conditions, depending on the electrodes geometry, has the minimum value of 25 kV/cm, the values of the electric field strength values in the near of the TP are sufficient for partial discharge inception. This statement is a very important tool for the future simulation work in order to verify if the inception conditions are fulfilled or not.

All 40 µl deformed water drops show higher electric field intensification near the triple point than the undeformed water drop and will favour the partial discharge inception requirements. For the three deformed models, the variation of the tangential component of the electric field strength is higher than that of the absolute component of the electric field strength.

60 µl Water Drop





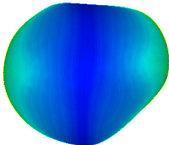
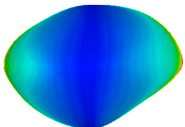
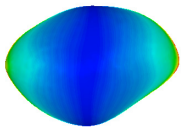
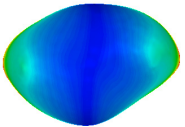
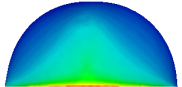
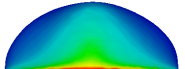
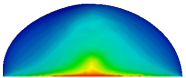
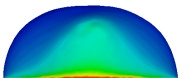
The 60 µl deformed water drop is modelled and simulated. Electric field intensifications are analyzed near the triple point,. The maximum values of the tangential component of the electric field in the CP are presented in **Figure 8.20**. The water drop shape before the experiment shows a high tangential electric field intensification on the left side, which is 4,2 times higher than the electric field without the drop. This intensification is

caused by the shape of the water drop. The top view shows that the form of the water drop is not perfectly round. For the models 60.a, 60.b and 60.c the local tangential component is relative value and is in the range 4,5 – 5,5 times higher than E_0 . Also the differences between the left and right side of the drop are smaller than those at the 40 μl drop. Here the 60 μl water drops are deformed according to pattern 2 from **Chapter 7.1.1**.

The local tangential field intensification on the left side of the drop, before the experiment, persists also for the three deformed drops. Thus the initial shape of the drop before voltage application plays a main role in the electric field intensifications at the deformed water drops. But the tangential values for the 60 μl drop are smaller than those measured for the 40 μl deformed drops. Although model 60.c presents a sharp edge at the top of the shape, the highest values of the electric field strength are not at that point. Consequently, the sharp edges affect the values of the electric field strength only when they are near the TP. The absolute components of the electric field strength, for the 60 μl models, are presented in **Figure 8.21**.

Also in this diagram the water drop model before the experiment shows a high electric field enhancement on the left side. As the tangential component on this side is also higher on the left side the reason can be attributed to the shape of the drop near TP.

Table 8.3: 60 μl water drop models

Water drop View	Before experiment	60.a	60.b	60.c
Front				
Top				
Side (left)				

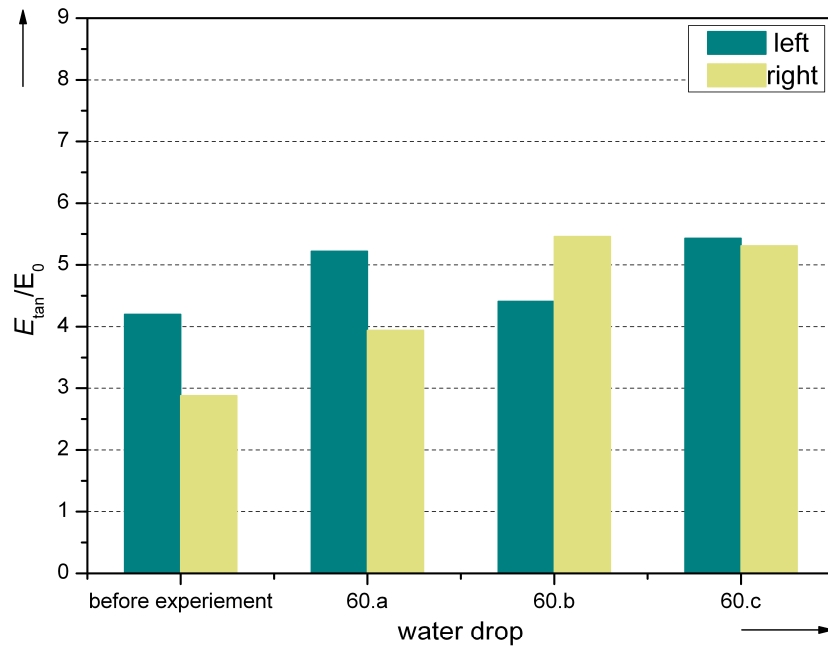


Figure 8.20: Maximum tangential electric field intensification at CP for 60 μ l drop model

The absolute values for the three models are between 5,5 to 6,8 times E_0 on both the left side and right side. The variation of the absolute electric field strength between the left and right side as well as between the models is relatively small.

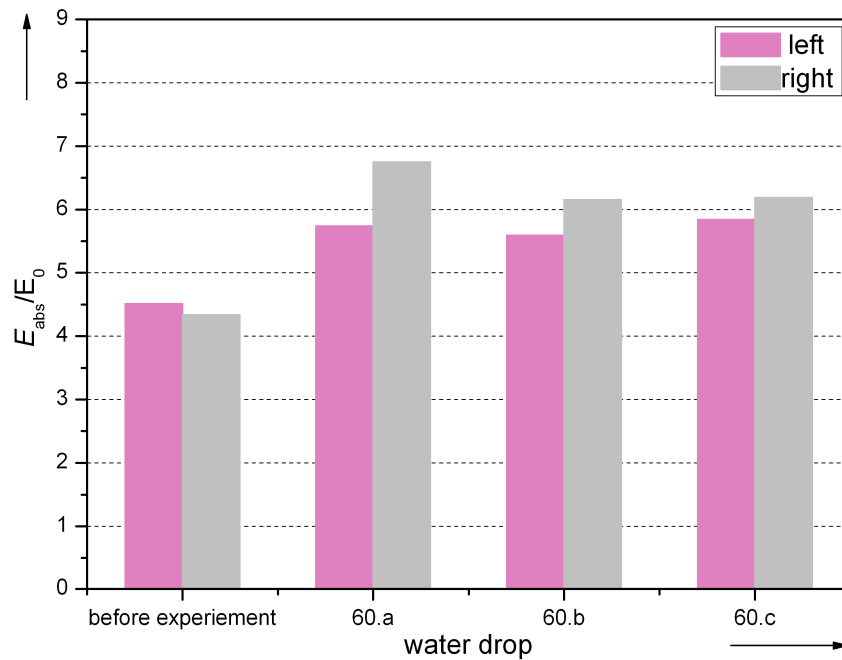


Figure 8.21: Maximum absolute electric field intensification at CP for 60 μ l drop model

In comparison with the 40 μ l water drop, the 60 μ l water drop shows smaller tangential field intensifications in the region of the triple point. For the absolute component, values

of the electric field are contrary; the values for the 60 μl water drop are slightly higher than those measured for the 40 μl water drop. Also the difference between the tangential and absolute values of the electric field is smaller than the values measured for previous water drop volumes.

The expected dependence of the electric field intensifications on the water drop volume cannot be observed due to the particular models. Each drop model is a single state of one recording sequence. The complete different deformation pattern of the 40 μl and 60 μl water drop provides an explanation for the different electric field intensifications. Due to the shape of the 60 μl water drop, before experiment, the normal component of the electric field at the insulating surface is higher than that of the 40 μl before the experiment.

Considering an applied electric field of $E_0=5,6$ kV/cm, corrected at standard atmospheric conditions, the absolute electric field values at the TP area are between 26,9 kV/cm and 31,8 kV/cm. Even through the 40 μl and 60 μl models have different deformation patterns, the values are reaching here at least the minimum inception electric field strength in air at normal conditions.

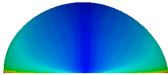

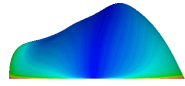
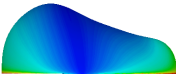
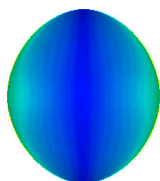
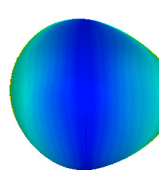
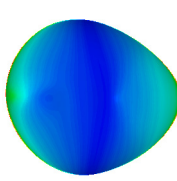
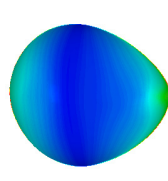
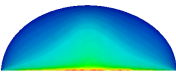
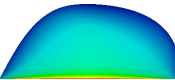
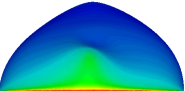

80 μl Water Drop

The simulations for the 80 μl water drop models are carried out using the same settings as for the previous water drops. The tangential component of the electric field presents intensifications of 2,6 higher than those of E_0 on the left side for the undeformed drop and up to 3 or 4 times for the deformed water drops, see **Figure 8.22**. On the right side in the CP the electric field intensifications are definitely higher, between 5 and 8. The reason for the high tangential electric field intensifications on the right side of the drop is the shape of the drop on that side; see top view from **Table 8.4**. Also the contact angle on the right side is much smaller than on the left side. A comparison of the results for 40 μl models with 80 μl models reveals that both present a high variation of the electric field strength values on the left and right side of the drop. The reason is that they have the same deformation pattern. Also here, the maximum tangential electric field strength occurs at the TP area and not at the tip of the water drop model.

Upon analysis of the absolute component of the electric field near the TP, the same pattern can be recognized, see **Figure 8.23**. On the left side, the absolute values of the electric field intensifications are about factor 4 and there are no substantial differences between the undeformed and deformed models.

On the right side, the electric field intensifications are much higher in comparison with those on the left side and for the deformed models by about factor 8. From all analyzed models the 80 μl models have the highest electric field strength intensification.

Table 8.4: 80 μl water drop models

Water drop View	Before experiment	80.a	80.b	80.c
Front				
Top				
Side (left)				

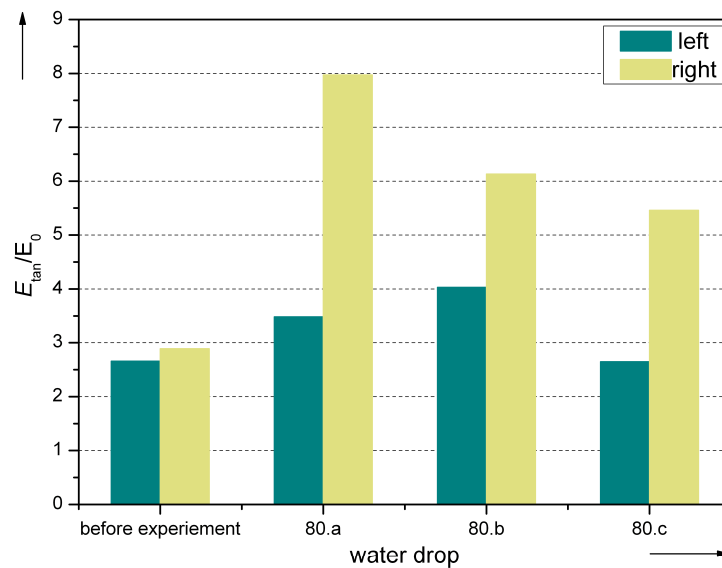


Figure 8.22: Maximum tangential electric field intensification at CP for 80 μl drop model

The small right contact angle and the sharp curvature on the right side are responsible for the large difference between the values of the absolute electric field strength on left and right side of the drop. The drop model 80.a and 80.b exhibit the highest electric field intensification, namely 8,5 times higher than the applied electric field.

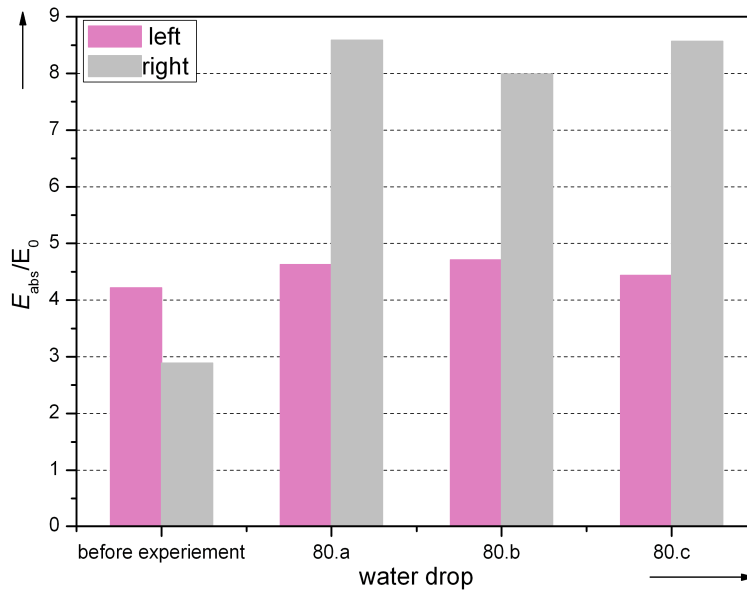


Figure 8.23: Maximum absolute electric field intensification at CP for 80 µl drop model

At the standard atmospheric condition the applied electric field stress is $E_0 = 5,2$ kV/cm. The absolute values of the electric field values are between 17,85 kV/cm and 36,3 kV/cm. In this case the variation interval is in the same range but is more expanded than for the other two volumes. The reason for the expanded range is the greater variation between the right and left side of the water drop model.

8.2.6 Comparison between the Different Water Drops

The local tangential electric field intensifications for nine different water drop deformations at three different volumes are presented in **Figure 8.24**. The water drop deformations, caused by the hydrodynamic forces, obviously influence the electric field distribution along the insulating surface. The local electric field intensifications for all deformations are above 2,5 times higher than the applied electric field. For frame 40.b and 80.a the electric field strength increases at the TP zone up to factor 8. The 40 µl and 80 µl models show both high variations of the tangential electric field strength on the left and right side of the drop, while the 60 µl models do not vary. Thus, the water drop deformations according to pattern 1 from **Chapter 7.1.1** present higher electric field strength intensifications and the requirement for partial discharge inception will be fulfilled earlier. Deformations according to pattern 2, i.e. 60 µl models, exhibit almost the same electric field intensifications on both sides and the values are much lower.

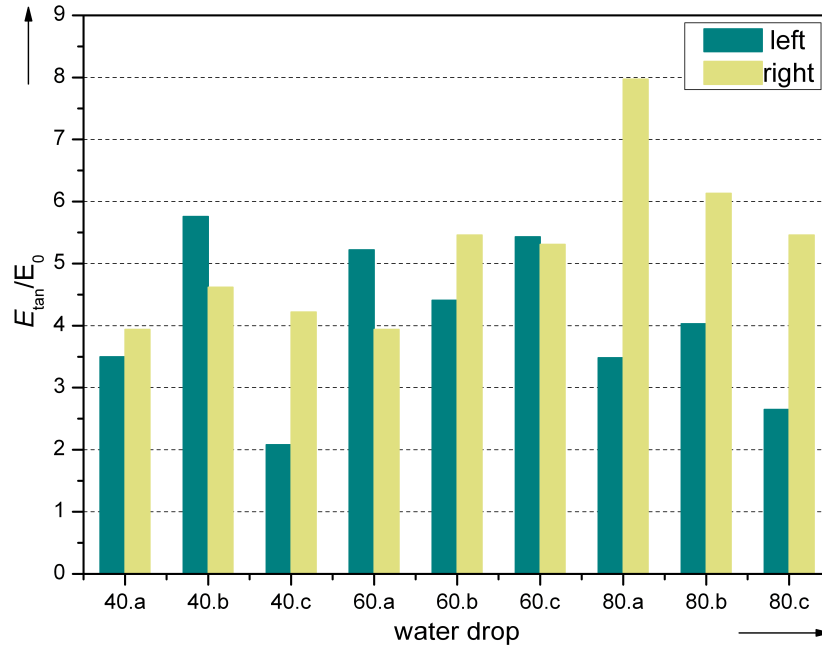


Figure 8.24: Maximum tangential electric field intensification at different water drop models

At the same partial discharge inception electric field strength, the discharge activity of the 60 μl models is much smaller than that of the 40 μl and 80 μl . Thus, the ageing processes are slower and the longevity of the insulating material is higher.

The 80 μl water drop exhibits the highest difference between the left and right side of electric field intensification. The reason is asymmetrical curvature of the water drop, as presented in **Chapter 8.2.5**.

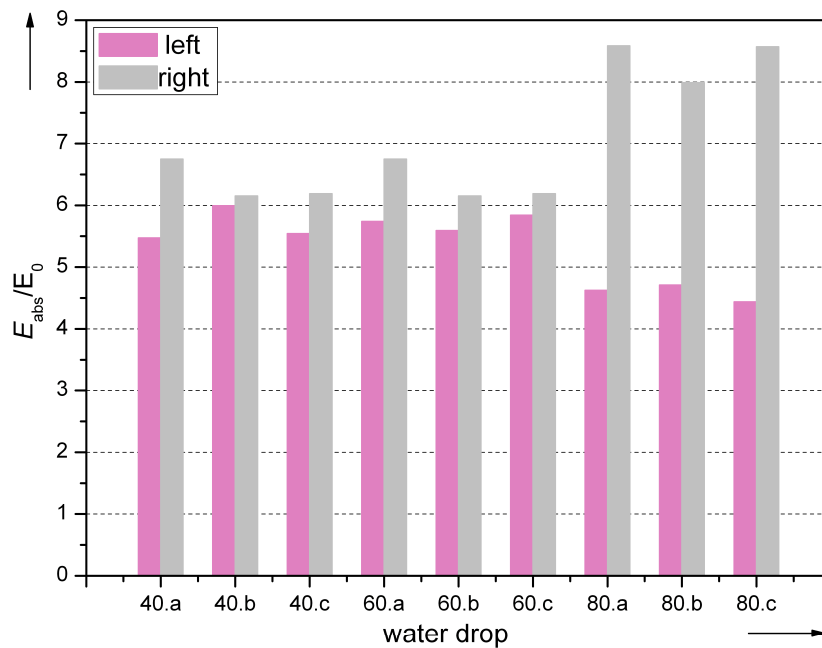


Figure 8.25: Maximum absolute electric field intensification at different water drop models

In comparison with the tangential component of the electric field strength, the absolute values at the CP are presented in **Figure 8.25**. The 40 μl and 60 μl water drops present similar electric field intensifications on both sides and are about 5-6 times higher than the absolute electric field strength when no drop is present on the surface. For the 80 μl water drop, the absolute electric field is up to 8,5 times higher than E_0 and the difference between the left and right side of the drop is significantly high. The reason for higher electric field intensifications is the sharp curvature on the right side of the water drop, see **Chapter 8.1.3**.

By considering only the values of the absolute electric field strength it is observed that the 40 μl and 60 μl water drop have the same behaviour with the exception of the 80 μl water drop. But if the mean value per drop is considered, all water drops present local field intensifications of about factor 6.

As the intensification of the absolute component of the electric field strength is the significant parameter for the inception electric field, the maximum local absolute values are calculated. The applied electric field strength E_0 is considered for each drop volume. The values of the absolute values occurring at the TP area of the water drops are presented in **Figure 8.26**. Also in this case, the 40 μl and 60 μl water drop models exhibit local electric field values between 25 kV/cm and 30 kV/cm, while the 80 μl has a minimum of 18 kV/cm and a maximum of 36 kV/cm. All the models achieved at least on

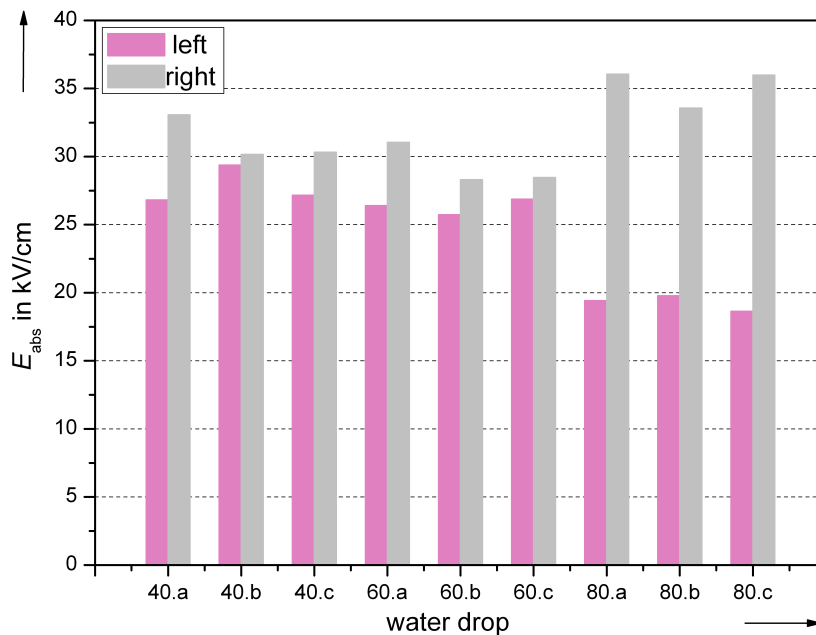


Figure 8.26: The absolute local electric field intensifications at different water drop models

one side of the drop the minimum value 25 kV/cm, which is the minimum inception electric field strength in air at normal conditions. For the 40 μl and 60 μl water drop the partial discharges start on both sides of the drop while for the 80 μl model only on the right side of the water drop. It can be concluded that as soon as the local electric field strength at the water drops reached at least the value 25 kV/cm the inception conditions are fulfilled. This observation can be used for further simulations, e.g., when the absolute electric field value is above 25 kV/cm at the TP area of the water drop, means that the minimum requirements for discharge are fulfilled.

Figure 8.27 presents an overview of the electric field intensifications at the triple points of different water drop shapes. Starting from the ideal sphere water drop up to deformed water drops, the tangential and the absolute component of the maximum electric field strength is increasing. As for the ideal sphere drop, the local field intensifications are 1,7 times higher than those of the electric field when no water drop is present. For the deformed water drops the electric field intensifications are 7 times higher. For the deformed drop a mean value for E_{tan} and E_{abs} is considered.

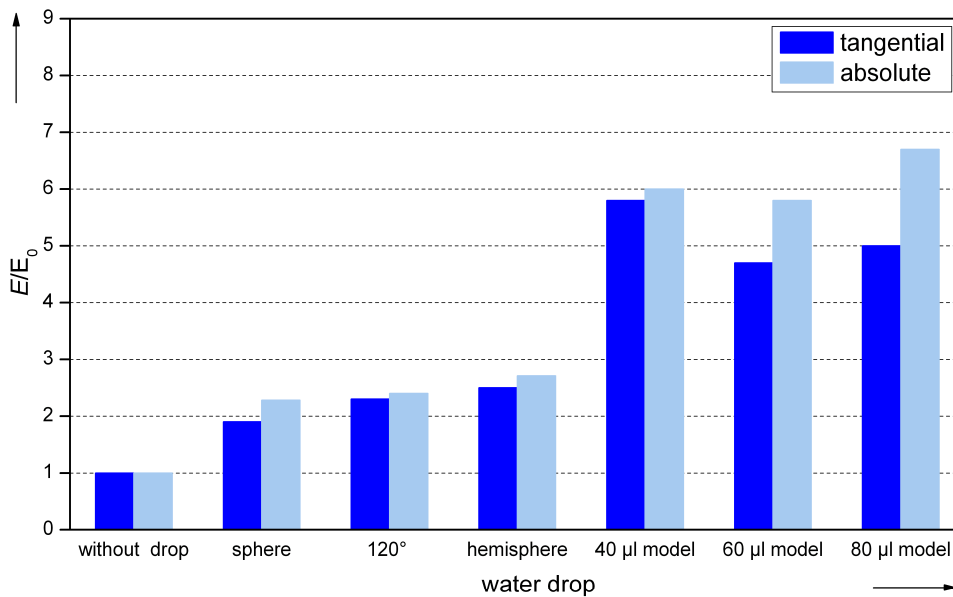


Figure 8.27: Maximum electric field intensification at different water drops

The deformation of the drop is the most important parameter which must be considered by analyzing the electric field distribution along the insulating surface in the presence of water drops. Moreover, the contact angle and the curvature of the water drop shape are responsible for intensifications of the tangential component of the electric field strength. However, the partial discharge inception conditions at water drops are influenced by the absolute component of the electric field strength.

Due to the fact that the differences between the values of the electric field strength of undeformed and deformed water drops are high, the deformation of the water drop under electric field stress cannot be neglected and must be considered.

9 Discussion, Conclusions and Outlook

9.1 Water Drops under the Electric Field Stress

On a horizontal insulating surface, the geometrical form of the water drop is defined by the surface properties and the fluid characteristics. The shape of the water drop is governed by the surface tension: the smaller the surface tension, the smaller the surface of the drop. Therefore, the same fluid will form almost sphere drops on a hydrophobic surface and ellipsoid shape on hydrophilic surface.

When an alternating electric field is present, the water drop starts to present waves on the surface. By increasing the electric field above a critical value, the water drop holds its equilibrium position but starts to oscillate in the direction of the electric field and a characteristic movement can be recognized. The same effect can be observed by ferrofluids stressed by an external magnetic field [Kei2003], [Eng1999], [Lan2000].

The experimental measurements reveal that the deformations depend on the applied voltage and its frequency, drop volume and ambient conditions. The water drop deformations are repeated in one voltage period as well as in the sequenced periods. The motion of the water drops is in accordance with the frequency at low frequencies and exhibits low amplitude movements at high frequencies [Kei2003]. Upon direct field stress the water drop is stable up to a critical value when the water drop moves only once. After the movement, the water drop oscillates several times due to inertia. Hence, the water drop movements during alternating field stress are due to the oscillations caused by the frequency.

In the presence of the electric field, the electrodynamic forces have the effect of stretching the water drop in the direction of the electric field lines. The most affected part is the TP of the water drop in the direction of the electric field. These forces elongate the water drop and are compensated by the viscosity of the fluid and by the interface friction forces between the water and the insulating surface. The previous remarks are observed during the experimental measurements and proved by electric field simulations.

The observed deformations of the water drop can be recognized by different water drop volumes. Due to the technical constrains, water drops with volume smaller than 40 μl are not analyzed in this work. The 40 μl and 80 μl water drops show similar deformation but the 60 μl water drop has a completely different behaviour on the

polymeric surface under electric field stress. The deformations depend on the initial conditions: smoothness of the drop, position of the pipette when the water drop is placed and surface state. The deformations of the drop with respect to the frequency are analyzed in [Schü1990]. For power frequency, 50 Hz, the results obtained in this work are in agreement with the published literature.

The ambient conditions show a different influence on the inception voltage at water drops on a polymeric surface than the influence at the breakdown voltage: the inception electric field strength decreases by increasing the absolute humidity of the ambient air. There are three at least two different possible explanations for this behaviour. First, looking from the microscopic point of view, the large negative oxygen ions could be obtained by the clustering/declustering process and the negative ion production increases exponentially with the humidity in the presence of the electric field. Due to the high concentration of negative ions the probability that the avalanche formation requirements are fulfilled is higher at high humidities, and this is the explanation for the dependence of the inception electric field strength with the absolute humidity presented in this work. From the macroscopic point of view, other two explanations can be given: at high humidities the contact angles of the water drop shapes could be changed or due to the evaporation the water drop shapes and volume could be changed. The last two aspects are not analyzed in this work and it can be researched in future work.

The electric field intensifications at the insulating surface are determined by the water drop deformation. The recorded water drop deformations are modelled using a design software. The distribution of the electric field along the deformation models is obtained using an electrostatic solver. As the TP is a singularity point, the electric field tends towards infinity, the electric field distribution in the vicinity of the TP must be considered. At a distance of 0,1 mm from the TP, at CP electric field intensifications up to 8 times higher than the electric field without drop are observed.

When the electric field distribution along a wet insulator is analyzed, it is absolutely necessary to consider the deformation of the drop.

The practical measurement and simulation results show that the shape of the water drop is very important for electric field analysis and that the deformation of the drop must be considered. In order to compare experimental measurements with the simulation values, they must be adjusted based on the ambient condition factor.

9.2 Ageing Model Update

At the insulating surface two different physical mechanisms which lead to insulation bridge can be observed. One is the electro-hydro-dynamic process and the second one its own effect, the discharge appearance. Both can lead to flashover [Che1974].

With regard to the early ageing processes at polymeric surfaces, the electro-hydro-dynamic processes are the most important for the flashover mechanism. In the early ageing phase the discharge appearance is minimal. Electrodynamics processes are present as water drop deformations, wave-like structures on the water drop surface, water drop splitting and formation of new drops. These dynamic events will advantage the formation of the fluid traces on the insulating surface and trigger the ageing mechanism. When the insulating surface is stressed by electric field, even by virgin surfaces, where the surface is still hydrophobic, the ageing mechanisms will start. The experimental results are in accordance with the ageing mechanism presented in the ageing model from **Chapter 3.1**. The surface shape of the drop depends on the frequency and on the applied voltage. The electro-hydro-dynamic phenomena are generally valid for early ageing and late ageing phases, for indoor and outdoor insulation and for the alternating and direct electric field. As the discharge appearance is already the effect of the electro-hydro-dynamic processes, the cause is the only possibility to avoid and limit the ageing processes at the insulating surface.

The electro-hydro-dynamic aspects at singular water drops analyzed in this thesis are relevant for the early ageing phase. In **Figure 9.1** the ageing model is upgraded for the early ageing phase. First the water drop deformation is responsible for the local electric field intensifications. Due to the deformation of the drop, the TP position and the dry distance on the insulating surface change respectively. The second update of the ageing model is the consideration of the ambient conditions. In the presence of the electric field the O_2^- hydrates with the water molecules from air, resulting in the formation of large number of negative ions, which increases exponentially depending on the ambient air humidity. This effect increases the probability of avalanche formation near the water drops. Those points will be the starting points for the PD activity at the surface of the polymeric material.

The general ageing model presented here is valid for all types of water traces present on the insulating surfaces. But individual effects of the complete inception phenomena cannot be generalized. Each effect depends on different parameters such as the type

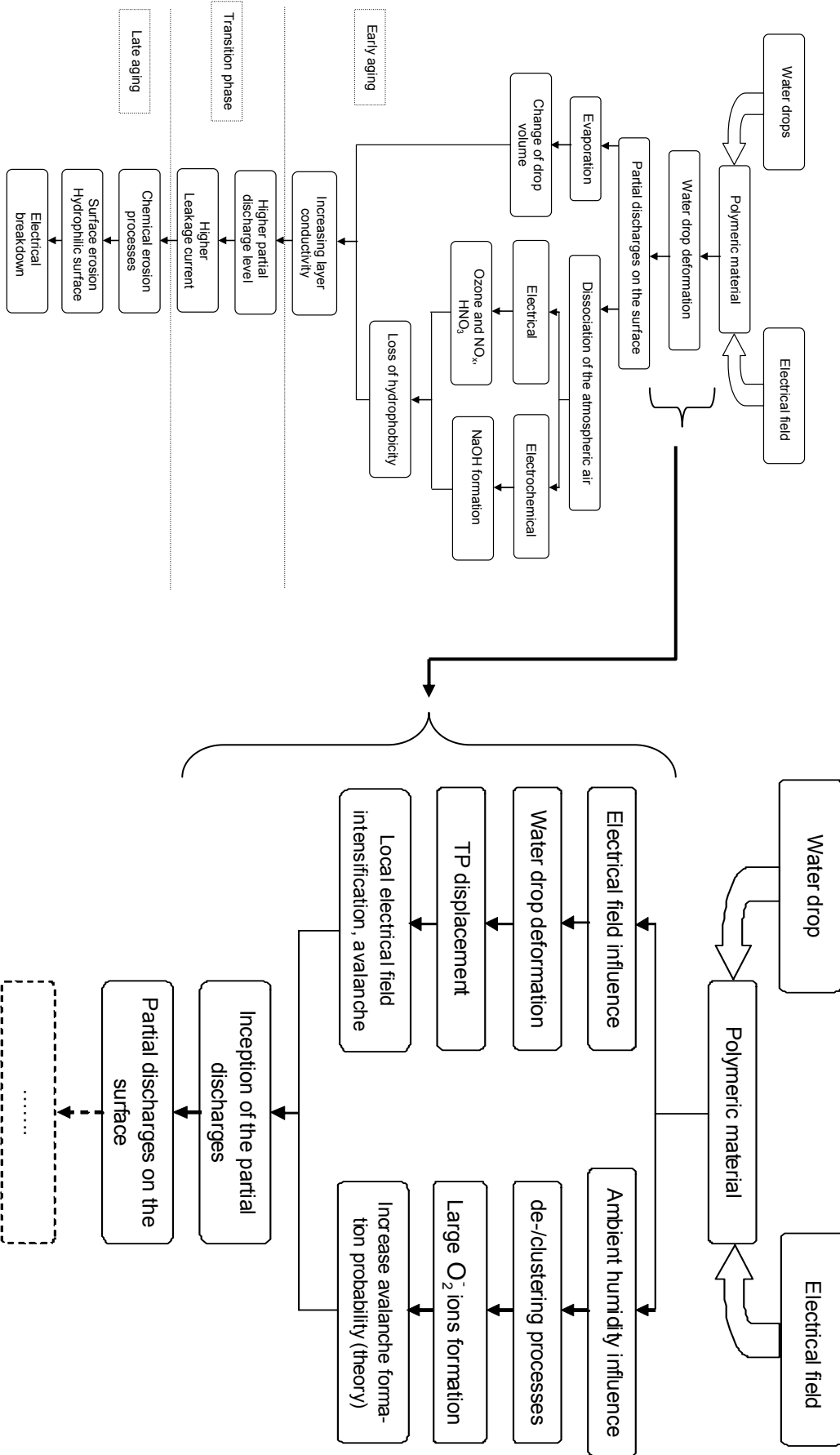


Figure 9.1: Update of the ageing model

of stress, water drop volume, water drop conductivity as well as smoothness of the insulating surface.

9.3 Conclusions

This work presents experimental and simulations results which contribute to a better understanding of the electrodynamic phenomena at the water drop under electric field stress on the insulating surface and their influence on the PD inception conditions.

Under electric field stress on a polymeric surface the water drops deform and form sharp edges. The water drop movement on the insulating surface is recorded using a high speed camera and a mirror system. The mirror system simultaneously records three different plane views of the water drop. In this way, a three dimensional recording is possible, while providing three dimensional information about the water drop movement. The recordings revealed that the water drop deformations are repeated along one voltage shape and two different patterns are observed. Water drops deforming according to pattern 1 present asymmetrical volume displacement on the left and right, while pattern 2 presents a wave-like structure on the surface. The 40 μl and 60 μl water drops deform following pattern 1 and the 60 μl water drop following pattern 2.

The partial discharge activity is analyzed using a standard partial discharge measurement system. As the discharges taking place at one water drop are marginal, the partial discharge system is not sensitive enough to detect the ignition of the discharge. Using a UV camera it was observed that discharges take place on the surface starting from the TP of the drop towards electrodes, at a voltage value below the value at which the partial discharge measurement system records the first discharges. This effect cannot be explained without assuming that the conventional partial discharge measurement system is not sensitive enough to detect the first discharges at water drops. Therefore, a photomultiplier module was used to detect the inception of the discharge activity on the surface. The first light emission of the partial discharges is amplified and converted into an electrical signal. It was revealed that the photomultiplier module detects the first partial discharge at a voltage value which is up to 13 % lower than the value measured using the standard partial discharge system.

During experiments the following parameters varied: water drop volume, water drop conductivity and ambient conditions. The inception electric field strength for small water drops is higher than that for greater water drops. The effect can be explained as

follows: for smaller water drops the intermolecular forces are in equilibrium with the surface tension and therefore the electrical forces required to disturb the equilibrium or to start the water movement are higher. For large water drops, due to the lower inner forces and the same surface tension, the equilibrium is more easily disturbed. Therefore, the partial discharge starts at lower voltages and the inception electric field strength decreases by increasing the water drop volume. Small water drops exhibit higher contact angle than larger water drops. The contact angle increases by decreasing the water drop volume.

The ambient conditions also play an important role in determining the inception electric field strength at water drops and it is a parameter which changes very often in normal duty, especially for outdoor insulation. Looking from the microscopic point of view, at high humidity and in the presence of the electric field, the oxygen molecules hydrate with the water molecules from moist air, forming large negative ions. As the production of large ions increases exponentially by increasing the humidity, the probability of an avalanche starting is higher at higher humidity than at lower ambient humidity. Hence, the inception electric field strength decreases by increasing the absolute humidity. Two different decay rates were measured. From 2 to 13 g/m³, region I, the inception electric field decreases by 2.3 %/g/ m³ and from 13 to 42 g/m³, region II, the decay rate is 0.8 % /g/m³. In region I the increase of the negative ions is faster and therefore the probability of avalanche formation is higher, i.e the decrease of the inception voltage is faster. In region II, the number of negative ions is already high, and upon increase of the humidity the number of negative ions does not change considerably. Thus the probability of avalanche formation increases slowly and the decrease of the inception voltage is slower than in region I, respectively. The humidity correction factors presented in this work can be used to predict exactly the inception electric field at the water drops on an insulating surface at a certain absolute humidity value.

From macroscopic point of view another two explanations for the dependency of the inception field strength with the absolute humidity could be considered, namely, the contact angle of the water drop is changing by different humidity level and that the evaporation of the water drop could influence the inception electric field strength value.

The practical importance is that the ambient conditions, i.e. absolute humidity, influence PD activities reversely compared with the general breakdown electric field strength. The ambient conditions should always be measured when PD measurements are carried out. Long-term observations and measurements on PD activity will only be

of any relevance if the results are obtained under the same humidity conditions or if they are corrected with respect to the humidity level.

The water drop deformations recorded with the high speed camera were modelled using design software, where the shape and volume of the drop are reproduced very accurately. The contour of the water drop deformation is modelled with the help of one curve in each plane view. If the water drop deformation is asymmetrical more than one curve per plane view was used. Based on this frame, a surface and a volume item (deformed water drop) are built, respectively. Using the models and the inception voltage values from the experiments, the electrostatic simulations are carried out. The simulation results show electric field intensification in the region of TP. In order to verify the simulation results, an analytical calculation was carried out. For the undeformed water drop with a contact angle of 120° the theoretical calculations are in agreement with the simulation results. For the deformed water drop the theoretical calculation of the electric field distribution at the water drop is no longer possible. Therefore, the theoretical consideration revealed that criteria to verify the simulation results must be found. Two criteria are developed, one global and one local. If the simulation results fulfil both criteria, the values can be considered to evaluate the electric field intensifications in the region of water drop.

The first criterion, named “integral criterion” is a global validation criterion, e.g. is valid for the whole path along the sample, and can be expressed as: the integral along the curve, which is the difference in each point between the electric field with and without the water drop, should be zero. If this criterion is fulfilled, globally the simulation results are correct. But, the interest point is in the near of the water drop, where the electrical field is intensified using a local validation criterion.

As the TP is a singularity point, i.e. values of the electric field strength tend to infinity, the values in the TP cannot be considered in the evaluation of the electric field intensification. The analysis of the electric field curves along the surface, at a distance of 0,1 mm above the surface at different mesh settings revealed that up to a distance of 0,1 mm from the TP, the curves corresponding to the fine meshes converge and this point is named convergence point. The CP is the point where the electric field intensification is considered. This is the “convergence criterion”, the local validation of the simulations results. The electric field intensification, analyzed at the CP shows high electric field intensification in the presence of the water drop on the surface.

The variation of the electric field strength with the contact angle and with the contour of the drop is shown by measurements and demonstrated by simulations. The electric

field intensification in the TP at hemisphere water drops is up to 2,5 times higher than the electric field values without water drops on the surface. For deformed drops, the electric field intensifications are higher and can reach values eight times higher than E_0 . The water drop deformations following the deformation pattern I (water drop volume is moving forwards and backwards in the direction of the electric field lines) show higher electric field intensification than the water drop deformations according to pattern II (water drop is crossed by a wave-like structure) and illustrate the great difference between the electric field values on the left and right side of the drop. The water drop deformation following pattern II exhibits lower electric field intensification and the values of the tangential electric field on the left and right side of water drop are similar. The tangential component of the electric field is the component affected by the local field intensifications. Taking into account the magnitude of the local electric field intensification, the deformation of the water drops on the insulating surface must be considered by electrical resistance of the polymeric insulating surfaces.

The absolute value of the electric field is to be considered in order to compare the experimental measurements with the simulation results. For the deformed water drops the absolute values of the electric field strength are in the interval 25-36 kV/cm. Since the minimum value of the inception electric field strength in air is reached the minimum requirement for discharge ignition is fulfilled. The measured partial discharge inception voltage, constituting input data for simulation, shows a very good correlation with the simulation results. Comparing the local electric field intensifications with the experimental findings, the ambient conditions factor should be considered.

The ageing model of a polymeric material was upgraded in the region of the early ageing phase. The water drop deformations, their implication on the local electric field intensification and the influence of the ambient conditions on the inception electric field are included in the ageing model for polymeric materials.

All the processes discussed in this thesis lead to a better understanding regarding water drop initiated discharges in air.

9.4 Outlook

In this work, the simulation results were carried out using an electrostatic solver where different water drop deformations were inserted and simulated. With the aid of numerous high-speed camera recordings, an algorithm to recognize and to model automatically the water drop deformations can be developed. Subsequently, different parameters such as surface smoothness, material state, incline angle, pollution grade, etc. can be varied and their dependence can be ascertained. By using a low frequency solver, the deformations of the drop can be coordinated with the voltage period. As in this work the influence of the negative ions aspect, for the influence of the humidity on the inception electric field strength was analyzed, a possible influence of the contact angle and evaporation could be considered in future work.

To date there is no simulation software designed to simultaneously consider the electric stress and the fluids dynamics stress. Therefore, software designed to combine both stresses would be very useful. With this software it would be possible to predict the behaviour of the water drops on an insulating surface at a given electric field stress.

AC stress provides the focal point of the results presented in this work. As the current trend is to use higher voltages for power transportation, DC systems constitute suitable alternative systems. For long distances or for off-shore windparks connections to the DC systems are recommended. Therefore, DC insulation should also be considered and analyzed. The charge accumulation of DC systems will affect the inception partial discharge behaviour and conditions. The water drop deformations, as well as the electric field distribution are different under DC stress.

Standards

- [IEC/TS 62073] IEC/TS 62073-2003; *Guide to the measurement of wettability of insulator surface*; 2003
- [DIN 50035-1] DIN 50035/03.89; *Terms and definitions used on ageing of materials; basic terms and definitions*, 1989
- [IEC 60270] IEC 60270-2000; *High-voltage test techniques – Partial discharge measurements*; 2000
- [IEC 60052] IEC 60052, Ed. 3,; *Voltage measurement by means of standard air gaps*, 10-2002
- [IEC 61621] IEC 61621; Ed. 1 *Dry, solid insulating materials – Resistance test to high voltage, low current arc discharges*; 1997

Literature

- [Abb1969] Abbas, M. A., Latham, J.; *The disintegration and electrification of charged water drops falling in an electric field*; Quart. J. Roy. Met. Soc., No. 95, 1969
- [Ada1990] Adamson, A. W.; *Physical chemistry of surfaces*; Wiley Interscience, 1990
- [All1987] Allen, N. L., Berger, G., Dring, D.; *Positive corona and atmospheric negative ion density under repetitive impulse conditions*; IEEE Transaction on Industry Applications, Vol. IA-23, No. 6, Nov./Dec. 1987
- [Atk1962] Atkin, R.H.; *Theoretical Electromagnetism*; Printed in Northern Ireland at The University Press, 1962
- [Bad1972] Badaloni, S., Gallimberti, I.; *Basic data of air discharges*; Report Upee 72/03, Padova University, 1972
- [Bär1993] Bärsch, R.; *Verminderung des Isoliersvermögens an Feststoff/Gas-Gränzflächen durch Fremdschichtinitiierte Teilentladungen*; ETG Fachberichte 49; 1993
- [Ber1980] Berger, G.; *The effect of humidity on positive corona discharged in air*; D ès Sc. Thesis, University de Paris Sud, 1980
- [Ber1990] Bergmann, L., Schäfer, C.; *Lehrbuch der Experimentalphysik*; Band 1, Berlin New York, de Gruyter, 1990
- [Bit1986] Bittera, J.; *Silikonkautschuke – eine Übersicht. Kautschuk und Gummi Kunststoffe*, Heft 39, Nr. 1, 1986
- [Bou1946] Bouwkamp, C.; *A note on singularities in inhomogen at sharp edges in electromagnetic diffraction theory*; Physica, Vol. 12, 1946
- [Bra1971] Brazier-Smith, P. R.; *Stability and shape of insolated and pairs of water drops in an electric field*; The physics of Fluids, Vol. 14, No. 1, 1971
- [Bra2007] Braunsberger, T.; *Verhalten zyklisch betauter Silikonoberflächen bei elektrischer Beanspruchung*; Dissertation Braunschweig; 2007
- [Bus1984] Busscher, H. J.; A, van Pelt, W. J.; de Boer, P., de Jong, H. I., Arens, J.; *The Effect of Surface Roughening of polymers on measured contact angles of Fluids*; Colloids and Surfaces, Vol. 9 , 1984
- [Cha1967] Chalmers, J. A.; *Atmospheric Electricity*; Oxford, Pergamos Press England, 1967

- [Che1974] Cheng, T.C.; *Mechanisms of Flashover of contaminated insulators*; PhD Thesis; Massachusetts Institute of Technology, Boston; 1974
- [Che2003] Cheng, Z., Liang, X., Zhou, Y., Wang, S.; *Study of water droplet discharge by electric field computation and high-speed video*; Proceedings of the 7th International Conference in Properties and Applications of Dielectric Materials, Nagoya, 2003
- [EMS2009] CST STUDIO SUITE 2009, Computer Simulation Technology Darmstadt
- [Eng1984] English, W. N.; *Corona from a water drop*; Phys. Review, Vol. 74, No. 2, 1984
- [Eng1999] Engel, A., Lange, A., Langer, H., Mahr, T., Cheteverikov, M. V.; *A single peak of the rosensweig instability*; Journal of Magnetism and Magnetic Materials, No. 201, 1999
- [Exl2005] Exl, F., Kindersberger, J.; *Contact Angle Measurement on Insulation Surfaces with Artificial Pollution Layers and Various Surfaces Roughnesses*; Proceeding of the XIVth International Symposium on High Voltage Engineering, 2005
- [Fri1992] Friedrich, G. H.; *Die phisikalischen Entladungparameter der synthetischen Luft unter dem Einfluss der Feuchte und Temperatur*; Dissertation Zürich 1992
- [Gal1991] Gallimberti, I., Marchesi, G., Niemeyer, L.; *Streamer corona at an insulating surface*; 8th International Symposium oh High Voltage Engineering, Dresden Germany, 1991
- [Gei1927] Geiger, H., Scheel, K.; *Handbuch der Physik*; Julius Springer 1927
- [Gor1992] Gorur, R. S.; *Comparison of RVT silicone rubber coating under artificial contamination in a fog chamber*; IEEE Tans. On Power Delivery, Vol. 7, No. 2, 1992
- [Gou1998] Goudie, J. L., Owen, M. J., Orbeck, T.; *A Review of Possible Degradation Mechanisms of Silicone Elastomers in HV Insulation Applications*; CEIDP Conference, Atlanta, Georgia, 1998
- [Gua2005] Guan, Z., Wang, L., Yang B., Liang, X. and Li, Z.; *Elelctrical field analysis of water drop corona*; IEEE Transactions on power delivery, Vol. 20, No. 2, 2005
- [Gub2005] Gubansky, S.; *Modern Outdoor Insulators – Concerns and Challenges*; IEEE Electrical Insulation Magazine, Nov/Dec 2005

- [Gus2002] Gustavsson, T. G.; *Silicone Rubber Insulators – Impact of material formulation in coastal environment*; PhD Thesis, Göteborg, 2002
- [Ham2007] Hamamatsu Photosensor Module H 8249 Series Data Sheet, 2007
- [Har1984] Hartmann, G.; *Theoretical evaluation of Peek's law*; IEEE Transactions on Industry Applications, Vol. IA-20, No. 6, pp. 1647-1651, Nov/Dec 1984
- [Hay1958] Hayt, W.H. JR.; *Engineering Electromagnetics*; McGraw-Hill Book Company, Inc., USA, 1958
- [Hill2001] Hillborg, H. C.; *Loss and recovery of hydrophobicity of polydimethylsiloxane after exposure to electrical discharges*; Dissertation, Department of polymer technology, Royal Institute of Technology, Stockholm, 2001
- [Hof1995] Hofmann, J.; *Elektrische TE- und Ableitstrommessungen mit Impulsspannung an polymeren Isolierstoffoberflächen mit Tropfenbelägen zur Diagnose des Oberflächenzustandes – am Beispiel von Elastomeren*; Dissertation, TH Zittau, 1995
- [Ied1986] Ieda, M.; *Testing of high polymer insulation for outdoor application – review, analysis*; CIGRE-Session, paper 15-11; 1986
- [Jah2003] Jahn, H.; *Zur Bewertung stofflicher und herrstellungsbedingter auf das hydrophobie- und Erosionsverhalten von Silikonelastomeroberflächen*; Dissertation, Dresden, 2003
- [Kal1998] Kaltenborn, U., Kindersberger, J., Speck, J.; *Surface behaviour of epoxy castings during the early aging period*; IEEE International Conference on Conduction and Breakdown in Solid Dielectrics, Västerås, 1998
- [Kal2005] Kaltenborn, U.; *Die Eignung von Diagnoseverfahren zur Beurteilung der Frühphase der Oberflächenalterung von Epoxidharz-Formstoffen bei simultaner elektrischer und klimatischer Beanspruchung*; Dissertation, Darmstadt, 2005
- [Kam1993] Kamra, A. K., Bhalwankar, R. V., Sathe, A. B.; *The onset of inhomogeneous and corona in water drops falling as terminal velocity in horizontal electrical fields*; J. Geophys. Res., No. 98, D7, 1993
- [Kär1988] Kärner, C. H.; *Testing and measurement techniques for the evaluation of organic insulation materials for HV outdoor application*; Proceedings of 21 Symposium on El. Insul. Material, 1988
- [Kei2003] Keim, S.; *Optische Diagnose an singulären Tropfen auf polymeren Isolierstoffoberflächen im elektrischen Feld*; Dissertation TU Darmstadt, 2003

- [Kei2003-1] Keim, S., König, D., Hinrichsen, V.; *Experimental investigations on electrohydrodynamic phenomena at single droplets on Insulating surfaces*; IEEE Conference on Electrical Insulation and Dielectric Phenomena (CEIDP) 2003, USA
- [Kik2008] Kikuchi, Y., Murata, T., Uozumi, Y., Fukomoto, N., Nagata, M., Wakimoto, Y., Yoshimitsu, T; *Effects of ambient humidity and temperature on partial discharge characteristics of conventional and nanocomposite enameled magnet wires*; IEEE Transactions on Dielectrics and Electrical Insulation, Vol. 15, No. 6, December 2008
- [Kim1990] Kim, S. H.; *The loss and recovery of hydrophobicity of RVT silicone rubber insulator coating*; IEEE Trans. On Power Delivery, Vol. 5, No. 7, 1990
- [Kim1992] Kim, S. H.; *Hydrophobic behaviour of insulators coated with RVT silicon rubber*; IEEE Trans on Electrical Insulation, Vol. 27, No. 3, 1992
- [Kin1989] Kindersberger, J., Kuhl, M.; *Effect of hydrophobicity on insulator performance*; 6th ISH, New Orleans, paper 12.01, 1989
- [Kind1986] Kind, D., Käerner, H.; *High voltage insulation technology*, Friedr. Vieweg & Sohn, 1985
- [Kön1993] König, D.; Rao, Y. N. ; *Partial discharges in electrical power apparatus*; VDE Verlag Berlin Offenbach; 1993
- [Kor1998] Korolev, Yu. D.; Mesyats, G. A.; *Physics of pulsed breakdown in gases*; ISBN 5769107790; URO-PRESS 1998
- [Kor2006] Kories, R., Schmidt-Walter, H.; *Taschenbuch der Elektrotechnik*; Verlag Harry Deutsch 2006
- [Küc2005] Küchler, A; *Hochspannungstechnik Grundlagen – Technologien – Anwendung*; Springer Verlag Berlin; 2005
- [Küp1990] Küpfmüller, K.; *Einführung in die theoretische Elektrotechnik*; Springer Verlag, 1990
- [Lam2001] Lambrecht, J.; *Über Verfahren zur Bewertung der Hydrophobieigenschaften von Silikonelastomer Formstoffen*; Dissertation TU Dresden, Shaker-Verlag Aachen, 2001
- [Lan1903] Langevin, P.; *Recombinaison et mobilités des ions dans les gaz*; Ann. Chim. Phys. Vol. 28, 1903

-
- [Lan2000] Lange, A., Langer, H., Engel, A.; *Dynamics of s single peaks of the rosenzweig instability in a magnetic field*; Physica, D 140, 2000
- [Lap2009] Lapp Insulators GmbH; Homepage http://www.lapp-insulator.de/html_de/composites/production.php, on 17.05.2009
- [Loe1965] Loeb, L. B.; *Electrical coronas*; Berkeley, CA: Univ. Of California Press, 1965
- [Lop2001] I. J. S. Lopes; *A Study of Partial Discharges from Water Droplets on a Silicone Rubber Insulating Surface*; IEEE Transactions on Dielectrics and Electrical Insulation, Vol. 8, 2001
- [Mac1931] Macky, W. A.; *Some investigations on the deformation and breaking of water drops in strong electrical field*; Proc. Roy. Soc., Vol. A133, London 1931
- [Mal2005] Mallon, P.E., Vosloo, W. L.; *Developemnet of techniques for monitoring performance in non-ceramic high voltage insulators*; Proceedings of the 5th CIGRE Southern Africa reg. Conference, 2005
- [Maso1929] Mason, M., Weaver, W.; *The Electromagnetic Field*; Dover Publications, Inc., New York, 1929
- [Mee1978] Meek, J. M., Craggs, J. D.; *Electrical breakdown of Gases*; New York; Wiley, 1978
- [Mei1949] Meixner, J.; *Die Kantenbedingung in der Theorie der Beugung elektromagnetischer Wellen an vollkommen leitenden ebenen Schirmen*; Annals of Physics; Vol. 6, 1949
- [Mei1972] Meixner, J.; *The Behavior of Electromagnetic Fields at Edges*; IEEE. No. 4, July 1972
- [Mor2001] Moreno, V. M., Gorur, R. S.; *Effect of Long-Term Corona on Non-ceramic Outdoor Insulator Housing Material*; IEEE Trans. On Dielectr. And El. Insulation, Vol. 8, Nr. 1, Febr. 2001
- [Mos1978] Mosch, W., Hauschild, W.; *Hochspannungsisolierungen mit Schwefelhexafluorid*; Dr. A Hüthing Verlag, Heidelberg Basel, 1978
- [Mül1985] Müller, B.; *Untersuchungen zum Oberflächenverhalten von stabförmigen Isolatoren aus epoxidharz-Formstoff bei simultaner Beanspruchung durch Feuchte und hohe Wechselfpannung*, Dissertation, Darmstadt, 1985
- [Nol1926] Nolan, J. J.; *The breaking of water drops by electrical field*; Proc. Roy. Irish Acad. No. 37, 1926

- [Ock1986] Ocker, W.; *Thermische Beanspruchung verschmutzter Isolatorenoberflächen durch Gasentladungen bei Niederspannung*; Dissertation Erlangen, 1986
- [Oly1994] Olyslager, F.; *The behaviour of Electromagnetic Fields at Edges in Bi-Isotropic and Bi-Anisotropic Materials*; IEEE Transactions on antennas and propagation, Vol. 43, No. 10, October 1994
- [Owe1986] Owen, M. J.; *Dynamic wettability of hydrophobic polymers*; 8th Rocky Mountains regional Meeting of ACS, Denver, 1986
- [Pet1995] Petcharacks, K.; *Applicability of the streamer breakdown criterion to inhomogeneous gas gaps*; Dissertation Zürich 1995
- [Phi1999] Phillips, A. J., Childs D. J., Schneider, H.M.; *Water Drop Corona Effects on Full-Scale 500 kV Non Ceramic Insulators*; IEEE Trans. On Power Deliv., Vol. 14, Nr. 1, Jan 1999
- [Plon1961] Plonsey, R., Collin, R.E.; *Principles and Applications of Electromagnetic Fields*; McGraw-Hill Book Company, Inc., USA, 1961
- [Pol1985] Poli, E.; *Positive corona inception under variable humidity conditions*; 8th Int. Conf. On Gas Discharge and their Applications (Oxford) IEE Conference Publication, pp. 593-596, 1985
- [Qui1993] Quint, I.; *Untersuchungen zum Einfluß von schwach leitenden Fremdschichten auf das Oberflächen-Alterungsverhalten wechsellspannungsbelasteter zylindrischer Prüfkörper aus Epoxidharz-Formstoff*; Dissertation Darmstadt, 1993
- [Rao1971] Rao, C. R., Raju, G. R. G.; *Growth of ionization currents in dry air at high values of E/n*; J. Phys. D: Appl. Phys. 4, pp. 494-503, 1971
- [Ren1974] Les Renardieres Group; *Positive discharges in long air gaps at Les Renardieres*; Electra, Vol. 35, 1974
- [Sch1923] Schumann, E. O., *Elektrische Durchbruchfeldstärke von Gasen. Theoretische Grundlagen und Anwendungen*; Springer Verlag, 1923
- [Sch1990] Schütte, T., Hörnfeldt, S.; *Dynamics of electrically stressed water drops on insulating surface*; IEEE International Symposium on Electrical Insulation, 1990
- [Sch1992] Schmuck, F.; *Zur zeittraffenden Alterungsprüfung von Silikongummi-Oberflächen undet Fremdschichbelastung und simultaner 50 Hz-Spannungsbeanspruchung*; Disseration Zittau, 1992
- [Sch1996] Schwuger, M. J.; *Lehrbuch der Grenzflächenchemie*; Georg Thieme Verlag, Stuttgart, New York, 1996

- [Sei2006] Seifert, J., Bärsch, R.; *Bewertung des Designs von Silikon-Verbundisolatoren unter dem Aspekt des Isolierstoffoberflächen – Fremdschichtverhaltens*; RCC – Tagungsbericht “Werkstoffe für Isolatoren, Überspannungsableiter, Kabelgarnituren, Schaltgeräte in der Hochspannungstechnik”, Berlin 2006
- [She1988] Sherwood, J. D.; *Breakup of fluids droplets in electric and magnetic fields*; The Journal of Fluids Mechanics, Vol. 188, 1988
- [Sig1991] Sigmond, R. S.; *On the role of water in aging of polymers in air-insulated electrical systems*; IEEE Trans. On Electrical Insulation, Vol. 26, No. 4, 1991
- [Sol2009] SolidWorks 2008-2009, SolidWorks Corporation
- [STR1992] STRI Guide1, 92/1; *Hydrophobicity Classification Guide*; Swedish Transmission Research Institute, 1992
- [Stra1941] Stratton, J.A.; *Electromagnetic Theory*; McGraw-Hill Book Company, Inc., USA, 1941
- [Tat2008] Tatizawa, H., Soletto, K., Bacega, W. R.; *Proposal of a Partial Discharge Detection Method for Laboratory and Field Conditions*; Transmission and Distribution Conference and Exposition, T & D IEEE/PES, 2008
- [Tay1964] Taylor, G.; *Disintegration of the water drops in an electric field*; Proceedings of the Royal Society, Vol. A280, London, 1964
- [Vla1991] Vlastos, A. E. ; *Surface structural changes of naturally aged silicones and EPDM composite insulators*; IEEE Trans. On Power Delivery, Vol. 6, no. 2, 1991
- [Vos2004] Vosloo, W. L., Macey, R. E., Tourreil, C. De; *The Practical Guide to Outdoor High Voltage Insulators*; Crown Publications cc. Johannesburg 2004
- [Wat1970] Waters, R. T., Rickard, T. E., Stark, W. B.; *Electrical field and current density in the impulse corona discharge in a rod/plane gap*; Proc. Roy. Soc. A. 304, pp. 187-210, 1968
- [Weil1977] Weiland, T.; *A Discretization Method for the Solution of Maxwell's Equations for six-component Fields*; AEÜ Archiv für Elektrotechnik Übertragungstechnik, Band 31, pp. 116-120, 1977
- [Weil1979] Weiland, T.; *Lossy Waveguides with an Arbitrary Boundary Contour and Distribution of Material*; AEÜ Archiv für Elektrotechnik und Übertragungstechnik, Band 33, pp. 170-174, 1979

- [Weil1985] Weiland, T.; *On the Unique Numerical Solution of Maxwellian Eigenvalue Problems in Three Dimensions*; Particle Accelerators, Vol. 17, pp. 227-242. 1985
- [Weil1996] Weiland, T.; *Time Domain Electromagnetic Field Computation with Finite Difference Methods*; Int. J. Num. Mod.: Electronic Networks, Devices and Fields, Vol. 9, pp. 295-319, 1996
- [Weil1998] Weiland, T.; *Elektromagnetisches CAD – Rechnergestützte Methoden zur Berechnung von Feldern*; Skriptum zur Vorlesung Feldtheorie II, TU-Darmstadt, 1998
- [Wind1994] Windmar, D.; *Water drop initiated discharges in air*; Dissertation Uppsala 1994
- [Wil1925] Wilson, C. T. R., Taylor, G. I.; *The bursting of soap bubbles in a uniform electric field*; Proc. Camb. Phil. Soc., No. 22, 1925
- [Win2006] Winter, H.-G., Bärsch, R.; *Oberflächenverhalten von Silikonelastomeren unter Feuchte- und biogenen Belastungen*; RCC-Conference review, Berlin, 2006
- [Wor2004] CIGRE Working Group D1.14; *Material properties for non-ceramic outdoor insulation*; State of art; Elecra No. 217, Dec. 2004
- [Yeo2006] Yeon-Ho, O., Ki-Dong, Song; *Modified Finite Element Method to Consider the Singularity of the Electrical Field Using a Singularity Function*; Annual Report Conference on Electrical Insulation and Dielectric Phenomena, 2006
- [Yos1996] Yoshiday, K.; Tagashiraz, H.; Ohshimay, T.; Ohuchiy, H.; Kishimoto, Y.; *Measurement of the Townsend first ionization coefficient in tetraethoxysilane and oxygen mixtures*; J. Phys. D: Appl. Phys. 29, pp. 2124–2128, 1996
- [Zis1964] Zisman, W. A.; *Relation of equilibrium contact angle to liquid and solid constitution*; Advanced Chemistry, Series 43, 1964

Curriculum Vitae

Simona Danuta Feier Iova

Personal Information:

- Born: *Iova*
- Date of Birth: *17.09.1979*
- Place of Birth: *Salonta, Romania*
- Marital Status: *married*
- Nationality: *Romanian*

Academic Formation:

1994 - 1998	Upper secondary school at the National College "Arany Janos" Salonta, Romania
1998 - 2003	Student at the Faculty of Electrical and Power Engineering, "Politehnica" University Timisoara, Romania Degree: Diploma in Engineering (Dipl.-Ing.)
2003 - 2004	Student at the Faculty of Electrical and Power Engineering, "Politehnica" University Timisoara, Romania Degree: Master of Science (M. Sc.)
2004 - 2009	Scientific assistant at High Voltage Laboratories, Darmstadt, University of Technology, Darmstadt, Germany

List of publications

- [1] Toader, D., Iova, S.; *Mutual inductance calculation between earth-conductor loops*; The VIII ETRAN - IEEE Conference, Juni 2004 Cacak, Serbia and Montenegro
- [2] Toader, D., Iova, S.; *The calculation of the single-phase short circuit current distribution in station installation for microhydroplants*; WEC Regional Energy Forum, June 2004, Neptun Romania
- [3] Nemes, M., Vuc, G., Paunescu D, Iova, S.; *Energy market. Forecast of the Next-Day price*; International Symposium on energy efficiency, October 2004, Cluj Napoca, Romania
- [4] Iova, S., Vuc, G., Paunescu, D., Nemes, M.; *Optimal Pattern for Next-Day Price Forecasting*; The 6th International Power Systems Conference, 2-4 November 2005, Timisoara, Romania
- [5] Braunsberger, T., Iova, S., Kurrat, M., Hinrichsen, V.; *Partial discharge processes at sessile water drops*; Proceedings of the XVI Gas Discharges and their Appl. 2006, Xian, China
- [6] Feier-Iova, S., Hinrichsen, V.; *Experimental investigation and modeling of mechanical deformation and inception voltage of water drops on insulating surfaces stressed by electrical field*; International Symposium on High Voltage Engineering, 27-31 August 2007, Ljubljana, Slovenia
- [7] Feier-Iova, S., Hinrichsen, V.; *Partial Discharge Inception Voltage of Water Drops on Insulating Surfaces Stressed by Electrical Field*, IEEE El. Insul. Conference 1-3 June 2009, Montreal, Canada
- [8] Feier-Iova, S., Hinrichsen, V.; *Partial Discharge Inception Voltage of Water Drops on Insulating Surfaces Stressed by Electrical Field*, International Symposium on High Voltage Engineering, 21-28 August 2009, Cape Town, South Africa

Coordinated diploma theses

- [1] Sébastien Blatt; Theoretische Berechnungen des Verhaltens von Wassertropfen auf Isolierstoffoberflächen unter dem Einfluss eines elektrischen Feldes; Nr. 1826; 2008
- [2] Michael Tenzer; Graphische Modellierung und elektrostatische Simulationen des Verhaltens von Wassertropfen auf Isolierstoffoberflächen unter dem Einfluss des elektrischen Feldes, Nr. 1828; 2009

Anlage 2: Erklärung laut §9 PromO

Erklärung laut §9 PromO

Ich versichere hiermit, dass ich die vorliegende Dissertation allein und nur unter Verwendung der angegebenen Literatur verfasst habe. Die Arbeit hat bisher noch nicht zu Prüfungszwecken gedient.

Darmstadt, den 9. September 2009

S. Feier-lova